THE MINISTRY OF NATIONAL
INFRASTRUCTURES
GEOLOGICAL SURVEY OF ISRAEL

Landscape and tectonic evolution of the Central Negev in response to Dead Sea rifting

Benny Guralnik

Report GSI/11/2009 **Jerusalem, October 2009**

THE MINISTRY OF NATIONAL
INFRASTRUCTURES
GEOLOGICAL SURVEY OF ISRAEL

Landscape and tectonic evolution of the Central Negev in response to Dead Sea rifting

Benny Guralnik

This work was submitted as a thesis for the degree of Master of Science to the Department of Geology, Institute of Earth Sciences, Faculty of Mathematics and Natural Sciences, The Hebrew University, Jerusalem.

The study was carried out under the supervision of:
Dr. Ari Matmon, Institute of Earth Sciences, The Hebrew University, Jerusalem
Dr. Yoav Avni, The Geological Survey of Israel, Jerusalem
Dr. Ezra Zilberman, The Geological Survey of Israel, Jerusalem

Report GSI/11/2009 Jerusalem, October 2009

Abstract

The present study investigates landscape evolution of the central Negev since the Pliocene, focusing on: (i) the possible timing and character of the transition from the Pliocene paleo-Paran drainage system to the present one, and (ii) the middle Pleistocene to present-day development of the drainage basins.

Drainage basin evolution and its relationship with Quaternary subsidence history of the western margins of the Dead Sea Rift (DSR) are reconstructed by using cosmogenic concentrations and exposure ages of desert pavements that have developed over westward-flowing alluvial surfaces, which were active in the Pliocene (e.g., the Edom River). Relicts of these streams are currently found at progressively lower elevations approaching the rift from west to east, reflecting eastward tilting and subsidence. Reconstruction of the tilting history of these surfaces was done by comparing their cosmogenic concentrations and exposure ages to those obtained from tectonically stable areas. The results show that the Pliocene drainage system collapsed between 2.0 – 1.6 Ma, that most of the subsidence in the Arava valley occurred between 1.6 – 1.0 Ma and diminished with time since then, and that since ~1.4 Ma, fluvial response to rift tectonics is expressed within the current basins by inset terraces.

In the middle – late Quaternary terrace remnants in the Neqarot and Paran basins, cosmogenic profile model ages correlate well to OSL ages sampled from the same units, and suggest regional depositional events at ~300 ka, ~200 ka, ~100 ka and ~10 ka. Analysis of cosmogenic isotopic signals in the present-day alluvium of the Neqarot leads to the conclusion that the central Negev is undergoing a degradation phase and is evacuating previously deposited sediment. Modeled cosmogenic inheritance of sand and chert during terrace deposition is interpreted here as basin-wide paleo-erosion rates. The "apparent erosion rate" of sandstone has a narrow range around 16 – 21 m/Ma, which is fairly constant with time. In the same terraces, the "apparent erosion rate" of chert diminishes from 13 m/Ma at ~300 ka to 2 m/Ma today, being possibly the result of middle to late Quaternary aridification of the region.

Acknowledgements

I'm greatly indebted to my advisor Dr. Ari Matmon, for guidance in every aspect of this work, and for teaching me to do science; to my advisors Dr. Yoav Avni and Dr. Ezra Zilberman, for tirelessly teaching me the geology of the Negev in the field and in the office. This work would have been completely impossible without Dr. David Fink (ANSTO), who helped in fieldwork, performed most of the AMS analyses, evaluated the results and clarified many ideas. I'm also obliged to Michael Davis for his help in collecting and processing the OSL samples. I deeply appreciate the aid of Imri Oz, Ahuva Agranat, and Dr. Nadia Teutch in the lab.

Excellent advice and critical review of work at progress was made by Prof. Zvi Garfunkel and Prof. Yehouda Enzel. Fruitful discussions with Dr. Hanan Ginat, Prof. Boaz Lazar and Prof. Amotz Agnon significantly extended the scope of this work. Dr. Rani Calvo, Dr. Amit Segev, Dr. Benjamin-Ze'ev Begin, Dr. Naomi Porat and Dr. Rivka Amit from the Geological Survey always helped with good advice and encouragement. Yaakov Rafael, Yaakov Mizrachi and Ariel Belmas helped in fieldwork, and Bat-Sheva Cohen, Channa Netzer-Cohen, and Nili Almog assisted in publishing. Prof. Nathan Paldor, Magi Perkin, Batia Moshe, Shoshana Busheri, Dikla Chanuka and Avital Arieli stood out in handling all administrative matters, and Sharon Lieber in library assistance.

I deeply thank my friends Shalev Siman-Tov, Itay Nudel and Rotem Golan for various help and support in the field and afterwards; Eden Almog for acquainting me with cosmogenic isotopes; Prof. Bruce Harrison, Prof. Ramon Arrowsmith, Dr. Sinan Akciz, Prof. Kelin Whipple, Prof. Dov Avigad and Prof. Victor Targulian for their generous sharing of their geologic experience; and my parents for their love and support.

Finally, I thank many unmentioned teachers, colleagues and friends for their help, encouragement and sincere interest in this work. This research was funded by ISF grant 188/06.

Thesis organization

Following a general introduction and methods, three separate topics are presented as standalone chapters, each including its own introduction, methods, results, discussion and a summary. In the conclusion section, an overview and synthesis of all the different topics is presented. Equations, figures and tables were numbered sequentially throughout the thesis to avoid duplication.

TABLE OF CONTENTS

LIST OF FIGURES

LIST OF TABLES

1. Introduction

1.1. Research motivation and goals

Drainage systems are significantly modified by rifting processes (e.g., McKee and McKee, 1972; Rosendahl, 1987; Summerfield, 1991; Wdowinski and Zilberman, 1996), most notably resulting in major changes in stream direction and drainage basin fragmentation (e.g., Ollier, 1995; Avni, 1998; Van der Wateren and Cloetingh, 1999, and references therein; Zelilidis, 2000; Bart, 2004; Mack et al., 2006). Although fluvial response to active tectonics has been extensively studied in orogens and subduction provinces, landscape development in active rifting zones has gained much less attention, and was usually studied only indirectly (e.g., via sedimentary sequences that fill the rift basin.)

The Negev Desert (10,000 km^2 at 29°–31°N, Figures 1–2) is part of the larger Saharo-Arabian desert belt, and is currently among the driest places on Earth (Amit et al, 2006), mostly receiving <80 mm yr^{-1} of precipitation. It is situated to the west of the Dead Sea Rift valley (DSR), part of the long tectonic boundary between the African and Arabian plates, which developed in the Miocene as a strike-slip fault and gained a vertical component contributing to subsidence at ~5My (Garfunkel, 1981). Good preservation of Pliocene – Quaternary alluvial sediments located throughout the central Negev and related to the various stages of drainage basin development enabled extensive research by generations of geoscientists (e.g., Picard, 1943; Shaw, 1947; Bentor and Vroman, 1957; Garfunkel and Horowitz, 1966; Gerson et al., 1985; Zilberman et al. 1996; Ginat, 1997; Avni, 1998), which laid down a solid geological framework of the long and complicated history of landscape development at the DSR margins. However, gaps in age constraint of the terrestrial units and their accumulation and erosion rates inhibited until now a full understanding of the landscape evolution processes and the tectonic patterns that prevailed during the Plio – Pleistocene times.

The present study focuses on the Paran and Neqarot drainage basins, two of the largest ephemeral streams in the Negev today. In the Pliocene, these currently separate basins were connected, forming an even larger, "paleo-Paran" basin (Avni et al, 2000). At the beginning of Pleistocene, the paleo-Paran disintegrated into smaller separate basins due to an eastward stream capture, driven by the eastward regional tilting of the central and southern Negev towards the subsiding Dead Sea and Arava basins (Avni et al., 2000). Initially, the ages of the fluviatile and lacustrine units deposited by the paleo-Paran river (Arava Formation; Avni et

al., 2001) and of the lacustrine and paleosol units deposited during the transition to the present-day drainage (Zehiha Formation; Ginat et al., 2002, 2003), were solely based on field relations and regional biostratigraphic or geomorphic correlations, reflecting the difficulty to date Million-year old continental terrestrial deposits. In a recent study (Simhai et al., 2007; Matmon et al., 2009), the first direct age (cosmogenic surface exposure age) of 1.9 – 1.5 Ma was obtained for the top of Arava Formation, confirming that the major drainage transition occurred in the early Pleistocene. However, two major knowledge gaps within the Plio-Pleistocene time framework remained intriguing:

1. While the abandonment age of the Arava Formation has been recently reported (1.9 – 1.5 Ma), the age of the base of the formation is only indirectly conjectured (4 – 2 Ma) from field relations and from geomorphologic correlation with dated basalts in Jordan.
2. In the period between the Zehiha lake deposits (early Pleistocene) and the oldest dated Quaternary terrace (300 ka), not a single sediment has been so far dated; this time gap may be either artificial (i.e., terraces of this age exist, but were beyond the dating techniques used so far) or real (implying that the absence of such terraces reflects continuous evacuation of material outside the basins).

The goal of this research was to understand and quantify the relations between the tectonic history of the Dead Sea Rift's western margin, and the geomorphological evolution of major drainage systems affected by it. Specifically, we utilized multiple dating methods (cosmogenic isotopes and OSL) in order to:

1. Determine the "surface exposure ages" of major wind gaps and the highest terraces along the abandoned courses of the paleo-Paran river. The spatial distribution of the abandonment ages of dry palaeo-valleys is the key to decipher the tectonic history of a region (e.g., Keller et al., 1999; Burbank and Anderson, 2001), and reconstruct the evolution of the present drainage network.
2. Determine the rate of the Plio – Pleistocene subsidence and eastward tilting of the Negev. The progressive subsidence of relicts of ancient stream deposits will be reconstructed by combining their abandonment ages with their estimated subsidence amount, calculated by using assumed but reasonable paleo-gradients. Moreover, since cosmogenic production rates are *altitude-dependent*, they can be used as a

"paleoaltimeter" for tracing elevation changes during exposure of the surface (e.g., Brown et al., 1991).

3. Refine the temporal and spatial framework of regional Quaternary erosion and deposition cycles, by means of high-resolution cosmogenic and OSL depth profiles of abandoned alluvial terraces along the routes of the major streams (e.g., Robinson et al., 2004). An inter-comparison of these different dating methods yields improved understanding of past fluvial regimes and basin-wide bedrock paleo-erosion rates with a possible contribution to paleoclimate research.

1.2. The geological setting of the Negev

The geological structure and stratigraphic sequence of Israel in general and of the Negev in particular reflect three major regional geologic and tectonic phases (Garfunkel, 1988): (i) the Precambrian Pan-African orogeny resulting in a suite of crystalline rocks termed "The Basement" (ii) a Cambrian – late Eocene "platform" stage during which a sequence comprising mostly of sandstone and carbonates was deposited, and (iii) the breakup of the African Plate by the Dead Sea Transform (DST), which initiated in the Miocene, resulting in terrestrial fluviatile and lake deposits.

Four major structural elements of the central Negev are present in the study area (Figure 1):

1. The Mahmal, Ramon and Badad anticlines, which are related to the Syrian Arc Fold Belt (SAFB) and which started to form in the late Cretaceous.
2. The E–W- and WSW–ENE-trending Saad–Nafha, Ramon, Arif–Batur, Paran and Thamad faults related to the late Cretaceous–Miocene Sinai–Negev Shear Zone (SNSZ), as characterized by right-lateral movement (Bartov, 1974). Significant structures such as the Karkom Graben and the transpressional Menuha Ridge are located along these faults (Bartov, 1970; Sakal, 1967).
3. The NNE–SSW-trending Halamish, Baraq–Zihor–Zenifim, Uvda, Milhan and Gerofit lineaments. These "longitudinal faults" (Ginat, 1997; Avni, 1998) form a 40–60-km-wide belt west of the DSR, which was tectonically activated in the early Pleistocene At that time, all previous structures described above were set on a 60–100-km-wide asymmetric upwarp with its main N-S axis located 50 km west of the Arava (termed: "arching"; Picard, 1943).
4. The Arava valley, which is the local expression of the larger Dead Sea Rift. The Arava valley is delineated by the DST fault segments: the Arava–Dead Sea, Zofar, Yaalon and Aqaba–Gharandal faults.

The activity of structural elements 3 and 4 is related to Dead Sea rifting (Avni, 1998). Thus they influenced the Quaternary drainage basins along the western margin of the rift. The evolution history of the central Negev drainage systems relates to activity along these structural features.

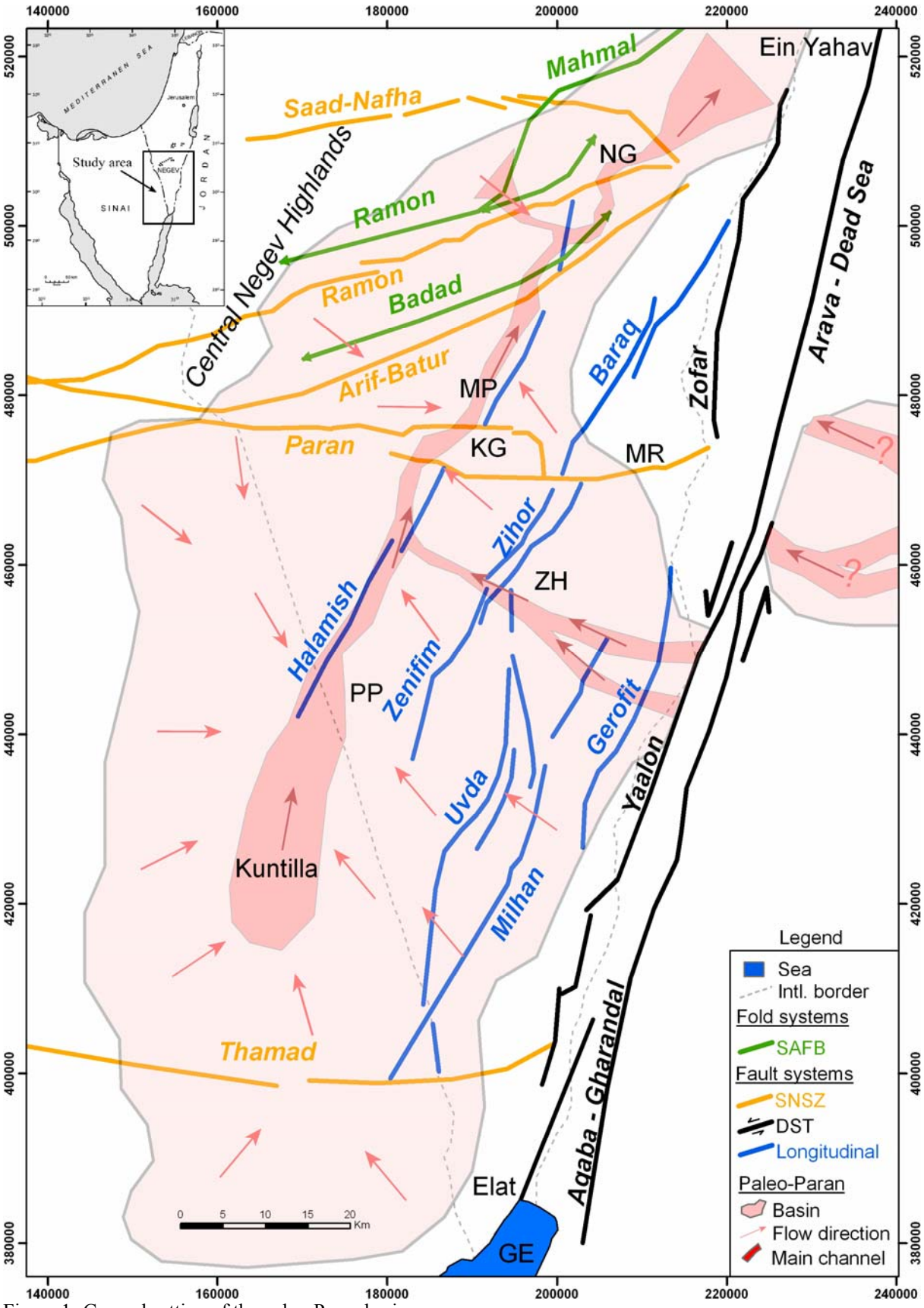

Figure 1: General setting of the paleo-Paran basin.

DST – Dead Sea Transform; SAFB – Syrian Arc Fold Belt; SNSZ – Sinai-Negev Shear Zone; NG – Neqarot Gorge; MP – HaMeshar Plain; KG – Karkom Graben; MR – Menuha Ridge; ZH – Zehiha Hills; PP – Paran Plains; GE – Gulf of Elat. (Sources: Sneh et al., 1998; Ginat, 1997; Avni 1998; Avni et al., 2000)

The Dead Sea Fault system accommodates mostly left-lateral strike-slip motion which initiated 18 – 14 Ma (Bartov et al, 1980; Figure 2a). This motion did not interfere at first with the westward-flowing rivers, which originated hundreds of km east of the transform boundary and successfully crossed it, draining into the Mediterranean (Bentor and Vroman, 1957; Neev, 1960; Zak and Freund, 1981; Calvo and Bartov, 2001). At ~5 Ma, extension initiated the development of the Dead Sea Rift (DSR) as a deep inland drainage basin and caused uplift of the rift margins (Garfunkel, 1981; Figure 2b,c). The scale of uplift along the central Negev was sufficient to cause collapse of the former drainage pattern (Wdowinski and Zilberman, 1997) and create a new water divide (Picard, 1943) that led to the establishment of the paleo-Paran river system sub-parallel to the rift direction (Garfunkel and Horowitz, 1966; Zilberman et al. 1996; Avni et al., 2000). This system, which was never directly dated, was attributed an age of 4 – 2 Ma (Avni et al., 2000) and drained the northern Sinai and the Negev towards the Dead Sea basin. It also and included a few westward-flowing tributaries that still crossed the plate boundary in the central Arava, where subsidence was minimal (Ginat et al., 1998, 2000, 2002; Figure 1). In the early Pleistocene, further subsidence in the central Arava valley and uplift of the central Negev Highland to its west (Figure 1) inverted the regional gradient, causing eastward tilting of the southern Negev. Tilting was accommodated by rotation of small, separate blocks along horizontal NNE-SSW axes (Garfunkel, 1970; Ginat et al., 2000). The direction of major westward-flowing streams in this newly tilted area (i.e., between the Negev Highlands and the Arava) was reversed, and stream flow towards the rift on the east was initiated (Garfunkel and Horowitz, 1966; Gerson et al., 1985; Kafri and Heimann, 1994; Ginat et al., 1998, 2000; Matmon et al., 1999; Avni et al., 2000; Ben David et al., 2002; Zilberman and Avni, 2006; Avni and Zilberman, 2007). Similar geomorphic processes of basin and tectonic evolution have been reported from other extensional provinces around the world (e.g Summerfield, 1991; Ollier, 1995; Zelilidis, 2000; Mack et al., 2006). Presently, lake deposits and soils that accumulated in the Negev during this *stream reversal stage* (i.e., regional zero gradients) are at progressively lower elevations towards the rift, and thus can record the amount of Quaternary subsidence.

1.3. The subsidence mechanism of the Dead Sea Rift's western margin

The topography of the central and southern Negev displays a distinct flexure towards the Arava valley on the east where subsidence was greatest (Figure 2c). In contrast, the major north-trending tectonic lines in the Negev, spaced at intervals of 3 – 10 km, display normal faulting in an opposite sense (i.e., east side up; Ginat, 1997; Avni, 1998). These seemingly

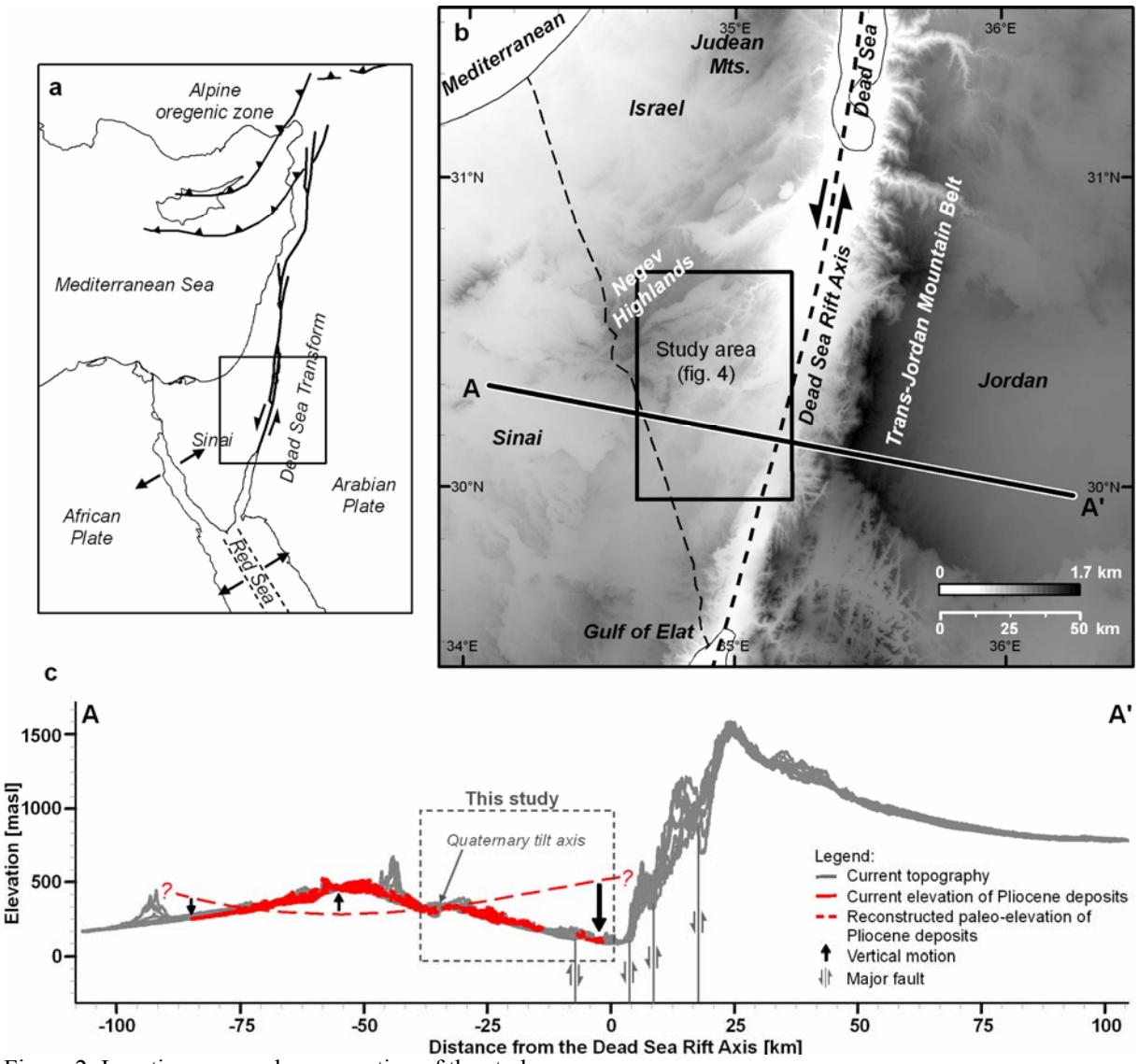

Figure 2: Location map and cross section of the study area
a) Location map of study area in the Eastern Mediterranean, b) general topography of the area, c) a topographic cross section across the rift flanks (A-A') (after Wdowinski and Zilberman, 1997; SRTM 90m elevation database).

contradictory observations can be reconciled by considering the upper brittle crust of the Negev as being flexed towards the rift through a series of tilted blocks which accompany the regional tilted surface (Garfunkel, 1970; Figure 3). These bookshelf-type structures are commonly found in rifted domains, where their primary function is to accommodate the brittle crust extension imposed by the stretching and thinning of ductile lower crust (Mandl, 1987). To test whether and how this mechanism applies for the central Negev, elevation of the tilted paleo-Paran deposits along the Edom river (Ginat et al., 2000) was digitized (Figure 4; red solid line) and a block-rotation algorithm (*blockrot.m*, see Appendix 8.4) was applied. A minimum-seeking procedure was used to find the best-fitting parameters of the initial topography: block height, subsurface fault geometry, angle of block rotation (α, similar to all blocks), and the tilt angle of the surface on which all blocks are leaned (β). The results show

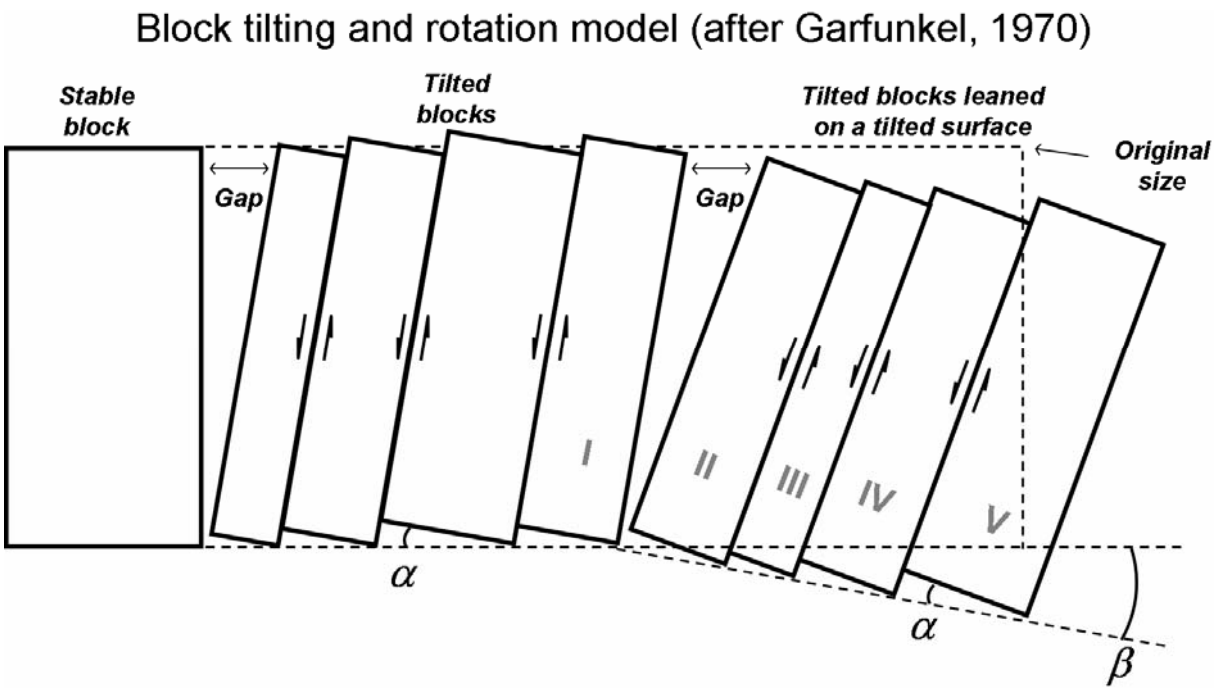

Figure 3: Block rotation model (after Garfunkel, 1970)
Regional rotation (indicated by the angle β for blocks II-V), is superimposed on local rotation (indicated by α and common to all blocks), no vertical exaggeration.

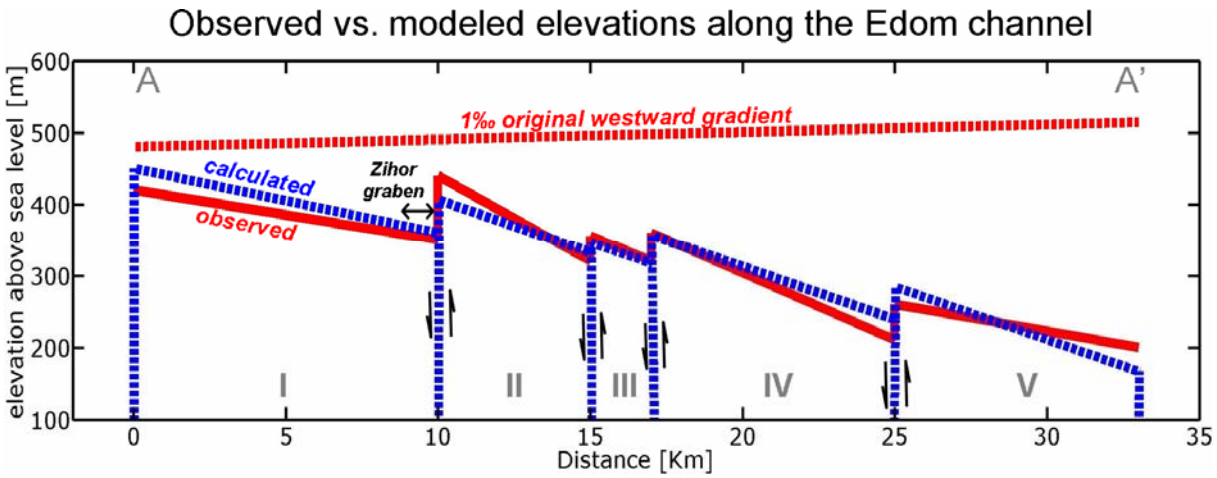

Figure 4: Observed and modeled elevations of the Edom channel
Observed and modeled elevations of the Edom channel facies along transect AA' (A=183/462, A' = 210/450 ITM Coordinates), vertical exaggeration of ~20. The model uses a pre-reversal gradient of 1‰, block height of 2 km, subvertical faults (dipping >80°), α=0.3° and β=0.6°. The calculated elevations reproduce actual heights of outcrops within a precision of 30 m.

that the actual elevations of the Edom river deposits can be reproduced within <30 m accuracy by a block rotation model with the following parameters: a pre-reversal regional westward gradient of 1‰, block height of 2 km, subvertical faults (dipping >80°), α=0.3° and β=0.6°. This result confirms that the eastward tilting in the central Negev during the Quaternary is likely to have been accompanied by a bookshelf rotation mechanism, implying a simultaneous rotation of a composite system behaving as one unit, rather than by spontaneous vertical motions of separate blocks at different times. Therefore, a monotonous

history of elevation change, and subsidence rate increase towards the rift's margins can be considered.

1.4. Neogene stratigraphy in the Negev

The Paran river drainage basin, the largest on the western margin of the Arava valley, drains toward the Dead Sea an area of ca. 3800 km^2 including northeastern Sinai and the southern Negev (Figure 1). Its inner basin elevation ranges from ~1000 masl west of Elat to ~100 m *below* sea level at its outlet in the Arava valley. The water divides between the current Paran basin and the adjacent basins of Neqarot and Hiyyon include several wide wind gaps, known as the "Meshar Plains" and "Zehiha Hills" (Figure 1), respectively. The presence of Pliocene conglomerates across the basins and their preservation in the wind-gaps led to realization that these three basins were part of a larger ancient basin, termed the paleo-Paran (Avni et al., 2000; Figure 1).

Bentor and Vroman (1957) were the first to use the term “Arava Conglomerate”, referring to coarse conglomerates (3–5 m thick) deposited in angular unconformity above the Miocene Hazeva Formation or older Tertiary–Cretaceous units in the northern Arava valley. In a pioneering geomorphological work, Garfunkel and Horowitz (1966) distinguished between the "Arava Conglomerate", characterized by the abundance of well-rounded and "allochthonous" pebbles (most strikingly, the igneous clasts derived from the "Basement" outcrops in Elat and Jordan), and a younger unit which they termed "Hameshar Formation", characterized by angular gravels of local origin intercalated with lacustrine-like beds. They related each of these units to a particular drainage system, suggesting that the Arava Conglomerate was transported eastward into the Arava valley, whereas the Hameshar Formation was deposited by a westward flowing river which drained into the Mediterranean through northern Sinai. Avni (1998) re-evaluated these and other depositional units in the central Negev (e.g., Sneh, 1982; Rabb'a, 1994; Livnat and Kronfeld, 1990) and incorporated all of them into a new stratigraphical framework termed the "Arava Formation". Avni (1998) and Ginat (1997) concluded that (a) this formation was deposited by a major drainage system whose main channel flowed west of and subparallel to the Dead Sea Transform and (b) during both stages of the paleo-Paran river, its final outlet was always the Dead Sea. Ginat (1997) and Ginat et al. (2003) described a lacustrine unit postdating the Arava Formation (Zehiha Formation), and both Avni (1998) and Ginat (1997) described morphostratigraphic relations of the middle to late Quaternary terraces termed Q1-Q4, from oldest to youngest, which were

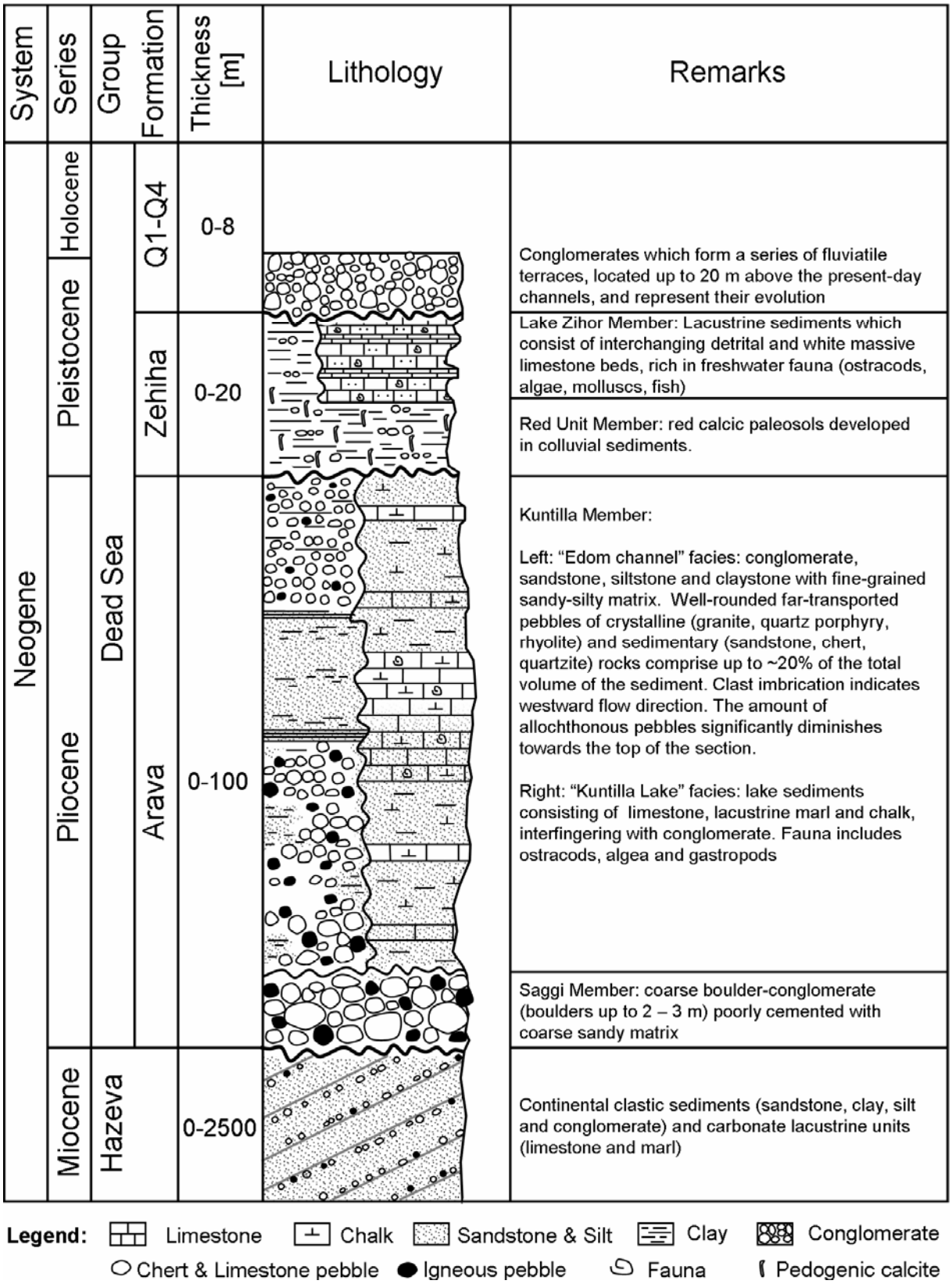

Figure 5: Stratigraphic columnar section of Neogene units in the central and southern Negev.
Sources: Avni et al., (2000), Ginat et al., (2000; 2002; 2003), Calvo and Bartov (2000)

deposited in the current drainage network. The up-to-date division of the Plio-Plesitocene units is summarized below.

The Arava Formation overlies the Miocene Hazeva Group and older units of Tertiary-Cretaceous age in an angular and erosive unconformity (Figure 5). In several locations in the central and southern Negev it is overlain by the early Pleistocene Zehiha Formation (Avni et al., 2001). Arava Formation is divided into two distinct members. The lower Saggi Member is 5–30 m thick and consists of poorly-cemented coarse boulder conglomerate (up to 2–3 m in diameter). Most clasts consist of chert and limestone with small lithoclasts and a coarse-sandy matrix. The upper Kuntilla Member is 40–100 m thick and consists of conglomerate, sandstone, siltstone and claystone with fine-grained silty-sandy matrix, and calcareous cement. A lacustrine sequence, up to 40 m thick, interfingers with the fluviatile sequence of this unit in the upper Paran basin, in the Karkom Graben, and in the central and northern Arava valley indicating the existence of poor drainage and temporal shallow water bodies within the drainage system. The age of Arava Formation based on field relations in the Negev and a geomorphological correlation to Jordanian basalts in Wadi Zarqa was constrained between 4 – 2 Ma (Avni et al., 2000, 2001). The deposition and abandonment of the Arava Formation in the Paran Plains (Figure 1) has been recently dated to 2.15 – 1.9 Ma (Simhai et al., 2007; Matmon et al., 2009).

The Zehiha Formation (Figure 5) overlies the Arava Formation with a slight angular and erosive unconformity (Ginat, 1997). It consists of lacustrine deposits laterally changing into fluvial coarse and fine gravel deposits rich in red calcic buried soil horizons. The lacustrine deposits comprise of 15 m of detritic limestone, whose age was attributed to early Pleistocene (Ginat, 1997; Rosenfeld et al., 1997; Ginat et al., 2003), based on the resemblance of its fauna and early Paleolithic hominid tools to those of the 'Ubediya Formation, for which the age of 1.4 Ma has been proposed (Tchernov, 1987).

Four alluvial terraces (Q1 – Q4) postdating the Zehiha Formation (Figure 5) can be found at the margins of present-day channels, forming a "staircase" up to ~30 m above the thalweg of the active channel. The terraces show an increasing development of salic-gypsic reg soils overlain by desert pavement (Amit et al., 1993). Within the Karkom Graben, the Quaternary alluvial surfaces that have been previously dated by OSL include Q1 (>300 ka), Q2 (100 – 55 ka) and Q3 (15 – 7 ka) (Avni et al., 2000b).

2. Methods

2.1. Cosmogenic nuclides and their use in geomorphology

Theoretical background

Earth and other objects in the solar system are exposed to a continuous flux of elementary particles (cosmic radiation) which hit molecules in the upper atmosphere and create a secondary flux of elementary particles which reach the surface of earth (Faure and Mensing, 2005). At mountaintop elevations, most of the secondary cosmic radiation is composed of neutrons, because they have a higher probability of being emitted from stimulated nuclei, and because, being electrically neutral, they are not slowed by ionization energy losses to atoms that they encounter while traveling through the atmosphere (Gosse and Phillips, 2001). As an elementary particle collides with a lattice atom within the rock, an in-situ cosmogenic nuclide forms by spallation (Figure 6). This is a high-incident energy process in which a neutron (or other nucleon) collides with a target nucleus (e.g., $^{16}_{8}\mathrm{O}$) and breaks off several lighter particles (e.g., 4p3n), leaving a lighter residual nucleus (e.g., $^{10}_{4}\mathrm{Be}$) (Gosse and Phillips, 2001).

Some of the more common in-situ cosmogenic nuclides include ^{3}He, ^{10}Be, ^{14}C, ^{21}Ne, ^{26}Al and ^{36}Cl (Gosse and Phillips, 2001). The rate of their in-situ (and atmospheric) production increases with latitude and altitude (Figure 7), due to lesser interaction with the terrestrial geomagnetic field and lesser interactions with atmospheric molecules, respectively (Gosse and Phillips, 2001). At latitudes of >60°, the nucleon flux is unaffected by the geomagnetic field, and thus production rates measured at the Sea Level High Latitude (SLHL) serve as a global reference. The fundamental scaling models for latitude and altitude (Lal and Peters, 1967; Lal, 1991) are being at present extended to include the second-order influences of temporal and spatial variations in the atmosphere (Stone, 2000), secular variations in the geomagnetic field (Dunai, 2001; Desilets and Zreda, 2003, 2006), solar modulation (Lifton et al., 2005), and non-dipole components of the geomagnetic field (Dunai, 2000; Lifton et al., 2008).

The production rates of cosmogenic nuclides at Sea Level High Latitude range from just a few atoms g^{-1} y^{-1} (e.g., 4.58 for ^{10}Be) to hundreds of atoms g^{-1} y^{-1} (e.g., 115 for ^{3}He). The low production rate, and in consequence the low concentrations, inhibited their serial measurement until the development of Accelerator Mass Spectrometry (AMS) in the 1980's.

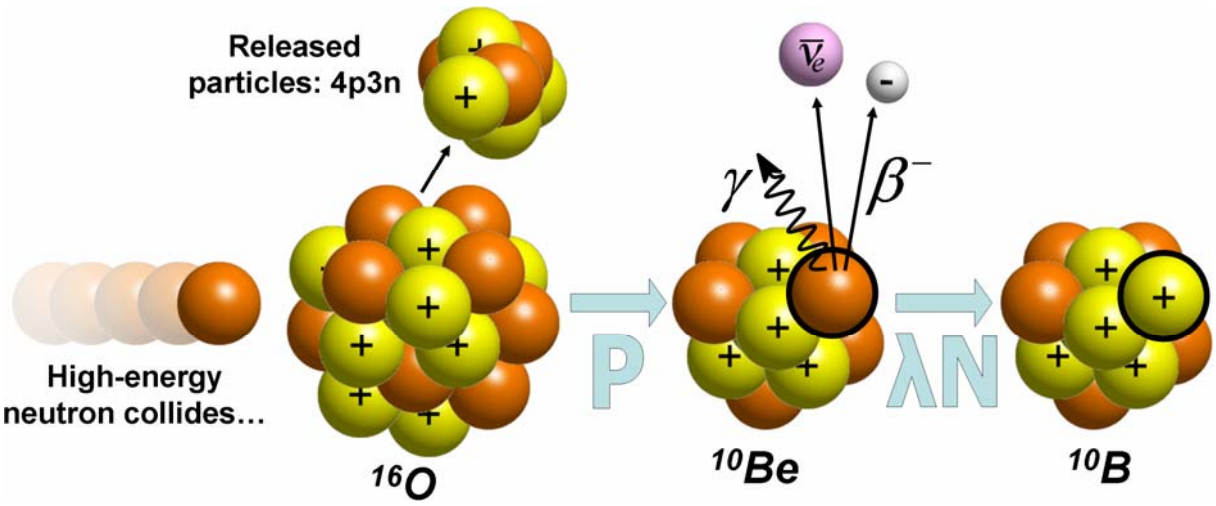

Figure 6: Schematic representation of the ^{10}Be geochronometer.
High-energy neutrons (left) collide with lattice atoms of oxygen in the rock, creating spall particles (4p3n) and converting ^{16}O into ^{10}Be, at a constant rate (P). The decay rate of radioactive ^{10}Be is proportional at all times (through the decay constant λ) to its instantaneous concentration (N). Exposure dating is possible until the two fluxes (P and λN) equilibrate.

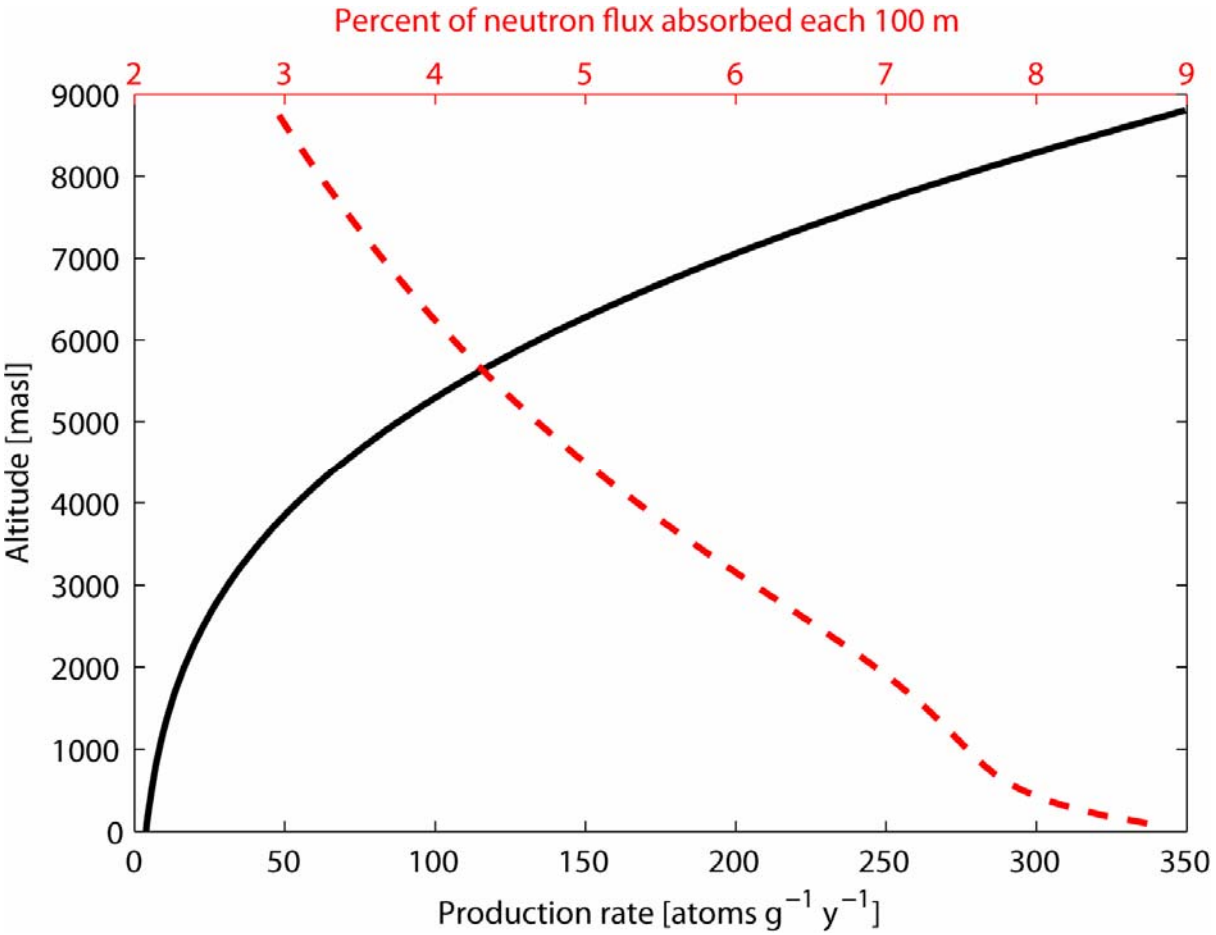

Figure 7: Altitude-dependency of cosmogenic production rate at latitude 30°.
The production rate of ^{10}Be at latitude 30° (black curve) drops from 349.4 atoms g^{-1} y^{-1} at 8800 masl (~top of Mt. Everest) to just 3.8 atoms g^{-1} y^{-1} at mean sea level. The relative absorption of the cosmic flux for each 100 m traversed (red dashed curve) rises from ~3% at 8800 masl to ~9% at mean sea level. Note: based on SLHL production rate of 4.58 atoms g^{-1} y^{-1} (Fink and Smith, 2007), scaling of Stone (2000). The "knee" in the red dashed curve (two inflection points at 2850 masl and 1085 masl) is a byproduct of the polynomial form of Lal's (1991) scaling factors.

For an unstable cosmogenic isotope, the combined effect of in-situ production at a constant rate (P), and radioactive decay proportional to concentration ($-\lambda N$; see Figure 6) is the following relationship of concentration with time:

$$N(t) = \frac{P}{\lambda}\left(1 - \exp(-\lambda t)\right) \quad (1)$$

Equation (1) describes "the rise of activity to a constant maximum of a system consisting of radiating particles in which (i) the rate of supply of fresh radiating particles is constant and (ii) the activity of each particle dies down geometrically with the time" (Rutherford and Soddy, 1902). This is a "classic" geochronometer which can date the exposure of a rock to cosmic rays for periods of up to 3 – 4 half-lives (for a radioisotope) or to infinity (for a stable isotope; Faure and Mensing, 2005).

The concept of surface exposure dating using in-situ cosmogenic isotopes was first proposed by Davis and Schaeffer (1955), who used ^{36}Cl to determine the exposure age of a deglaciated surface in the Rocky Mountains, Colorado. With the advent and standardization of AMS analysis, exposure ages were reported from all around the world (e.g., Srinivasan, 1976; Klein et al., 1986; Phillips et al., 1986; Leavy et al., 1987; Kurz et al., 1990; Brown et al., 1991). The chemical composition of quartz (consisting of Si and O, two of the most important target elements for ^{26}Al and ^{10}Be, respectively) and its widespread occurrence in terrestrial rocks gave rise to its extensive use for cosmogenic dating of fluvial sediments (Lal and Arnold, 1985). Under further different assumptions, the concentrations of cosmogenic isotopes can be alternately interpreted in terms of bedrock erosion or uplift rates (e.g., Lal, 1991; Brown 1991), burial ages of sediments (e.g., Granger and Muzikar, 2001) and sediment generation and transport rates (e.g., Bierman and Steig, 1996).

Sampling and labwork

Three types of cosmogenic isotope samples were collected in this study: (i) sediment from active channels which allow the quantification of basin-wide average erosion rates, (ii) sediment, boulders, and desert pavement samples from alluvial terraces. These samples allow the exposure dating of a terrace since its abandonment and reconstructing vertical tectonic movements through time (iii) deeply buried sediment in which the ^{26}Al/^{10}Be ratio indicates the time of deposition. Samples consisting of alluvial deposits were dissolved in 32% HCl and sieved to the 0.25 – 0.85 cm fraction. Desert pavement samples were leeched for 24 hours in 32% HCl and 70% HNO_3 to remove their varnish. To see the effect of patina dissolution, our

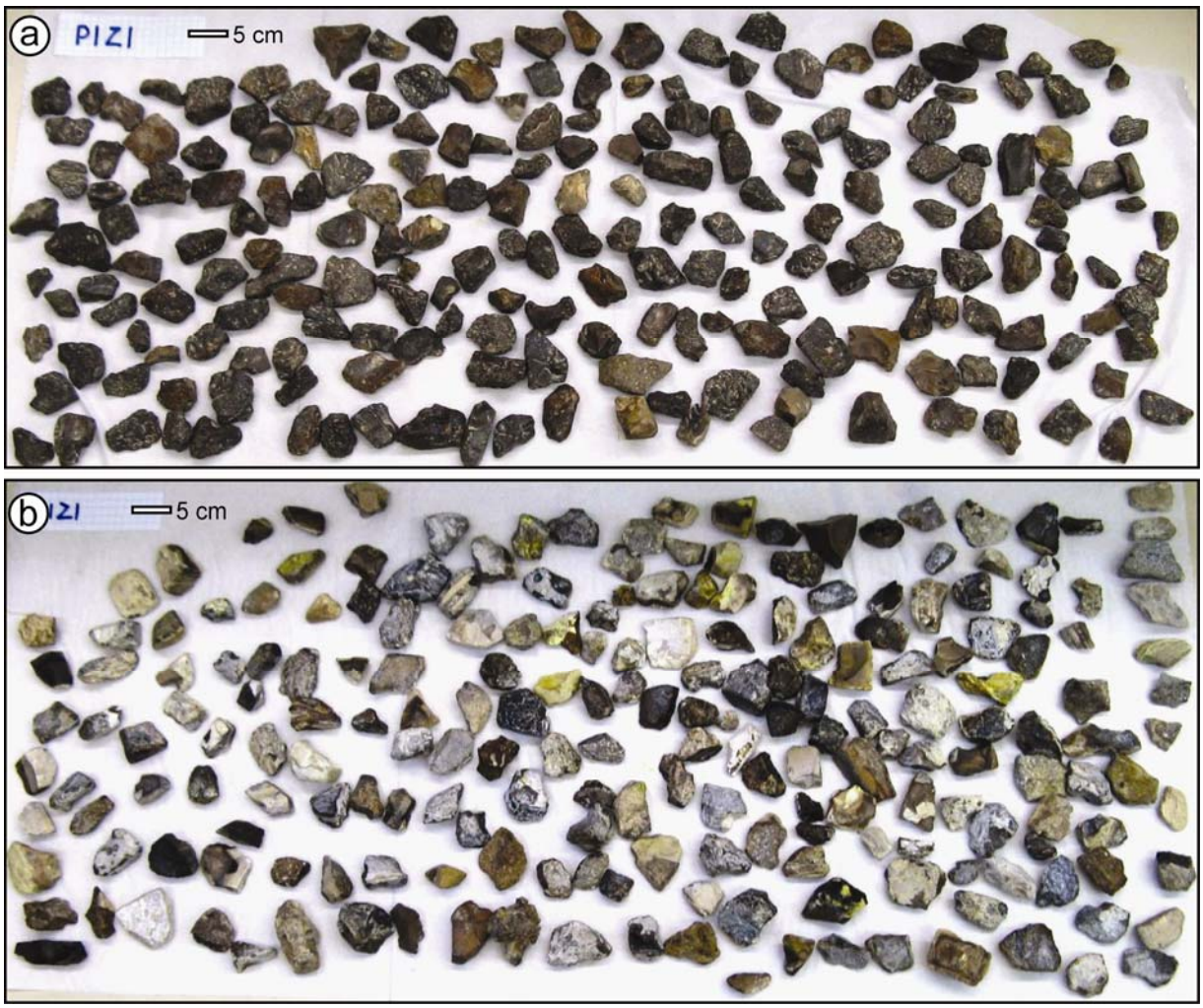

Figure 8: Dissolution of desert pavement patina
Desert pavement of sample MK (P1-Z1-DP) a) before the chemical treatment b) after a 24-hr leech in concentrated HCl and HNO_3.

first desert pavement samples were crushed to 0.25 – 0.85 cm only after the leech (Figure 8). Subsequent samples were crushed before the leech.

Subsequent extraction and separation of BeO from all samples followed standard techniques (Bierman and Caffee, 2001). $^{10}Be/^{9}Be$ ratios of 41 samples were determined at the ANTARES Accelerator Mass Spectrometry (AMS) facility at the Australian Nuclear Science and Technology Organization (ANSTO) (Fink et al., 2004; Fink and Smith, 2007). $^{10}Be/^{9}Be$ ratios of four other samples (KZ, PS8 in this work; PS4, PS6 in Matmon et al., 2009) were measured at the Lawrence Livermore National Laboratory (LLNL). As new values have been reported recently for $^{10}Be/Be$ ratios of AMS standards in use at both LLNL and ANTARES (Nishiizumi et al., 2007; Fink and Smith, 2007) we took care in assuring that normalization of all $^{10}Be/Be$ ratios conformed to a self-consistent pair of nominal values (namely 28500×10^{-15} for 07KNSTD3110 and 27900×10^{-15} for NIST SRM 4325, respectively) and the corresponding new value for the ^{10}Be half-life (1.36±0.07 Ma). In converting concentrations

to exposure ages, we adopt the scaling factors of Stone (2000) and correspondingly reduce the previous accepted sea-level high-latitude production rate of 5.08 atoms g^{-1} y^{-1} to 4.58 ^{10}Be atoms g^{-1} y^{-1} (which includes a 2.5% contribution from muon production at the Earth's surface).

2.2. Optically Stimulated Luminescence (OSL)

The OSL method dates the last exposure of mineral grains (such as quartz, feldspars, aluminum oxide) to sunlight (Aitken, 1998). While in the dark, excited electrons are trapped at an approximately constant rate in sites such as imperfections of the lattice, impurities, or defects. Thus, the number of trapped electrons grows as a function of time and surrounding radiation. Decay of nearby radioactive minerals and cosmic radiation are the main triggers for electron excitement, thus, their concentration must be measured. Under stimulation of light the electrons may free themselves from their traps and emission of light will occur. The emission intensity is a function of the number of trapped electrons and can be interpreted in terms of the time elapsed since the last exposure to light. Only several minutes of light exposure are necessary to zero the OSL in quartz (Aitken, 1998). The number of trapped electrons in the mineral grains is not infinite. It may reach a maximum concentration (termed the saturated concentration), thus, limiting the dating method to the 10^5 yr time frame, generally between 300 – 400 ka.

To prevent exposure to sunlight, a layer of tens of centimeters was scraped back from the vertical face of the terrace in the dark before collecting the OSL samples into a light-proof bag. All subsequent laboratory procedures were carried out under subdued orange light. Fine sand-sized quartz (88–125 μm and 125–177 μm) was separated and purified using standard laboratory procedures (Zilberman et al., 2000; Porat, 2007). OSL measurements were carried out on a Risø DA-12 TL/OSL reader. Equivalent doses (De) were determined using the standard single aliquot regenerative dose (SAR) protocol (Murray and Wintle, 2000), using preheats of 10 seconds at 220°C-260°C. The De used for age calculations was averaged from repeated measurements of up to 19 aliquots per sample. Samples had recycling ratios mostly within 10% of 1.0 and negligible IR signals. Annual γ and cosmic dose rates were measured in the field in the same holes dug for sampling, using a portable gamma scintillator. Dose rates of α and β radiation were calculated from the concentrations of the radio-elements U, Th, and K in the sediment, measured by ICP-MS and ICP-AES at the Geological Survey of Israel.

3. Tectonic and drainage evolution of the Negev in the Quaternary

3.1. Cosmogenic paleo-elevation studies

Elevation changes are one of the most pronounced expressions of tectonic deformation. Thus, quantification of the temporal and spatial scales of these changes is of major importance in tectonic research. Paleoaltimetric studies have mainly focused on the uplift of the largest plateaus and mountain ranges of the world. The potential application of surface production of cosmogenic isotopes for paleoaltimetry has previously been recognized (e.g., Lal, 1991; Blard et al., 2005, 2006) due to the known attenuation dependence of the galactic cosmic ray flux with increasing atmospheric depth. This dependence is largest at low altitudes and high latitudes, suggesting that even small altitude changes may be detectable. However, the rate of paleo-elevation change would need to exceed rock erosion rates by 2 – 3 orders of magnitude to be detected using in-situ nuclide concentrations (Lal, 1991). Consequently, regions that experience either extremely slow erosion or rapid vertical movement are preferred settings for studies of paleo-elevation change. Only a few cosmogenic studies attempted to detect large-scale vertical tectonic movements (Craig and Poreda, 1986; Brown et al., 1991; Cerling and Craig, 1994; Brook et al., 1995; Bruno et al., 1997; Schäfer et al., 1999); successful results have been attained so far only in Antarctica, where cosmogenic production rate and its dependence on altitude are maximal and erosion is minimal.

In the present study, we combine geologic and geomorphologic data from modified fluvial systems along the western margins of the Dead Sea Rift, southern Israel, with new cosmogenic exposure ages to (i) constrain the temporal evolution of the drainage systems during the late Pliocene and early Pleistocene, and (ii) reconstruct the subsidence history of the Dead Sea Rift's western margin. Our results provide extensive direct dating of early Pleistocene abandoned fluvial surfaces and establish the use of cosmogenic exposure age dating of desert pavements to date ancient surfaces in hyperarid environments. We also successfully test the use of cosmogenic isotopes in reconstructing tectonic subsidence along the margins of an active rift boundary.

3.2. Methods and study sites

The concentration (N) of a radionuclide with a decay constant (λ), produced in a freshly exposed rock (with zero initial concentration) by high-energy particles at a constant rate (P) over an irradiation time (t), is given by:

$$N(t) = P \cdot \lambda^{-1} \cdot \left(1 - \exp(-\lambda t)\right) \tag{2}$$

(Lal, 1991). Since the intensity of cosmic-ray irradiation reduces exponentially with the thickness of the atmosphere and depth of the shallow lithosphere, the production rate cannot be considered constant if during its exposure, the irradiated surface experiences altitude changes or surficial alteration such as erosion or sedimentation. Taking into account the effects of uplift rate (U [m/Ma], negative for subsidence), and erosion rate (ε [m/Ma], negative for sedimentation), Equation (1) becomes:

$$N(t, U, \varepsilon) = P \cdot (\lambda + MU + \mu\varepsilon)^{-1} \left(1 - \exp\left(-t / (\lambda + MU + \mu\varepsilon)^{-1}\right)\right) \tag{3}$$

where $\left(\lambda + MU + \mu\varepsilon\right)^{-1}$ is the "effective irradiation time", and M, μ are the reciprocals of atmospheric and rock attenuation lengths, respectively (Craig and Poreda, 1986; Lal, 1991; Brown, 1991; Cerling and Craig, 1994). If the ratio between the cosmogenic concentration (N) and the in-situ production rate (P) has been determined for a sample, its true exposure age may be expressed as a function of uplift and erosion rates:

$$t(U, \varepsilon)_{N/P} = -(\lambda + MU + \mu\varepsilon)^{-1} \cdot \ln\left(1 - N / P / (\lambda + MU + \mu\varepsilon)^{-1}\right) \tag{4}$$

Where erosion is insignificant (e.g., Brown, 1991; Matmon et al., 2009), the true exposure age becomes a function of uplift rate alone, and may be represented by a continuous curve relating the two unknowns (Figure 9). A convenient reference point on this curve is the apparent or "simple" exposure age (a singular solution for $U \equiv \varepsilon \equiv 0$), which will *underestimate* or *overestimate* true exposure age, if the surface has uplifted or subsided, respectively (Figure 9). The modeled uplift rates are necessarily time-averaged rates over the respective true exposure time since measured cosmogenic concentrations integrate production rates which vary over time due to a changing altitude; the actual instantaneous rates during exposure may differ from the time-averaged rate, unless a constant rate is assumed.

Our sampling strategy was based on the assumptions, that: (i) the resistant chert clasts of desert pavements in the Negev do not erode, and continuously reside in the topmost soil layer via a mechanism of dust accumulation underneath the clasts (Amit and Gerson, 1986; McFadden et al., 1987; Amit et al., 1993; Wells et al., 1995; Matmon et al., 2009), (ii) the process of stream abandonment and progressive subsidence of ancient stream relicts can be

reconstructed by comparing the abandonment ages of tectonically stable surfaces to ages of subsided surfaces (iii) the selected "reference" surface has indeed been tectonically stable. If surfaces are contemporaneous and were abandoned simultaneously, simple exposure ages will increase (compared to the exposure age of the tectonically stable "reference" site) towards areas of greater subsidence (cf. simple exposure ages of A and B, Figure 9). If, on the other hand, simple exposure age decreases as subsidence increases, an asynchronous abandonment must be considered (cf. simple exposure ages of A and C, Figure 9)

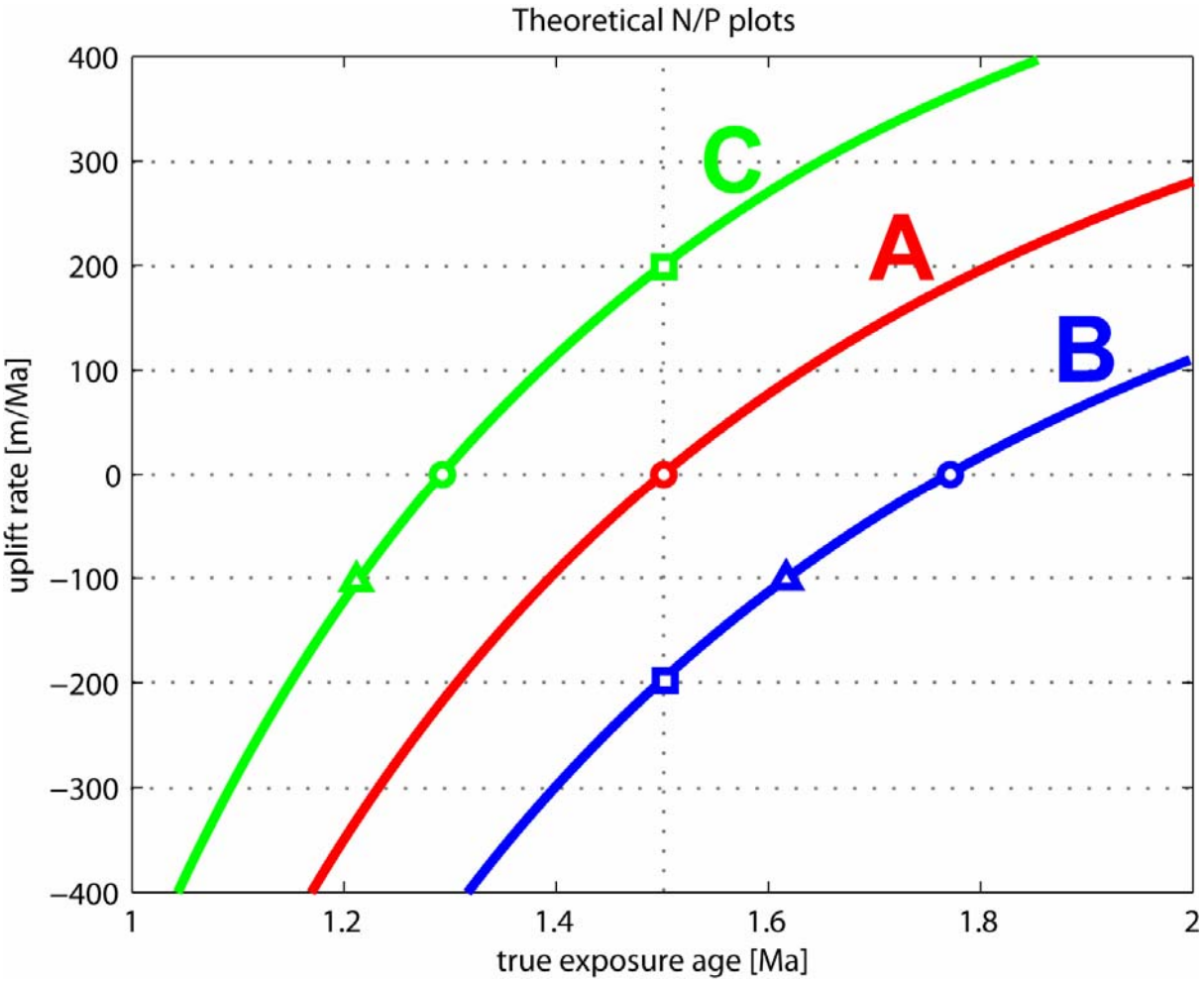

Figure 9: Theoretical N/P plots.
Three curves with constant but different N/P ratios (letters refer to hypothetical samples) showing the continuous combinations of exposure age vs. tectonic signal for a given N/P ratio. Circles represent “simple” exposure ages. A) sample from a tectonically stable area (no elevation change) whose simple exposure age (1.5 Ma) may be treated as the true exposure age. B,C) samples from *a tectonically active region*. If B and C are contemporaneous with A, then B has subsided at an average rate of 200 m/Ma and C was uplifted at an average rate of 200 m/Ma (indicated by squares). However, if B and C are independently known to have subsided at a rate of 100 m/Ma (indicated by triangles), then B must be older than A and C younger.

Figure 10: Desert pavement properties
a) A soil pit at site EZ. Dust which penetrates beneath the desert pavement clasts accumulates into a thick gravel-free B horizon; the clasts remain constantly above and "afloat" the fine material, being exposed from the time of fluvial surface abandonedment (e.g., Amit et al., 1993, 1996) b) Close-up on topmost soil and desert pavement at site MK (water divide between Paran and Neqarot basins). Notice the gravel at the bottom of the picture (suspended in the B horizon), which were originally just a few cm below the desert pavement gravels, and are now separated by ~15 cm of aeolian dust c) Close-up on desert pavement at site ES, showing the "optimal" gravel size of 2 – 3 cm.

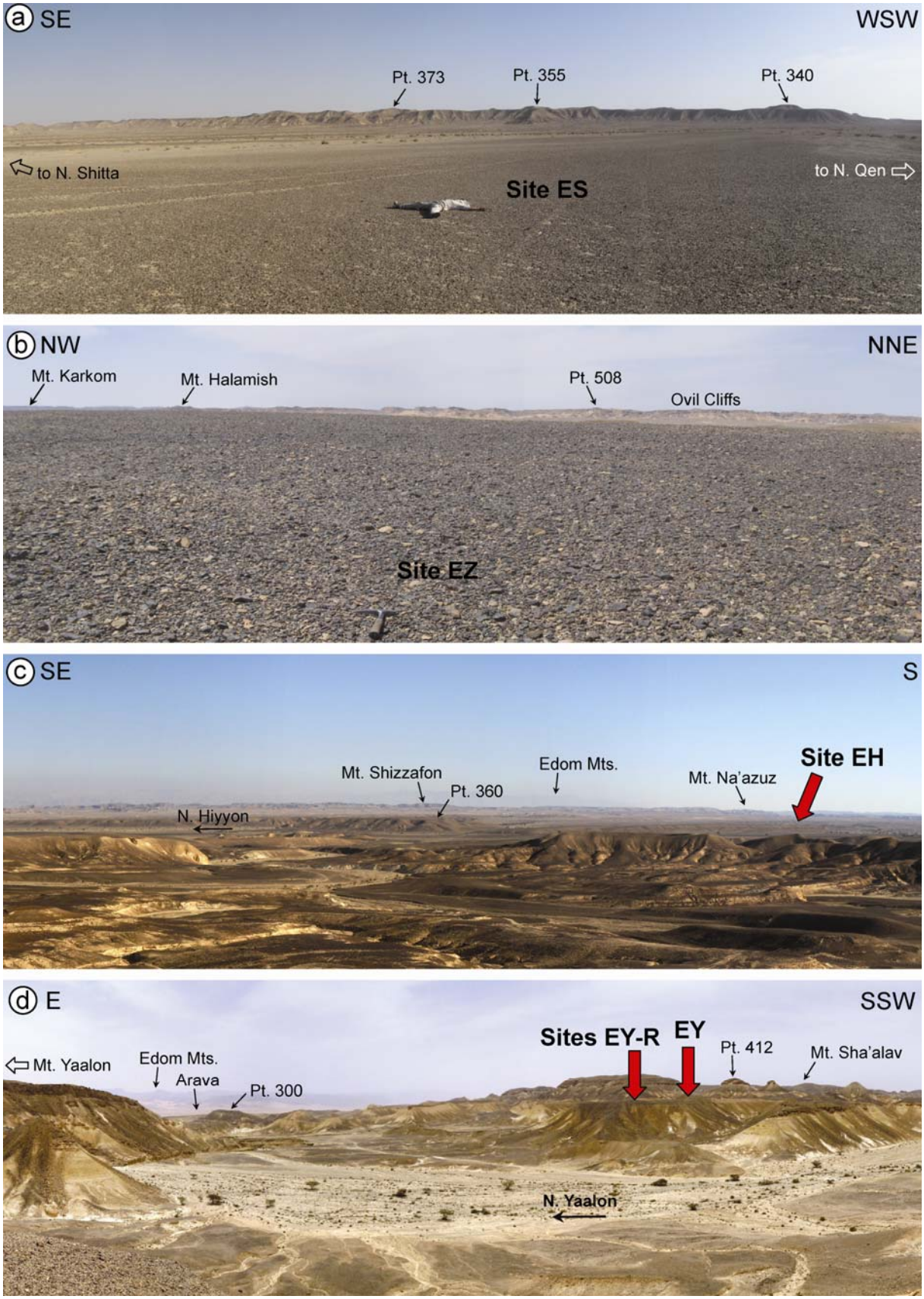

Figure 11: Sites along the Edom River.
a) Site ES (water divide between Shitta and Hiyyon basins; see figure 4 for all locations). b) Site EZ (water divide between Hiyyon and Paran basins). c) Site EH (a high terrace within the Hiyyon valley) d) Site EY (a high terrace within the Yaalon valley)

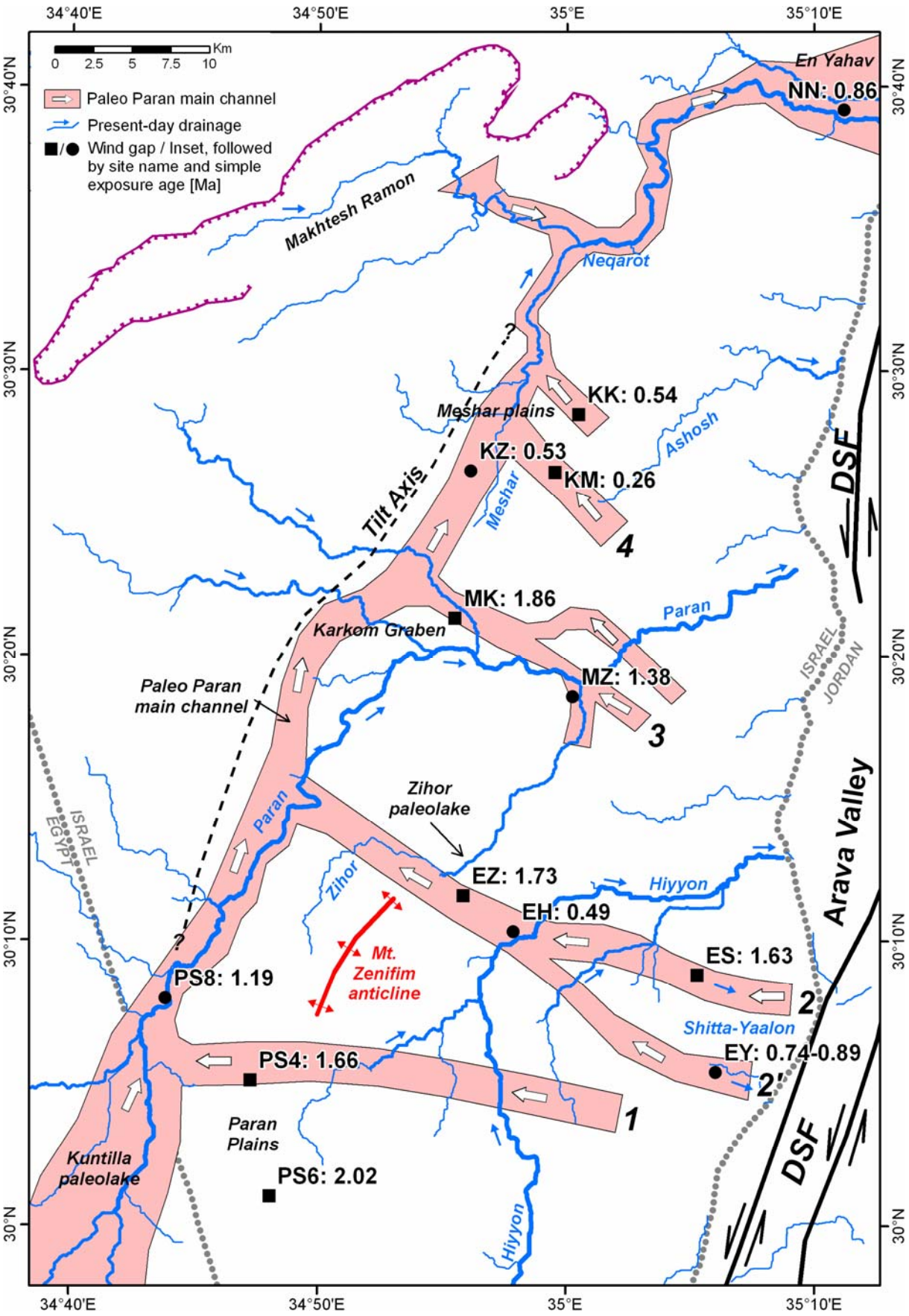

Figure 12: Spatial distribution of terrace abandonment ages across the Negev.
Present-day drainage basins are outlined in blue, reconstructed paleo-Paran drainage in pink (arrows indicate flow direction). Major westward-flowing paleo-tributaries are numbered: 1 – Zenifim, 2 – Edom Channel (Shitta facies), 2' – Edom Channel (Yaalon facies), 3 – Menuha, 4 – Kippa. Major Dead Sea faults (DSF) in black, Quaternary tilt axis in dashed black line. Sample locations and their simple exposure ages are indicated. Sources for reconstruction: Ginat (1997), Ginat et al. (1998), Avni (1998), Ginat et al. (2000), Avni et al. (2000).

In this study, we addressed only those sites where a mature desert pavement had developed on top of abandoned late Pliocene (Arava Formation; Avni et al., 2001) and early Pleistocene (Zehiha Formation; Ginat et al., 2002, 2003) fluvial and lacustrine deposits. Three wind gaps between the Paran and Hiyyon basins (sites PS4 and PS6; Figure 12; Matmon et al., 2009), and Paran and Neqarot basins (site MK; Figure 10b; Figure 12) are considered as tectonically stable (Avni et al., 2000); four other wind gaps are located in progressively subsided areas and include the water divides between Shitta and Hiyyon basins, (ES; Figure 10c; Figure 11a), Hiyyon and Paran (EZ; Figure 10a; Figure 11b), and Ashosh and Neqarot (KM and KK). The seven remaining surfaces are found within the current basins of Paran (PS-8), Yaalon (EY; Figure 11d), Hiyyon (EH; Figure 11c), Zihor (MZ), Meshar (KZ) and Neqarot (NN), and formed during the incision stages of the current drainage network, post-dating the abandonment of the wind gaps.

At each targeted site, pits were dug and soil profiles were inspected (Figure 10a,b) to assure soil development stage is the most mature (Stage E of Amit et al., 1993, 1996) and that the pavement did not develop on top of an eroded soil section. At our sample sites hundreds of overlying desert pavement clasts were collected (25 – 40 clasts are sufficient to achieve a representative mean concentration in a geomorphic system; Repka et al., 1997).

3.3. Results: abandonment ages of water divides and terraces in the central Negev

Exposure ages, assuming zero inheritance, zero erosion and no vertical tectonic movement during irradiation are given as two groups (wind gaps and insets) in Table 1. Five out of seven paved alluvial surfaces at wind gaps yielded the highest ^{10}Be concentrations ranging between (7.252 ± 0.197) to (5.115 ± 0.128) × 10^6 atoms g^{-1} SiO_2, which correspond to "simple" exposure ages of 2.02 ± 0.37 Ma and 1.63 ± 0.27 Ma, respectively (Table 1, Figure 12). The two remaining wind gap samples from the eastern Meshar basin (KK and KM) yielded in comparison far younger ages of 0.54 Ma and 0.26 Ma, relating to cliff retreat and water divide migration processes affecting the eastern Meshar basin. These two samples were not considered later in our tectonic interpretation. All inset terraces, situated below the present water divides, yielded lower ^{10}Be concentrations, ranging from (4.801 ± 0.148) to (2.167 ± 0.053) × 10^6 atoms g^{-1} SiO_2, which correspond to simple exposure ages of 1.19 ± 0.17 Ma and 0.49 ± 0.06 Ma, respectively. Ages of two samples (EY and EY-R) collected 130 m apart from the same inset terrace above the Yaalon stream (0.89 ± 0.12 Ma and 0.74 ± 0.09 Ma) are in good agreement (at the 1σ) demonstrating an acceptable level of geologic variability.

Table 1: Simple exposure ages for Central Negev desert pavement samples.

Sample Name	Location Lat / Long	Elevation [masl]	^{10}Be [10^6 atoms g^{-1}]	Simple exposure age [Ma]
Windgaps				
KK	30°28.467' / 35°00.500'	388	2.442 ± 0.063	0.54 ± 0.06 (0.02)
KM	30°26.451' / 34°59.546'	405	1.291 ± 0.054	0.26 ± 0.03 (0.01)
MK	30°21.319' / 34°55.515'	383	6.157 ± 0.142	1.86 ± 0.32 (0.07)
EZ	30°11.585' / 34°55.856'	433	6.099 ± 0.148	1.73 ± 0.29 (0.07)
ES	30°08.795' / 35°05.304'	255	5.115 ± 0.128	1.63 ± 0.27 (0.06)
PS4	30°05.089' / 34°47.304'	522	6.349 ± 0.176	1.66 ± 0.28 (0.07)
PS6	30°01.020' / 34°48.076'	545	7.252 ± 0.197	2.02 ± 0.37 (0.10)
Insets				
NN	30°39.189' / 35°11.228'	-5	2.611 ± 0.066	0.86 ± 0.11 (0.03)
KZ	30°26.494' / 34°56.137'	380	2.396 ± 0.065	0.53 ± 0.06 (0.02)
MZ	30°18.578' / 35°00.263'	275	4.677 ± 0.129	1.38 ± 0.21 (0.06)
EH	30°10.323' / 34°57.886'	355	2.167 ± 0.053	0.49 ± 0.06 (0.01)
PS8	30°07.959' / 34°43.866'	450	4.801 ± 0.148	1.19 ± 0.17 (0.05)
EY	30°05.412' / 35°06.113'	331	3.504 ± 0.115	0.89 ± 0.12 (0.04)
EY-R	30°05.383' / 35°06.035'	328	3.012 ± 0.081	0.74 ± 0.09 (0.02)

Note: Simple exposure ages are ordered north to south (as shown in Figure 12) and are based on present day site altitude. A ^{10}Be half-life of 1.36 ± 0.07 Ma (Nishizumi et al., 2007), Sea Level High Latitude (SLHL) production rate of 4.58 ^{10}Be atoms g^{-1} SiO_2, attenuation length of 150 ± 4 g cm^{-2} and latitude-altitude scaling factors of Stone (2000) were used for all age calculations. Internal uncertainty in age (in brackets) represents the analytical uncertainty (including a 2% reproducibility error of AMS standards). External uncertainties include an additional 10% error in reference production rate and scaling factors (Lal, 1991). Sample names in italics were measured at LLNL. EY-R is a repeat sample taken from same terrace 130m from sample EY.

Table 2: Calculated paleo elevations of central Negev surfaces

Name	Distance from tilt axis [km]	Elevation [masl]			Elevation change [m]	
		Present	During reversal	Initial	Since initial	Since reversal
	D	Z	Z_0	Z_i	dz_i	Dz_0
KK	7	388	400	431	-43	-12
KM	7	405	400	432	-27	5
MK	7	383	400	432	-49	-17
EZ	17	433	450	526	-93	-17
ES	33	255	450	599	-344	-195
PS4	2	522	500	509	13	22
PS6	2	545	520	529	16	25

Note: D, Z and Z_0 are given constants calculated from a geological map. D is site distance from the tilt axis (fig. 4), Z is present site elevation, and Z_0 is the elevation of the most proximate Arava Formation outcrops at the tilt axis. $Z_i = Z_0 + D \times 0.0045$; $dz_i = Z - Z_i$; $dz_0 = Z - Z_0$.

The reconstruction of paleo-elevations of Pliocene and Pleistocene deposits in the Negev can be described via local displacements relative to a "tilt axis" (Figure 2c, Figure 12) which lies within a confined and narrow region between uplifted and subsided areas and which by definition would have experienced a net zero elevation change during the Quaternary transition of the drainage system. The tilt axis is traditionally associated with the NNE-trending paleo-Paran main channel (Figure 12), along which the present-day streams are

usually incised only tens of meters below the Pliocene deposits (Avni et al., 2000). At the Paran Plains (Figure 12; sites PS4, PS6), the net zero elevation change area occupies a broad belt of several km, due to influence of the Mt. Zenifim anticline (30.16° N, 34.86° E), a local Quaternary uplift structure (Figure 12). Consequently, sites PS4 and PS6 are considered to represent a best choice for a relatively stable tectonic environment (Matmon et al., 2009).

Initial Pliocene elevations at the wind gaps listed in Table 2 were reconstructed by extrapolating a westward paleo-gradient of 4.5‰ (analogous to the gradient of major, present-day streams in the Negev) from the tilt axis to the east. Reported site distance from the tilt axis (Table 2, column 2) is assumed to be within an uncertainty of ±2 km. During the stream direction reversal episode, identical sediments (Zehiha Formation) were deposited at tilt the axis and at the current wind gaps when both formed a planar surface and were all at equal altitudes. Ongoing eastward titling changed the altitudes of these deposits at the emerging wind gaps but not at the tilt axis. Sediments found closest to the tilt axis were less affected by tilting than those found in wind gaps away from the tilt axis. We determine wind gap elevation at the time of reversal by locating wind gap deposits at the tilt axis location which is closest to the wind gap sampled for comsogenic isotopes. Total elevation change at each wind gap since initial elevation Table 2, column 6) and since the *stream reversal stage* (Table 2, column 7) were calculated by subtracting its present elevation from the extrapolated ones as described above. Since the amount of subsidence at the inset terraces is further complicated by the amount of vertical incision subsidence of these landforms was not considered.

3.4. Discussion

Age uncertainty

Two types of uncertainty can be attributed to cosmogenic exposure ages (Balco et al., 2008): (i) "internal" uncertainty, associated solely with the quality of the AMS measurement, and useful for comparing exposure ages of samples from a single study area, and (ii) "external" uncertainty, arising from latitude-altitude scaling errors and time dependent variations in site specific production rates (e.g., Stone, 2000; Lifton et al., 2005, 2008), choice of a reference calibration site (e.g., Stone, 2000; Desilets et al., 2006), and the error in its independent age (e.g., Clark et al., 1995). The external uncertainty may be used for comparing the ages of widely separated samples, or for evaluating cosmogenic ages against an independent different geochronometer. All the wind gaps sites addressed in this study are located within a narrow elevation range of 250 – 550 masl and situated only tens of km apart from each other. We

assume they experienced the same geomagnetic, solar, and atmospheric variations, and that their ages are comparable within their internal uncertainties alone. While improved scaling factors and SLHL production rate in the future may require shifting the exposure ages reported here, their relative differences are expected to be maintained.

Age uncertainties arising from assuming erosion and inheritance are considered below. Generally, these two processes affect calculated exposure ages in opposing ways: the application of a typical erosion rate for all samples of similar lithology and locality result in increased model ages whereas the more variable effect of inheritance results in decreased ages. Since the extremely high concentrations of ^{10}Be measured in wind gap samples are not far below their site-specific saturation values, surface erosion rates cannot exceed 0.2 – 0.3 m/Ma (Matmon et al., 2009). However, applying such erosion rates throughout the $>10^6$ year lifetime to a <10 cm clasts would have clearly caused them to completely disappear. Since this is not the case, desert pavement clasts must experience an effective zero erosion rate after they reach their optimal size and thickness. Inheritance values from previous exposures in chert in the hyper arid environment of the central Negev was determined was constrained by 5 depth samples at site PS4 to only ~3.2×10^5 atoms ^{10}Be (Matmon et al., 2009); correcting for such inheritance would result in a negligible age reduction of ~3%.

Basin delineation stages

Plotting all simple exposure ages against their distance from the tilt axis (fig 5) provides strong evidence for 3 distinct episodes of Plio-Pleistocene fluvial evolution: (i) *Early abandonment*: the paleo Paran fluvial system started to collapse in the late Pliocene, as indicated by the oldest wind gap age (PS6) of ~2 Ma. (ii) *Establishment of present water divides:* the abandonment ages of wind gaps PS4, PS6, MK, EZ, and ES are tightly clustered and overall are independent of site distance from the Quaternary tilt axis. An average wind gap age of 1.8 ± 0.2 Ma (internal error propagated, KK and KM sites omitted) indicates that the episode of collapse of the paleo-Paran drainage lasted for about 400 ka, similar to the drainage reversal period which has been recently reported from the East African Rift (Holzforster and Schmidt, 2007). This age supports the earlier correlation between the Zehiha and 'Ubeidiya formations (Ginat et al., 2003), for which an age of 1.4 Ma was suggested on the basis of long-range biochronological correlations with Europe (Tchernov, 1987). (iii) *Incision of the present basins*: Continuous fluvial incision in the Negev between 1.6 Ma and 0.3 Ma, reflects fluvial response to the base level lowering within the outlines of the present drainage basins and is perhaps also controlled by climatic cycles (i.e., the first stage of

shaping the landscape of the southern Negev was mainly influenced by tectonics; when the tectonic influence diminished, the climatic signal on landscape evolution came to be manifested.)

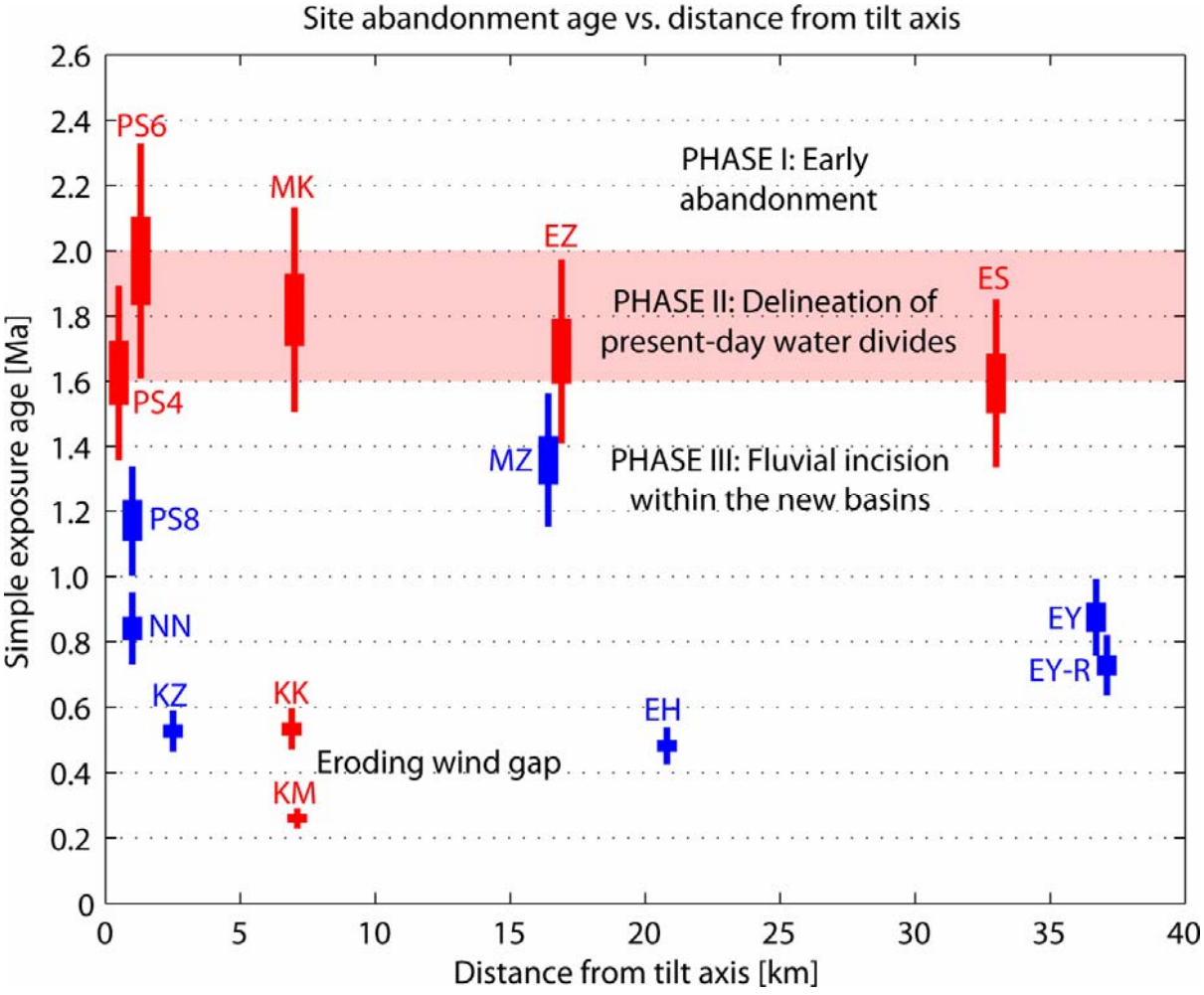

Figure 13: Simple exposure ages of desert-pavements.
The ages of wind gaps (red) and inset surfaces (blue) are plotted against their distance from the Quaternary tilt axis. Internal and external uncertainties are indicated by thick and thin bars, respectively (see section 3.4). Excluding the anomalously young ages of wind gaps at the Meshar basin (KK and KM), the average wind gap age is 1.8 ± 0.2 Ma (marked by the red band).

3.5. Subsidence scenarios

It is likely that during the *stream reversal stage*, the original boundaries and leveled stagnating channels of the paleo-Paran basin would have been overprinted by deposition of the autochthonous Zehiha Formation (Avni et al., 2000). As a result, we assume that this process would reset the in-situ cosmogenic clock of the majority of alluvial surfaces across the Negev. The new and emerging eastward-oriented drainage channels gradually incised below the nearly planar "datum surface" of the *stream reversal stage* leaving but a few isolated relict surfaces preserved above and in-between the newly-formed basins. Some of the wind gaps which experienced differential subsidence towards the rift must have remained

practically unaltered due to the hyperarid climate and prolonged isolation from the new network of active streams. Therefore, cosmogenic concentrations in these surfaces may contain a tectonic signal which can be used to unravel the subsidence history of the Negev since the *stream reversal stage*.

Vertical tectonic motion postdating the deposition of a fluvial "marker" can be inferred only when the amount of displacement exceeds the unit's thickness; smaller changes may reflect local erosion or original thickness variations. In the central and southern Negev, the thickness of the Plio-Pleistocene sequence is typically several tens of meters. Thus, significant vertical motion since the *stream reversal stage* (~200 m, Table 2) may be confidently inferred only for a single site ES, situated near the Arava valley. This is one of four sites (EY, ES, EH and EZ) sampled along the east-to-west flowing ancestral "Edom River" (Figure 12), a ~50 km long Pliocene stream, whose distinct deposits contain allochthonous gravel derived from crystalline and sedimentary rocks exposed only east of the Dead Sea Rift, in the Edom Mountains of Jordan (Lifshitz et al., 1985; Ginat et al., 2000). The relicts of this paleo-river can currently be found across four separate basins (Shitta-Yaalon, Hiyyon, Zihor and Paran) at progressively lower elevations towards the rift (Table 2). Two wind gap samples, EZ and ES, are preserved representatives of the *stream reversal stage* planar "datum surface", yielding an average simple exposure age of 1.68 ± 0.16 Ma (Table 1). However, from the tectonic standpoint these two sites are different. EZ was marginally affected by vertical displacement and thus its exposure age most closely reflects the true abandonment age. In contrast, the total subsidence of ES below the *stream reversal stage* datum is ~ 200 m, suggesting that its cosmogenic ^{10}Be concentration may incorporate a mixed "tectonic" and "exposure" signal. Possible scenarios of subsidence evolution, depending on modeling the cosmogenic concentration of desert pavement pebbles at ES, are presented in Figure 14 and are discussed below.

Subsidence preceding the formation of Desert Pavement

The most straightforward interpretation (scenario A; Figure 14) assumes that the desert pavement at ES began to form at its present-day elevation and only after the subsidence of the wind gap ceased. In such a scenario, the irradiation by cosmic rays occurred solely at the present-day altitude, and hence its simple exposure age of 1.63 ± 0.27 Ma must also be the *true age of abandonment*. Given the ~ 345 m of displacement, we obtain an *average* subsidence rate of ~ 200 ± 100 m/Ma from early Pliocene to the present-day. This rate is comparable to but somewhat slower than the 300 – 600 m/Ma subsidence rates proposed for

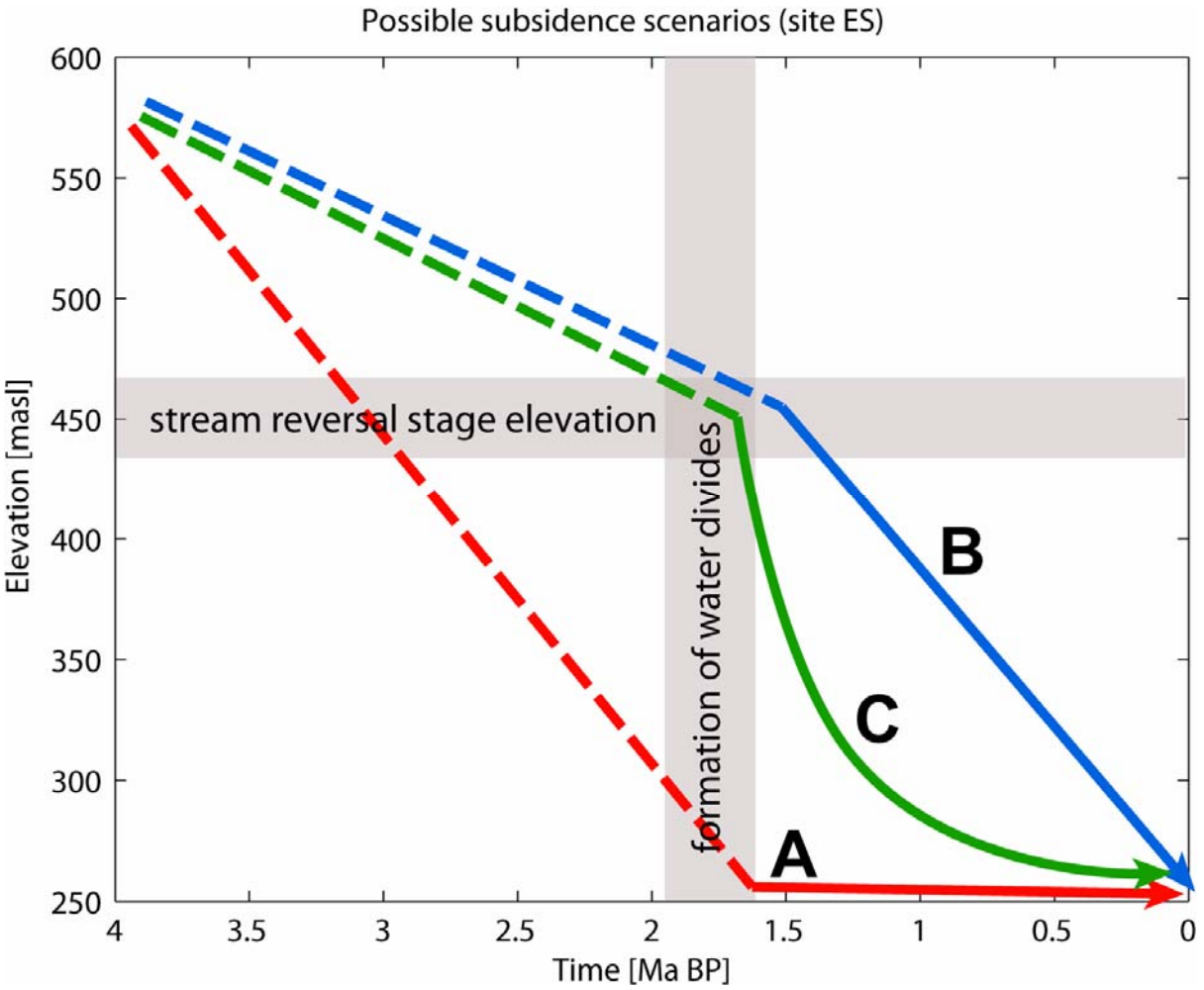

Figure 14: Possible subsidence scenarios for site ES.
Horizontal grey band represents the elevation of the paleo-Edom River during *stream reversal stage*. Vertical grey band – the age range of water divides. Colored lines represent subsidence scenarios. A: subsidence precedes the formation of desert pavement which has been continuously exposed at its present elevation; thus it only records age. B and C: desert pavement is formed during subsidence at a higher elevation than present; thus it records a mixed signal of age and subsidence, which is either considered to be constant (B), or variable (C).

the western margins of the Dead Sea basin (Bartov et al., 2006). However, the main weaknesses of this scenario is that it requires the *stream reversal stage* to have occurred sometime during the middle Pliocene (or at least prior to the oldest wind gap age of 1.8 – 1.9 Ma), contradicting the general model for the tectonic history of the western margin of the Dead Sea rift (Avni et al., 2000; Ginat et al., 2000) and specifically, the younger (early Pleistocene) age of the paleolake Zihor deposits associated with the *stream reversal stage* (Ginat et al., 2003). Furthermore, since the Zihor deposits contain a Lower Paleolithic hand tool assemblage (Ginat, 2003), the age of this unit cannot be older than the initial northward migration of hominids out of Africa at 1.5 – 2.0 Ma (Ron and Levi, 2001).

Subsidence at a constant rate, following the formation of Desert Pavement

In a more realistic approach (scenario B; Figure 14), the desert pavement at ES formed during the *stream reversal stage* and on abandoned surfaces at a significantly higher elevation than at

present (~200 m; Table 2). The gradual decrease in cosmogenic production rate due to regional subsidence would result in an apparent overestimated exposure age (i.e., using the production rate for today's altitude). The true exposure age may be evaluated by assuming a constant subsidence rate and using the age-subsidence rate curve for site ES as plotted in figure 7. A true age of 1.52 ± 0.07 Ma (internal error), and a constant subsidence rate of 129 ± 19 m/Ma are derived for site ES. For site EZ, the insignificant subsidence retains the exposure age at 1.69 Ma ± 0.10 Ma (internal error). The result yields a rather slow (110 – 150 m/Ma) subsidence rate at the Arava valley, and reduces the exposure age of sample ES by only ~100 ka from that given in Table 1 where one assumes simple constant exposure at today's elevation. This suggests that the eastern water divides may have been delineated ~300 ka later (i.e., at ~1.5 Ma) than similar basin boundaries to the west (at ~1.8 Ma). However, field observations suggest that the eastward-tilting process was morphologically more dominant in the early Pleistocene and decelerated towards the present time (Ginat et al., 1998, 2002).

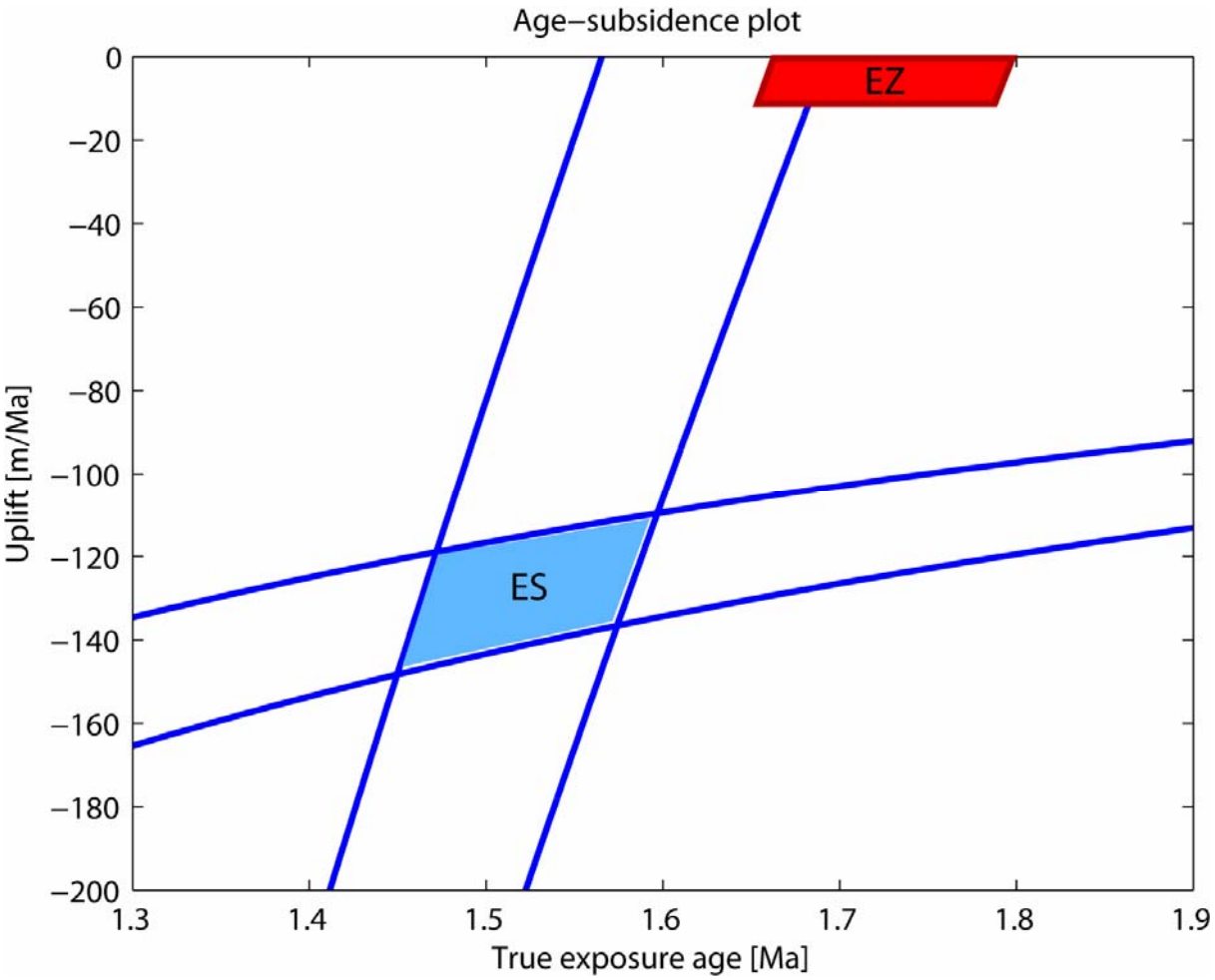

Figure 15: Age-subsidence plot for wind gap samples ES and EZ.
Sub-vertical band represents the N/P curve for site ES and sub-horizontal band is constrained by requiring all uplift and exposure age pairs to result in a –195±20 m elevation change as estimated from Table 2. Shaded areas represent the allowed true age – constant subsidence combinations at sites ES and EZ.

Subsidence at an unknown rate, following the formation of Desert Pavement

A constant subsidence rate serves as a convenient first-order approximation, but is contradicted by field evidence. We can solve for a *time-varying subsidence rate* by using an independent constraint on the true exposure age at site ES (scenario C; Figure 14) and maintain a total subsidence of ~200m. The nearby tectonically undisturbed site EZ is a high-standing relict of the Edom River, abandoned just prior to incision and accumulation of Zehiha Formation lake deposits. ES, on the other hand, represents the top of the Zehiha Formation. Hence sites EZ and ES date the base and the top of the same unit, respectively. The total accumulation period of the Zehiha sediments can be estimated using the rate of carbonate accumulation and soil formation in arid environments (Ginat et al., 2003). By subtracting the estimated accumulation time (0.12 ± 0.06 Ma; after Ginat et al., 2003) from the age of the formation's base as given by the simple exposure age of the undisturbed site EZ (1.73 ± 0.07 Ma), we obtain an independent age of 1.62 ± 0.09 Ma for the top of Zehiha Formation at ES. Although this value is numerically equivalent to the simple exposure age of ES (1.63 ± 0.06 Ma), it does not represent simple exposure at a fixed elevation, but rather is the length of time for which site ES, while exposed, underwent subsidence. Thus, cosmogenic isotope concentration at site ES incorporates a changing production rate due to lowering elevation.

To determine which subsidence histories best reproduce the ^{10}Be cosmogenic concentration measured at ES, we generated random monotonic time-elevation paths, starting at 1.62 ± 0.09 Ma at 450 masl, and ending today at 255 masl. Using these paths, the ^{10}Be concentration at ES was simulated by integrating Equation (2) over small time increments and using an altitude-dependant production rate P (*tecthist.m*, see Appendix 8.4). Figure 16 shows only those trajectories that successfully reproduced the observed concentration at ES within the analytical error; all other simulated paths are not shown. Despite the scatter, the mean subsidence paths display a clear trend of a diminishing tectonic activity with time, with a mean rate of ~350 m/Ma during 1.6 – 1.2 Ma and of ~35 m/Ma ever since 1.0 Ma. The cumulative average rate for the whole exposure history is 117 m/Ma. This result agrees with previous works, which recognized that the early Pleistocene tectonic phase was the main trigger for the reorganization and the readjustment of the paleo-Paran drainage basin (Avni et al., 2000), and that the tectonic activity has diminished since (Ginat et al., 2002). Hence, this scenario is the preferred one.

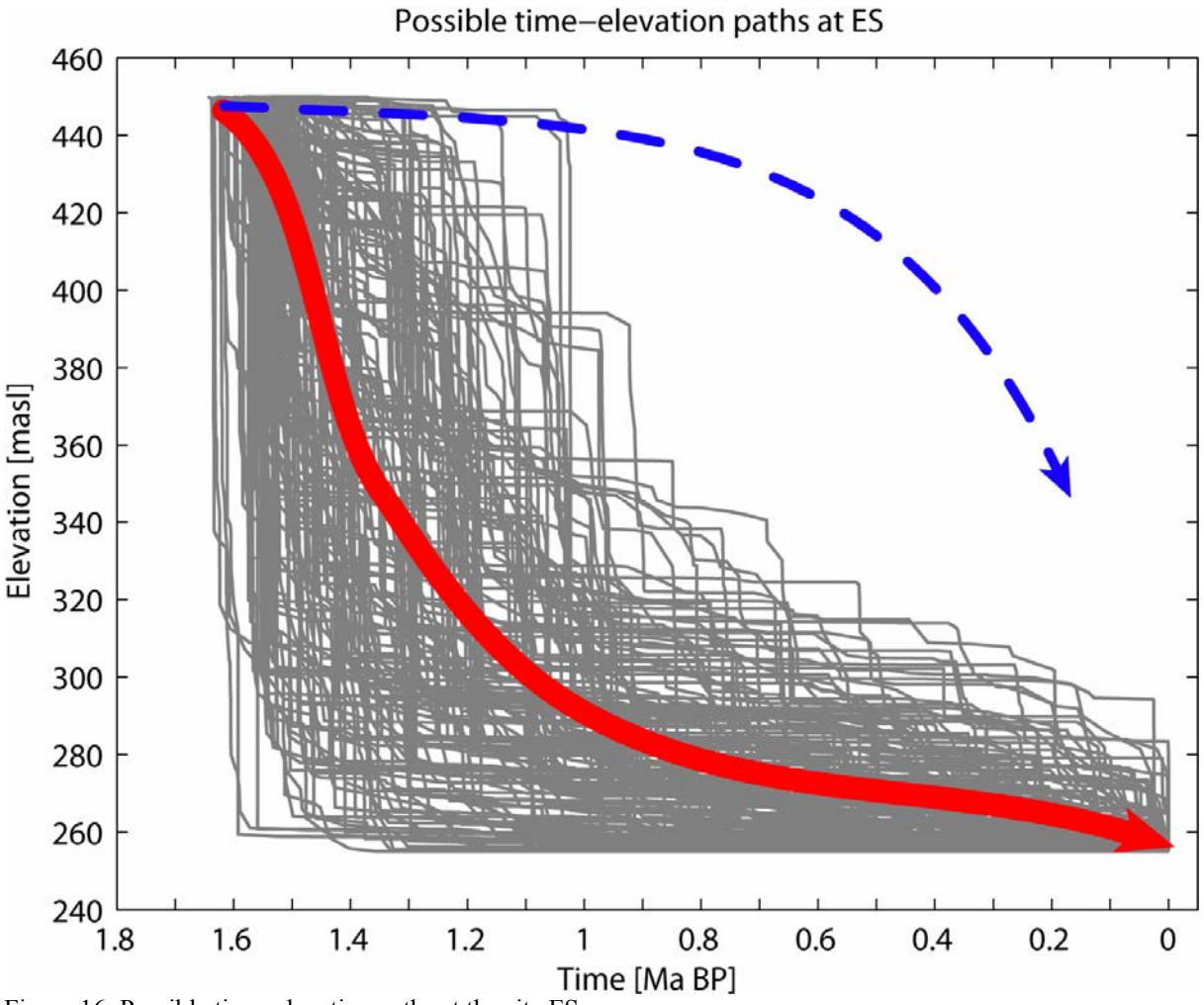

Figure 16: Possible time–elevation paths at the site ES.
Thin grey lines represent random monotonic subsidence paths starting at 1.62 ± 0.09 Ma and 450 masl and ending at 255 masl today, and which reproduced the observed N/P value at ES within the analytical uncertainty. Red thick line represents the average elevation of all valid scenarios at discrete time points. The blue dashed line represents a failed path, whose modeled concentration reached the observed value of N/P too early: the necessary additional exposure will increase the modeled N/P value beyond the analytical uncertainty of the measured N/P ratio at ES.

3.6. Water divide migration at the eastern Meshar basin

Two wind gaps at the eastern part of the Meshar plain (site KK, 0.51 ± 0.06 Ma, Figure 17a; and site KM, 0.25 ± 0.03 Ma, Figure 17b) have yielded anomalously young ages, which are a result of a recent truncation as discussed below. Calcic soils, such as the one observed at site KM (Figure 17c,d), did not form in the hyperarid areas of the Negev during the middle – late Pleistocene (Amit et al., 2006). At sites PS4 and PS6, buried calcic soil horizons (Bk) at depth of ~1 m below surface are associated with model cosmogenic ages of early Pleistocene; salic and gypsic horizons, found above the calcic horizons, reflect middle to late Pleistocene climate (Matmon et al., 2009). It is likely that the calcic soil observed at site KM has been formed in the early Pleistocene as well (upon a conglomerate which was deposited earlier). However, unlike other windgaps, eastern Meshar was subjected to continuous fluvial activity that removed the top of the ancient soils and kept resetting the cosmogenic clock at this area.

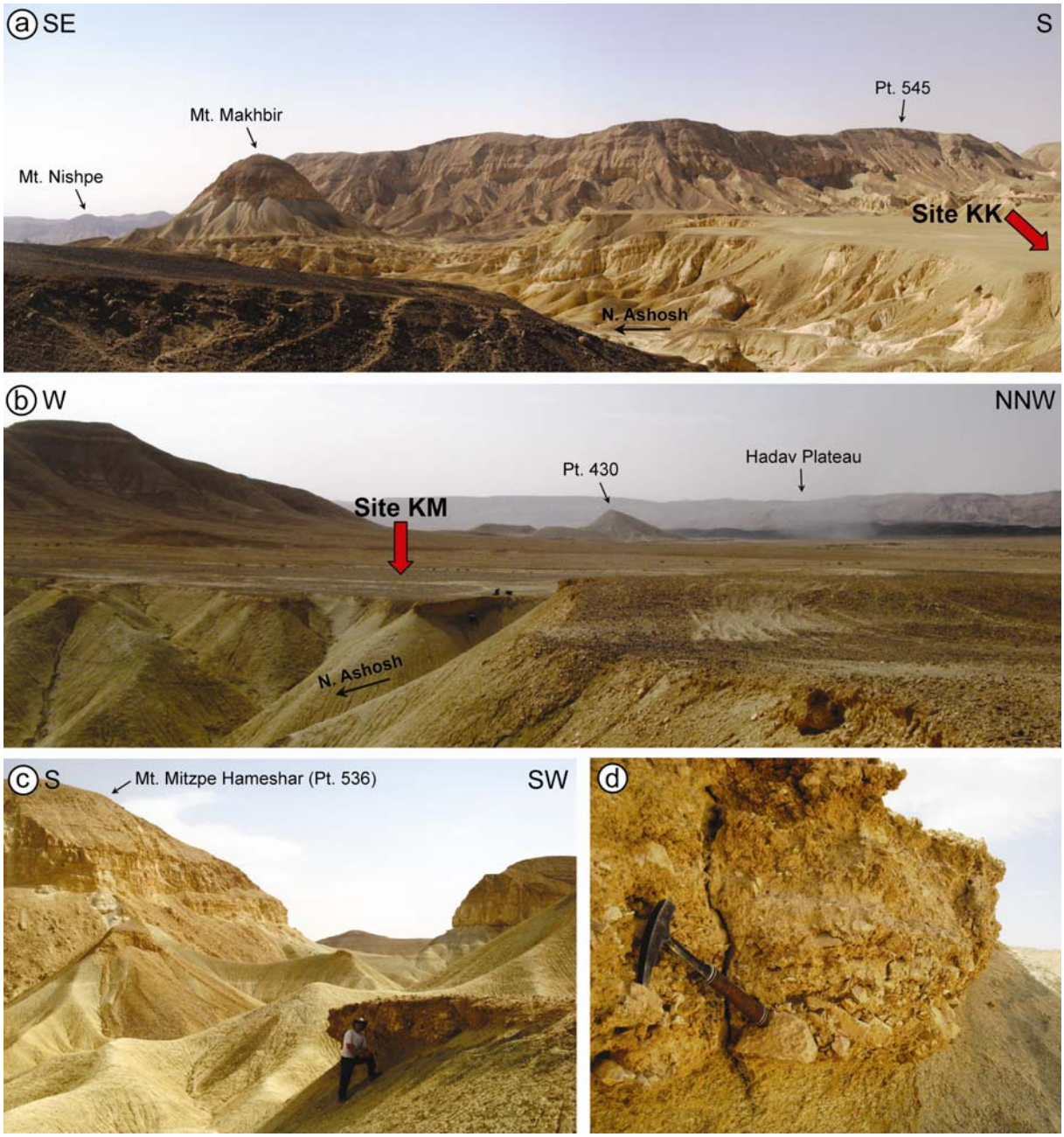

Figure 17: Water divide between the Meshar and Ashosh basins.
a) Site KK (marked with an arrow. Isolated hill on the left is Mt. Makhbir). b) Site KM (marked with an arrow). c-d) site KM: close-up on the buried calcic soil horizon developed in the Arava conglomerate.

Different scenarios are involved in the preservation or destruction of ancient water divides (Figure 18a). As the regional gradients in the vicinity of ancient wind gaps (PS4, PS6, MK, MZ, EZ) were reversed, the new fault-controlled stream network started flowing perpendicular to the paleo-Paran drainage lines, effectively minimizing the runoff from the abandoned surfaces located on water divides (Figure 18b). However, at the eastern part of the Meshar plain, the original westward gradient of the paleo-Paran drainage system has not been cancelled altogether but only diminished; hence, the new stream network flows parallel to the paleo-direction: a weak westward drainage is still present on top of the eastern Meshar plain, while the bordering Ashosh basin flows in an opposite direction to the east (Figure 18c). The

100 m high cliff at the boundary between the two basins undergoes a relatively rapid westward retreat due to the soft bedrock on which the water divide is situated (Paleocene shales of the Taqiye Formation), augmenting the catchment area of the Meshar in favor of the Ashosh basin. Thus, local stagnation of flow at the eastern edge of the plain (due to a diminishing catchment area) is soon followed by cliff collapse and an establishment of a new water divide just to the west of the old one. Observing this active migration of the water divide, it becomes clear that the Meshar plain consists of rejuvenated surfaces, inset below the early Pleistocene datum. The similarity of the abandonment ages at the Meshar watergaps to that of the young inset surface at the central Meshar (site KZ, 0.45 ± 0.05 Ma) supports this explanation from yet another perspective.

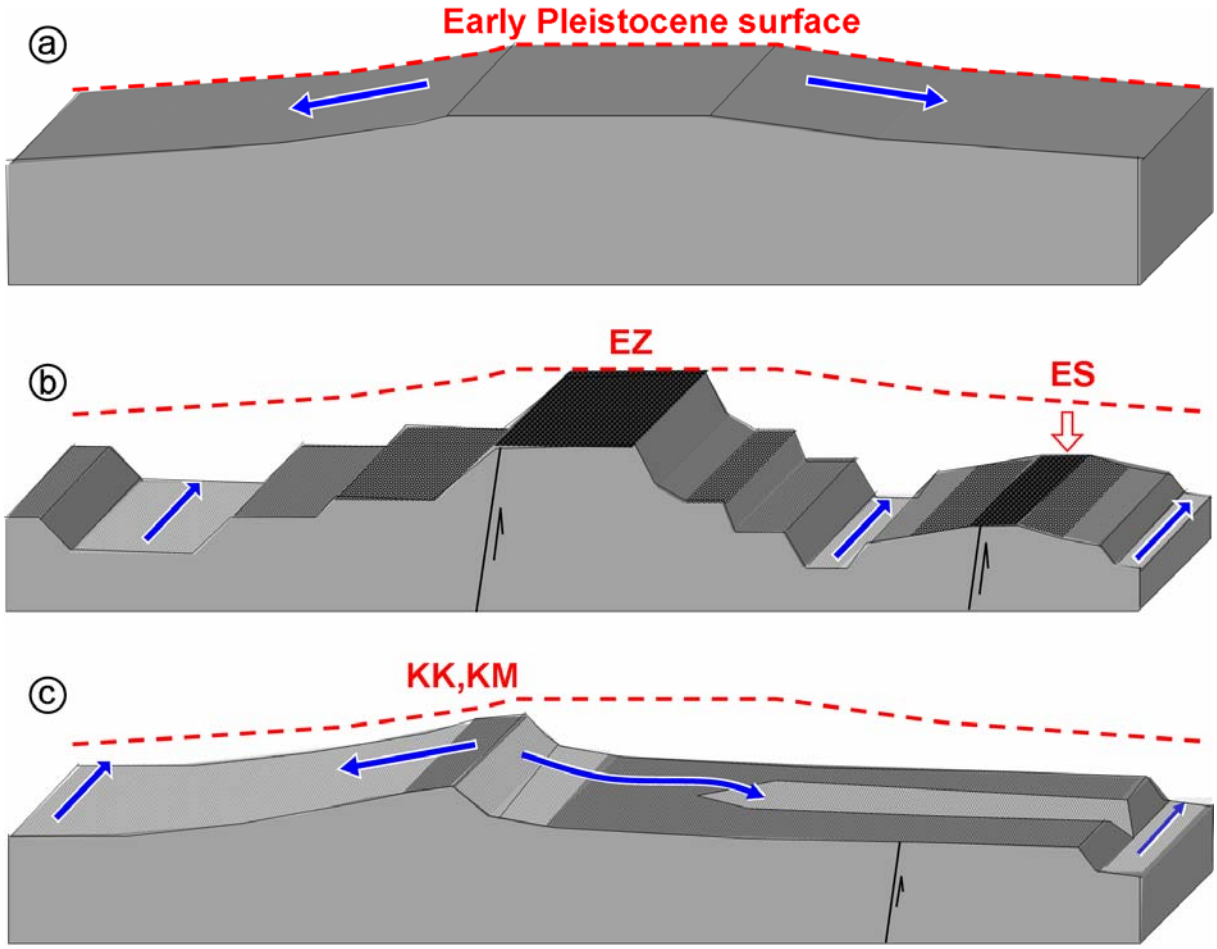

Figure 18: Scenarios for preservation or destruction of surfaces associated with a basin's breakup
a) Emergence of a new water divide and development of desert pavement on the abandoned wind gap. b) A drainage network flowing parallel to the water divide between the basins leads to preservation of the original wind gap surfaces. c) A drainage networks flowing perpendicular to the water divide between the basins leads to constant backward migration of the water divide.

3.7. Summary

The central Negev has a unique setting for investigating fluvial response to long-term tectonic base-level lowering. The paleo-Paran was a Pliocene drainage system that flowed parallel to the incipient Dead Sea rift and also included westward flowing tributaries several tens of km long. Gradual tilting and subsidence towards the east resulted in leveling of the westward-flowing tributaries, and subsequent fragmentation of the paleo-Paran into smaller present-day basins, captured towards the subsiding Arava valley on the east. Zero regional gradients that prevailed during the fluvial reversal stage were accompanied by the accumulation of shallow water deposits and red paleosols, which are currently found on progressively lower elevations towards the rift, and record the amount of Quaternary subsidence.

Extreme hyperaridity conditions leading to negligible erosion rates of resistant clasts, makes desert pavements a unique tool for (i) determination of terrace abandonment ages, and (ii) reconstruction of vertical tectonic movements, by cosmogenic concentration that is a path-integral of the elevation-dependant cosmogenic production rate through time. Reconstruction of vertical tectonic movements attempts to characterize three parameters: (a) the amount of elevation change (b) an absolute age at which the elevation change started, and (c) an elevation-time path. If two out of three parameters are known to a good degree, and a cosmogenic concentration is measured in the tectonically disturbed landform, the third parameter may be estimated or constrained. Most interesting in this sense is the time-elevation path, currently inaccessible to other paleoaltimeters.

Excellent preservation of ancient surfaces on wind gaps along present-day water divides allowed dating the collapse of the paleo-Paran to 1.8 ± 0.2 Ma. One early Pleistocene surface near the backbone of the Arava (site ES) which experienced the greatest Quaternary subsidence (~200 m) is interpreted to contain a cosmogenic signal of elevation change, which occurred at a rate of a few hundreds of m/Ma and probably diminished with time. A continuous record of fluvial incision since ~1.4 Ma within the new basins has been established. However, surfaces older than 0.3 Ma are rare, supporting the observations that rapid tectonic movements in the early and middle Pleistocene did not create the appropriate conditions for sediment storage within the basins, and that fluvial response to the lowered base level of the Dead Sea and the Arava valley was mostly that of incision.

4. Characterization of the middle – late Pleistocene fluvial systems

4.1. Overview of Quaternary deposits in the central Negev

Uplift of the Negev Highlands and progressive subsidence of the Dead Sea basin in the early Pleistocene promoted the collapse of the paleo-Paran basin and shaped the drainage into its present-day pattern (Figure 19); this was discussed and shown in the previous chapter and in Avni et al. (2000) and Ginat et al. (2000).

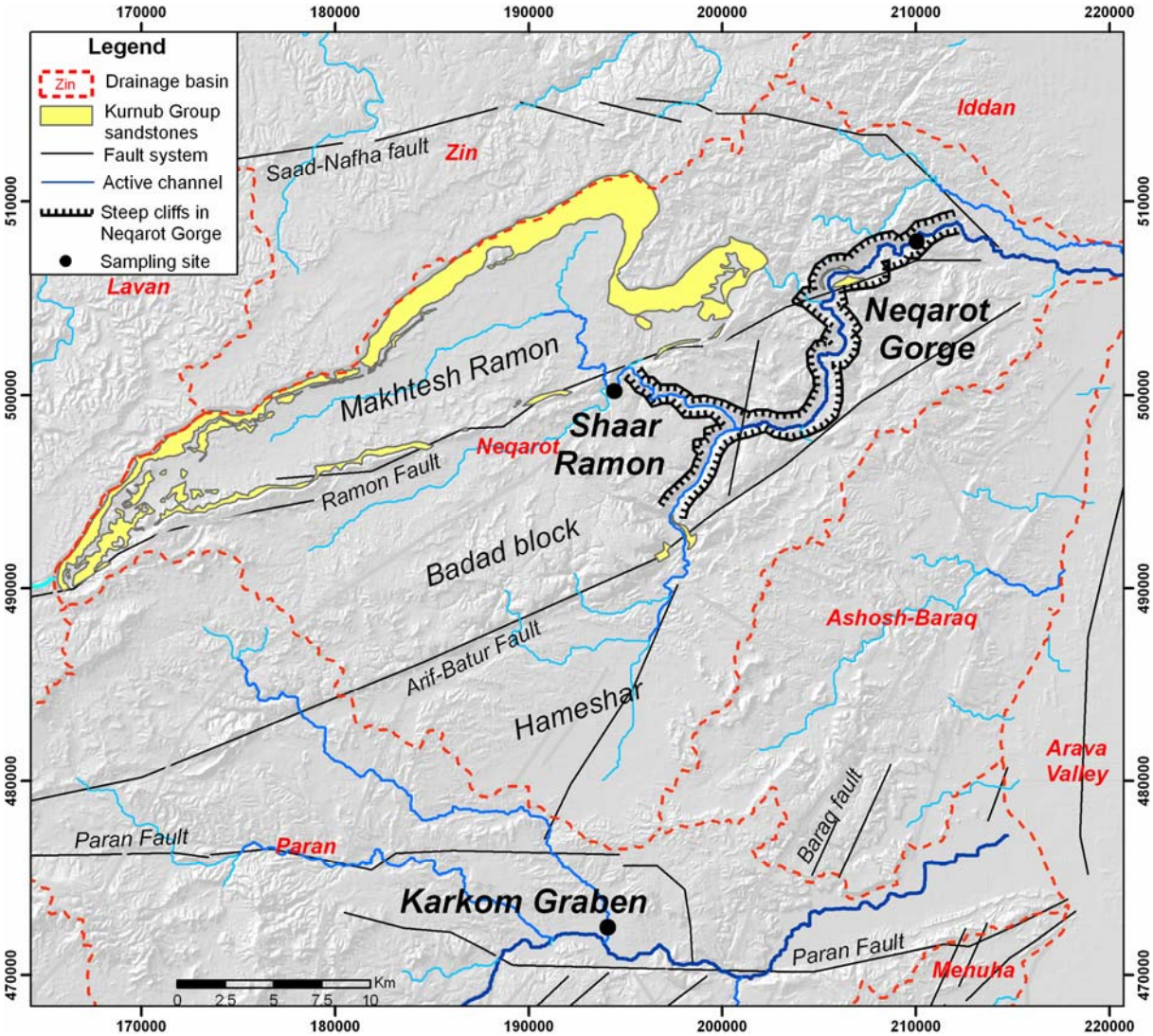

Figure 19: Location map of the late Quaternary sampled terraces.
Sources: Israel DTM grid: Hall, 1993; Avni et al., 2000; Sneh et al., 1998.

Sediment transport within the ephemeral streams of the central Negev is currently sporadic, controlled by short but intense and localized convective storms and flash floods (e.g. Greenbaum et al., 2001). During floods, the depth of the transport layer in most streams is 0.5 – 1.5 m (Amit et al., 2007). The late Quaternary alluvial terraces in the central Negev basins

generally follow the course of present-day streams and are situated at elevations of up to 30 m above the present-day stream beds. They are mostly unaffected by faults and thus were deposited during a period of relative tectonic quiescence (Avni et al., 2000). In regions of wide flood plains, up to four distinct morphostratigraphic surfaces can be identified (Ginat et al., 2000), from the oldest (Q1) to youngest (Q4) terrace. The alluvial sections of the terraces typically comprise of (Avni, 1998): (i) large alluvial clasts (<10 cm), fine material and sporadic coarse input (boulders up to 0.5 m width) of autochthonous origin, consisting of Cretaceous – Eocene carbonates and cherts. (ii) a few allochthonous constituents (e.g., granite, rhyolite and quartz pebbles etc.) reworked from earlier fluviatile sections that transported far-derived materials. A distinct soil chronosequence and surface morphologic change can be distinguished. The rough surface of the lower terraces is characterized by bar and swell morphology, poor sorting of clasts, and a lack of desert pavement. This is in sharp contrast to desert-paved surfaces developed on the topmost terraces, with up to ~80% surface cover (typical size of each desert pavement clast is 4-5 cm). The soil developed on these terraces includes an A_v horizon, a clay-rich and clast-free B horizon with layers of gypsum, and a salt-shattered clast zone beneath (stage E of Amit et al., 1993, 1996). In this work, we combine previous and new OSL data from these terraces with new cosmogenic ages to reconstruct the aggradation and erosion phases that occurred in the central Negev during the late Quaternary. We also analyse the isotopic signature downstream the active channel of the Neqarot Canyon.in order to characterize the present-day sediment transport regime.

4.2. Study sites within the Neqarot and Paran basins

Two major basins in the central Negev, the Paran and Neqarot, were targeted (Figure 19) for a combined cosmogenic and OSL depth profiling of representative terraces. These two basins, which formed a single drainage during the Pliocene, were separated during early Pleistocene (Avni et al., 2000; this study), and subsequently have experienced a separated evolution. The Neqarot basin drains an area of ~1000 km^2 towards the northern Arava valley through the Neqarot Gorge (Figure 19), which is an antecedent drainage course carved during the Pliocene by the paleo-Paran river (Zilberman et al., 1996). The Neqarot drainage basin includes Makhtesh Ramon (the biggest of the four erosion cirques in the Negev; Zilberman, 2000), where Lower Cretaceous sandstone outcrop. These outcrops are the main source of quartz sand in fluvial deposits within the Makhtesh and downstream in the Neqarot Gorge (Figure 19). Within the Neqarot Gorge, strath bedrock surfaces situated 40 – 50 m above present-day channel suggest that they have once formed the riverbed of the gorge. However, alluvial material is preserved up to 20 m above current river bed. Two distinct alluvial

terraces at +7 m ($Q2_N$) and the other at +2 m ($Q3_N$) above the river bed are apparent on both banks of the present channel (Figures 20–22).

The Paran basin is the largest drainage system in the Negev, draining an area of ~4000 km^2 towards the central Arava valley through the Karkom Graben (Figure 19), a Miocene structure enclosed between two segments of the Paran fault (Calvo and Bartov, 2001). A uniquely continuous Neogene section is preserved within the graben, reflecting all the major stages of the fluvial evolution of the Negev (Figure 23). The late Quaternary terraces are deposited up to 20 m above the current Paran channel, and ~130 m below the Miocene – early Pleistocene sections, which had been eroded during early and middle Pleistocene. Three distinct terraces along the Paran stream within the Karkom Graben were previously dated by OSL to ~300 ka ($Q1_P$), ~100 ka ($Q2_P$) and ~10 ka ($Q3_P$) (Avni et al., 2000b; Figure 23).

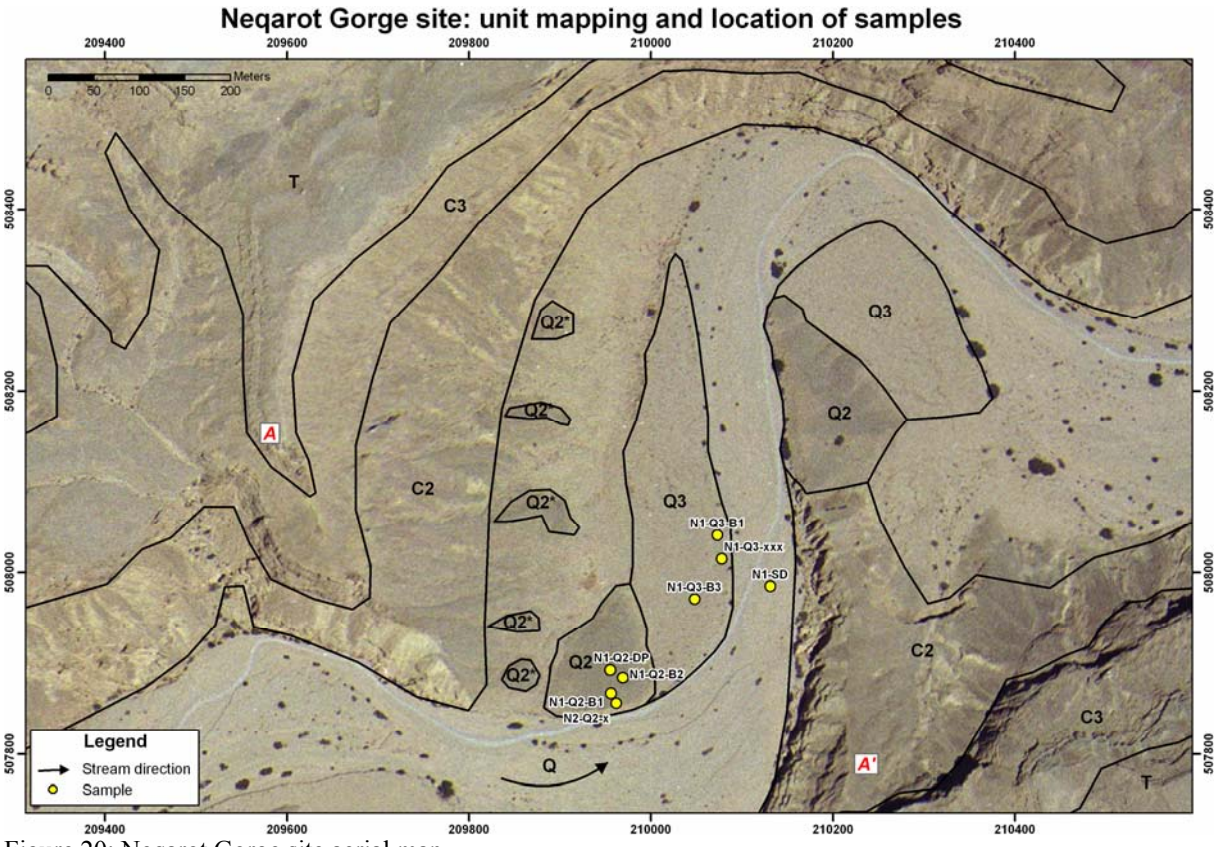

Figure 20: Neqarot Gorge site aerial map.
Formation legend: C2 – Zafit, En Yorqeam and Avnon formations (Cenomanian). C3 – Tamar Formation (Cenomanian). T – Derorim, Shivta and Nezer formations (Turonian). Q2, Q3 – Alluvial terraces. Q2* - Talus associated with Q2. Q – Active channel. (Modified from Sneh et al., 1998) A-A'- cross section shown in Figure 22.

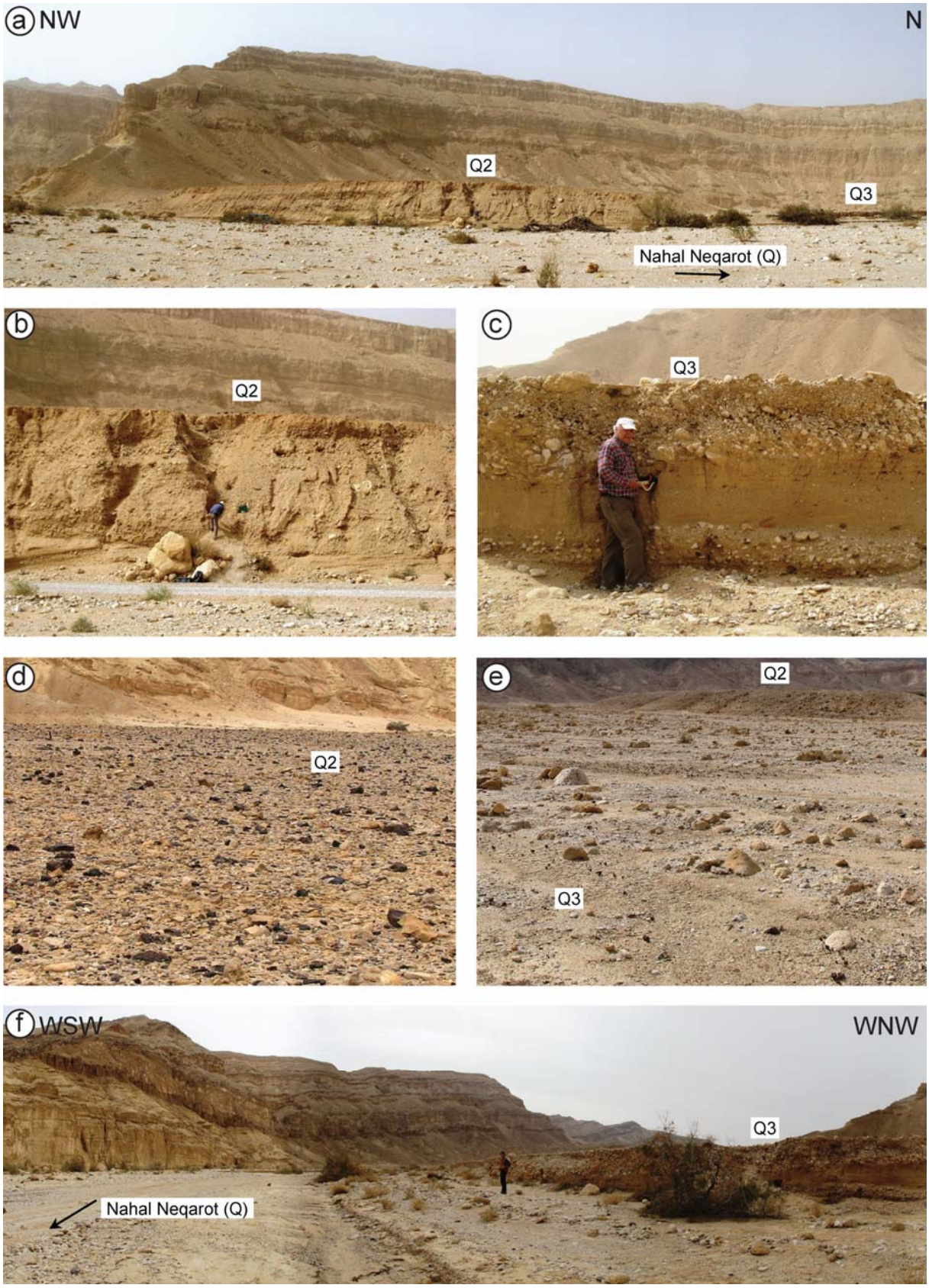

Figure 21: Photographs at the Neqarot Gorge site.
a) General outlook on field relations of bedrock, $Q2_N$, $Q3_N$ and Q (the present-day active channel) b,c) the alluvial sections of $Q2_N$ and $Q3_N$; d,e) The surficial properties of $Q2_N$ and $Q3_N$; f) The location of the active channel transect and its proximity to the $Q3_N$ section.

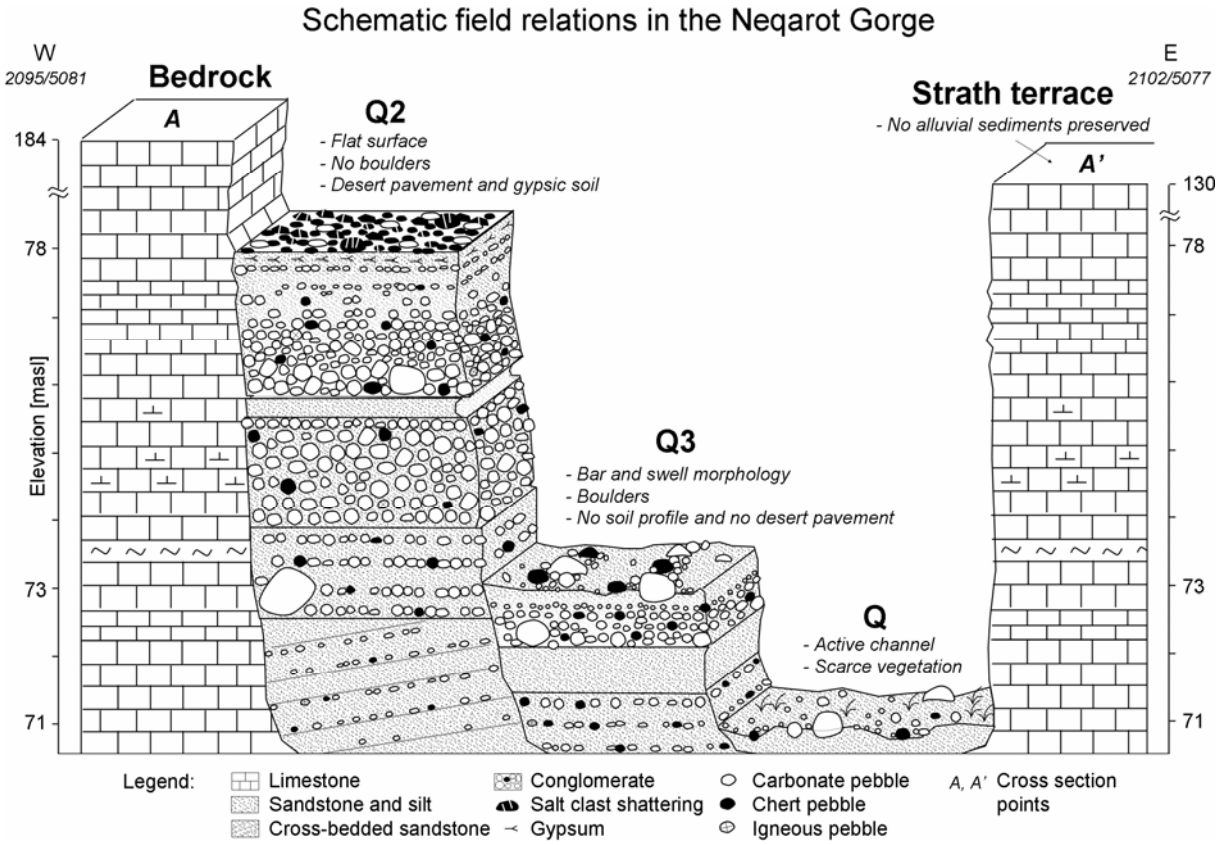

Figure 22: Schematic cross section, field relations at the Neqarot Gorge site.
DP – desert pavement.

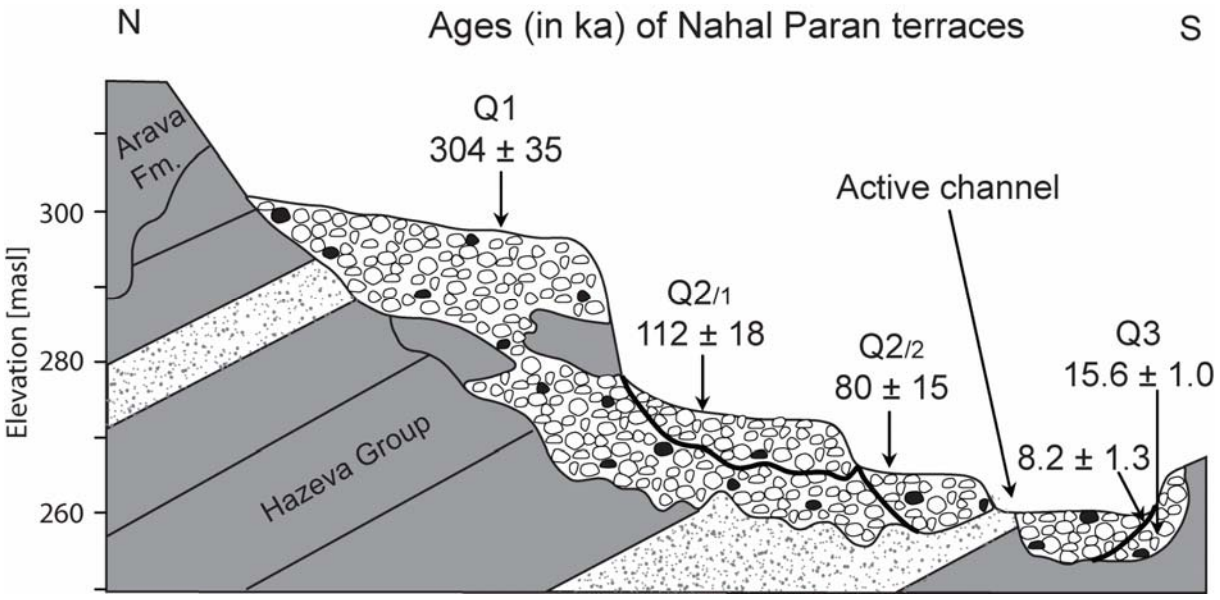

Figure 23: Schematic cross section, field relations and OSL ages at the Karkom Graben site (see Figure 19).
(from Naomi Porat, pers. comm., used with permission)
Sections of the Miocene Hazeva Group [1.5 km of which the upper 1 km is probably syntectonic (Calvo and Bartov, 2001)] represent a northwestward regional drainage, while the sections of the Pliocene Arava Formation (~150 m) deposited unconformably on top of Hazeva Group represent the paleo-Paran stream, which flowed across the Karkom Graben through the Neqarot Gorge towards the Dead Sea. All late Pleistocene terraces were deposited within the boundaries of the present active system.

4.3. Methods

Cosmogenic isotopes

Cosmogenic concentrations measured in actively transported sediment are used to understand and characterize present-day drainages, and aid in constraining the initial conditions and ages of sediment in abandoned terraces. Moreover, an assumption of a basin-wide isotopic steady-state may be made if the cosmogenic concentrations do not decrease downstream, allowing to interpret the concentrations in terms of sediment transport times and averaged basin-wide erosion rates (Brown et al., 1995; Bierman and Steig, 1996; Granger et al., 1996).

During deposition of alluvial material, a cosmogenic profile in the sediment will develop (Lal and Arnold, 1985; Phillips et al., 1998), in which the concentration (N) of a cosmogenic radionuclide at any depth (x) is invariant of time. Various factors which control the cosmogenic concentration profile in the aggrading alluvial section include (i) depth below surface (x), (ii) the production rate of cosmogenic nuclides at the surface ($P(0)$), (iii) sediment density (ρ), (iv) vertical deposition rate (s, in [cm y^{-1}]), and (v) the initial cosmogenic concentration in the newly arriving sediment (N_{inh}):

$$N(x) = N_{inh}\exp(-\lambda x/s) + \frac{P(0)\exp(-\rho x/\Lambda)}{\lambda - \rho s/\Lambda}\left(1-\exp\left((-\lambda/s+\rho/\Lambda)x\right)\right) \qquad (5)$$

where λ is the nuclide's decay constant, and Λ is the attenuation length of cosmic rays (~150 g cm^{-2}; Gosse and Phillips, 2001).

In contrast, when a surface is abandoned, a different, "exposure" profile is developed (Lal, 1991; Phillips et al., 1998). This profile depends on the time of exposure and on the rate of surface exhumation, enabling surface exposure dating (until the concentrations reach their steady-state equilibrium values after 3-4 half-lives of the targeted nuclide; Faure and Mensing, 2005). Under conditions of constant exposure, the cosmogenic concentration profile in the alluvial section is a function of: (i) depth below surface (x), (ii) exposure time (t), (iii) the production rate at the surface ($P(0)$), (iv) sediment density (ρ), (v) vertical erosion rate (ε, in [cm y^{-1}]), and (vi) the initial cosmogenic concentration at a layer which is now at depth x ($N(x,0)$):

$$N(x,t) = N(x,0)\exp\left(-\lambda t\right) + \frac{P(0)\exp\left(-\rho x/\Lambda\right)}{\lambda+\rho\varepsilon/\Lambda}\left(1-\exp\left(-(\lambda+\rho\varepsilon/\Lambda)t\right)\right) \qquad (6)$$

A convenient reference age, known as "simple exposure age", may be calculated for an observed concentration (N_{obs}) sampled at depth x and with a known sediment density ρ.

Assuming that the surface production rate $P(0)$ and the attenuation length Λ have not changed during the irradiation time (t), and considering the effects of inheritance and erosion as negligible $(N(x,0) \equiv 0, \varepsilon \equiv 0)$, we can rearrange Equation (6):

$$t(N_{\text{obs}}(x), x, \rho) = -\frac{1}{\lambda} \cdot \ln\left(1 - \frac{N_{\text{obs}}\lambda}{P(0)\exp\left(-\rho x / \Lambda\right)}\right) \tag{7}$$

where $N_{\text{obs}}(x)$ is the observed concentration at depth x.

Glacially striated rocks (Nishiizumi et al., 1989) and desert pavements (McFadden et al., 1987; Wells et al., 1995) contain independent evidence of near zero erosion and continuous exposure to cosmic radiation since abandonment, and thus may be adequately dated by Equation (7). However, with increasing depth below the surface, the importance of the in-situ produced cosmogenic isotopes decreases relative to their initial concentration, making the assumption of $N(x,0) \equiv 0$ invalid. For alluvial surfaces which were first aggraded and then abandoned, we can resolve the "inheritance problem" by combining Equations (5) and (6):

$$\begin{aligned} N_{\text{mod}}(x) = &\left[N_{inh}\exp(-\lambda x / s) + \frac{P(0)\exp(-\rho x / \Lambda)}{\lambda - \rho s / \Lambda}\left(1 - \exp\left((-\lambda / s + \rho / \Lambda)x\right)\right)\right] \\ &\times \exp\left(-\lambda t\right) + \frac{P(0)\exp\left(-\rho x / \Lambda\right)}{\lambda + \rho\varepsilon / \Lambda}\left(1 - \exp\left(-(\lambda + \rho\varepsilon / \Lambda)t\right)\right) \end{aligned} \tag{8}$$

where $N_{\text{mod}}(x)$ is the modeled concentration for a sample collected from depth x, based on the unknowns N_{inh}, s, ε, and t. Since in Equation (8), the effects of ε and t are interchangeable (i.e., the same profile may be produced by long exposure at slow erosion rate, and by short exposure with fast surface denudation), an independent control on one of these parameters must be obtained.

The soils which develop on top of abandoned terraces are a product of slow dust accumulation and pedogenesis rather than profile erosion (Amit and Gerson, 1986; Amit et al., 1993; Matmon et al., 2009). We can therefore neglect the erosion ($\varepsilon \equiv 0$) and simultaneously apply Equation (8) to all the available depth samples, looking for a unique combination of N_{inh}, s and t which minimizes the difference between modeled and measured concentrations at all depths (e.g., Anderson et al., 1996; Nichols et al., 2002, 2005). When the best-fit values of N_{inh}, s and t are obtained, the model age of deposition of each sample may be calculated:

$$t_{\text{dep}}(x) = x / s + t \tag{9}$$

i.e., the sum of the individual periods it took each strata to reach its depth (x/s) plus the subsequent exposure time (t) as similarly experienced by all strata.

This best-fit cosmogenic "model deposition age" (*profileage.m*, see Appendix 8.4) can be easily compared to the deposition age of an OSL sample acquired from the same depth. The initial cosmogenic inheritance of deposited material plays an important role in understanding the fluvial behavior and basin-wide erosion rates in the past (Bierman and Steig, 1996). For a measured cosmogenic profile in sediment, the inheritance (N_{inh}) may be estimated by solving Equation (8) for all depths. When only one cosmogenic sample is measured and an independent age t_{OSL} is given, the cosmogenic inheritance may be attributed to the "excess" cosmogenic exposure age (if such exists), by re-arranging Equation (6) to calculate $N(x,0)$:

$$N(x,0)=\left[N(x,t)-\frac{P(0)\exp\left(-\rho x/\Lambda\right)}{\lambda+\rho\varepsilon/\Lambda}\left(1-\exp\left(-(\lambda+\rho\varepsilon/\Lambda)t_{\mathrm{OSL}}\right)\right)\right]\cdot\exp\left(\lambda t_{\mathrm{OSL}}\right) \quad (10)$$

This inheritance $N(x,0)$ may be then used to infer a basin-wide paleo-erosion rate:

$$\varepsilon=\Lambda/\rho\cdot\left(\overline{P}/N(x,0)-\lambda\right) \quad (11)$$

where $\overline{P}$ is the past basin-averaged production rate (*inheritance.m*, see Appendix 8.4).

Field and lab work

Three samples of active channel sediment were collected above and below the confluence of the Ramon and Neqarot streams. A fourth active channel sediment sample was collected 30 km downstream in the Neqarot Gorge, nearby the $Q2_N$ terrace. All sites have a similar 20 – 30 m wide channels, an average slope of 0.01, and surficial sand-sized sediment. At each site, sandstone was sampled perpendicular to the stream direction at ~0.5 m intervals across the entire stream and amalgamated into a single sample. Cosmogenic depth profiles of Q3N and Q2N at the Neqarot gorge were sampled from cleaned terrace walls, scraped back about 0.5 m ($Q3_N$) and 2 m (utilizing a modern gully in $Q2_N$; see Figure 21b). Additionally, 2 quartzite boulders were collected from each terrace. Desert pavement was sampled at the top surfaces of $Q2_N$, $Q2_P$ and $Q1_P$ by collecting and amalgamating hundreds of chert clasts (while 25 – 40 clasts are sufficient to achieve a representative mean concentration in a geomorphic system; Repka et al., 1997). Three depth samples from each of $Q3_N$ and $Q2_N$ terraces were also sampled for OSL dating (total of 6 samples).

4.4. Ages of terrace deposition and paleo-erosion rates

The ^{10}Be concentrations measured in the active channel sediment of the Neqarot Gorge decrease downstream (Table 3). Their values change from (3.06 ± 0.18) × 10^5 atoms g^{-1} SiO_2 at "Shaar Ramon" to (1.13 ± 0.06) × 10^5 atoms g^{-1} SiO_2 at the lower "Neqarot Gorge" site (Table 3 and Figure 24). Although these samples represent the active channel and therefore are supposedly "ageless", their inheritance is equivalent to "simple exposure age" that ranges between 62 ± 7 ka (N4-N) and 29 ± 3 ka (N1-SD; Table 3).

In the Neqarot Gorge site, concentrations of four depth samples in the $Q2_N$ terrace range from (1.33 ± 0.10) × 10^5 atoms g^{-1} SiO_2 at a depth of 5.31 m below surface, and up to (3.61 ± 0.11) × 10^5 atoms g^{-1} SiO_2 at a depth of 0.63 m (Table 3 and Figure 25a). These concentrations correspond to model deposition ages (Equation 8) of 216 ± 21 ka and 182 ± 11 ka for the base and top of the $Q2_N$ terrace, respectively, and a model inheritance of 1.27 ± 0.09 × 10^5 atoms g^{-1} SiO_2. The OSL ages (Table 4) obtained from the same depths (206 ± 19 ka and 199 ± 27 ka for the base and top, respectively), are in excellent agreement with cosmogenic deposition ages. The cosmogenic concentration of the desert pavement above the surface is (10.67 ± 0.34) × 10^5 atoms g^{-1} SiO_2 (simple exposure age of 288 ± 32 ka), and that of the boulders ranges from (10.67 ± 0.34) to (19.52 ± 0.86) × 10^5 atoms g^{-1} SiO_2, corresponding to simple exposure ages of 294 ± 33 ka and 576 ± 73 ka, respectively.

Seven depth samples in the $Q3_N$ terrace yielded ^{10}Be concentrations nearly independent of sample depth, with a mean value of (1.14 ± 0.16) × 10^5 atoms g^{-1} SiO_2 throughout the section (Table 3 and Figure 25b). Corresponding model ages of 8.2 ± 3.9 ka and 2.5 ± 1.5 ka for the exposed base and top of the $Q3_N$ terrace were calculated, and a model inheritance of 1.07 ± 0.04 × 10^5 atoms g^{-1} SiO_2 was estimated. The OSL ages (Table 4) for the base and top of the Q3 section are 11.0 ± 4.9 ka and 10.9 ± 4.4 ka, respectively. The ^{10}Be concentrations of two boulders at the top surface of the terrace range from (3.35 ± 0.12) to (6.35 ± 0.18) × 10^5 atoms g^{-1} SiO_2, corresponding to simple exposure ages of 88 ± 10 ka and 170 ± 19 ka, respectively.

The ^{10}Be concentrations of desert pavements sampled on top of terraces in the Karkom Graben are 18.53 ± 0.43 × 10^5 atoms g^{-1} SiO_2 for the $Q1_P$ terrace (simple exposure age of 346 ± 39 ka, corresponding to an unpublished [Naomi Porat, pers. comm., 2008] OSL age of 304 ± 35), and 15.04 ± 0.36 × 10^5 atoms g^{-1} SiO_2 for the $Q2_P$ terrace (simple exposure age of 440 ± 51 ka, corresponding to an unpublished [Naomi Porat, pers. comm., 2008] OSL age 125 ± 16 ka).

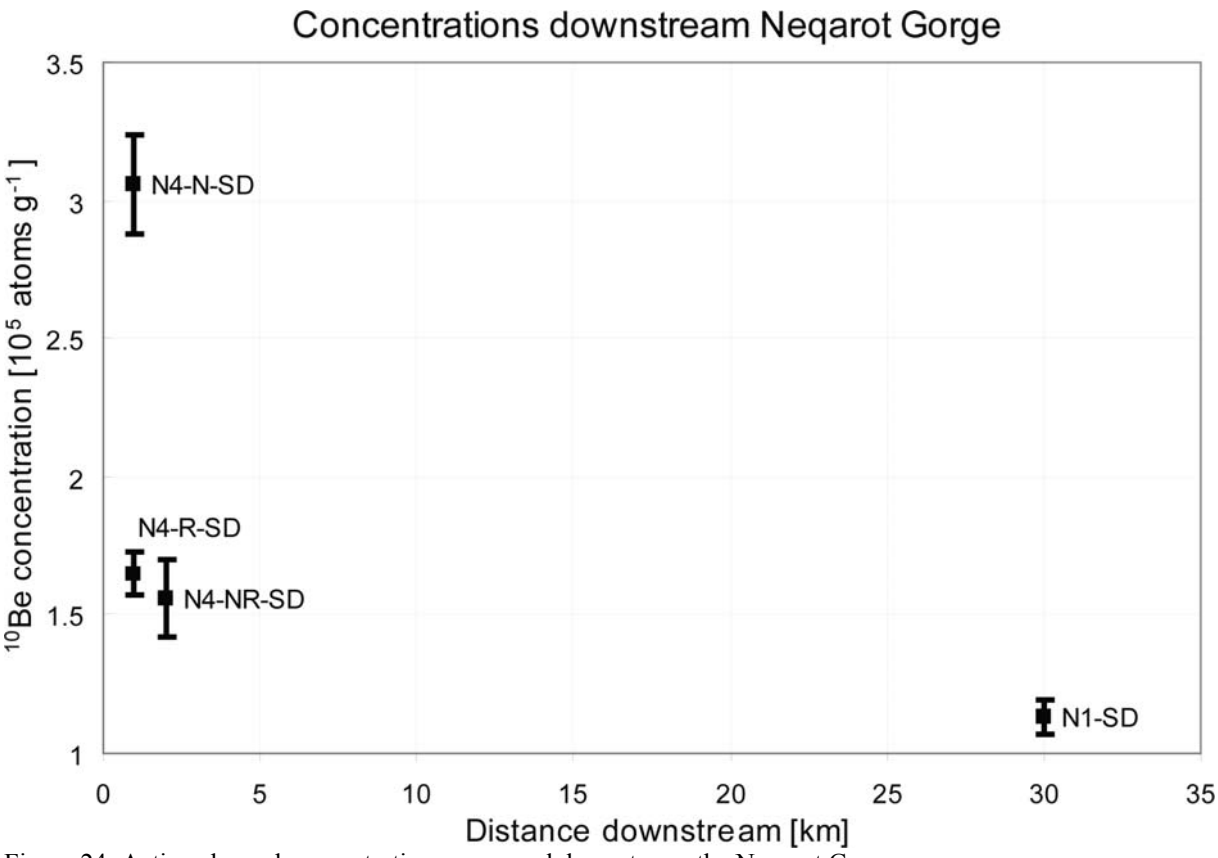

Figure 24: Active channel concentrations measured downstream the Neqarot Gorge.

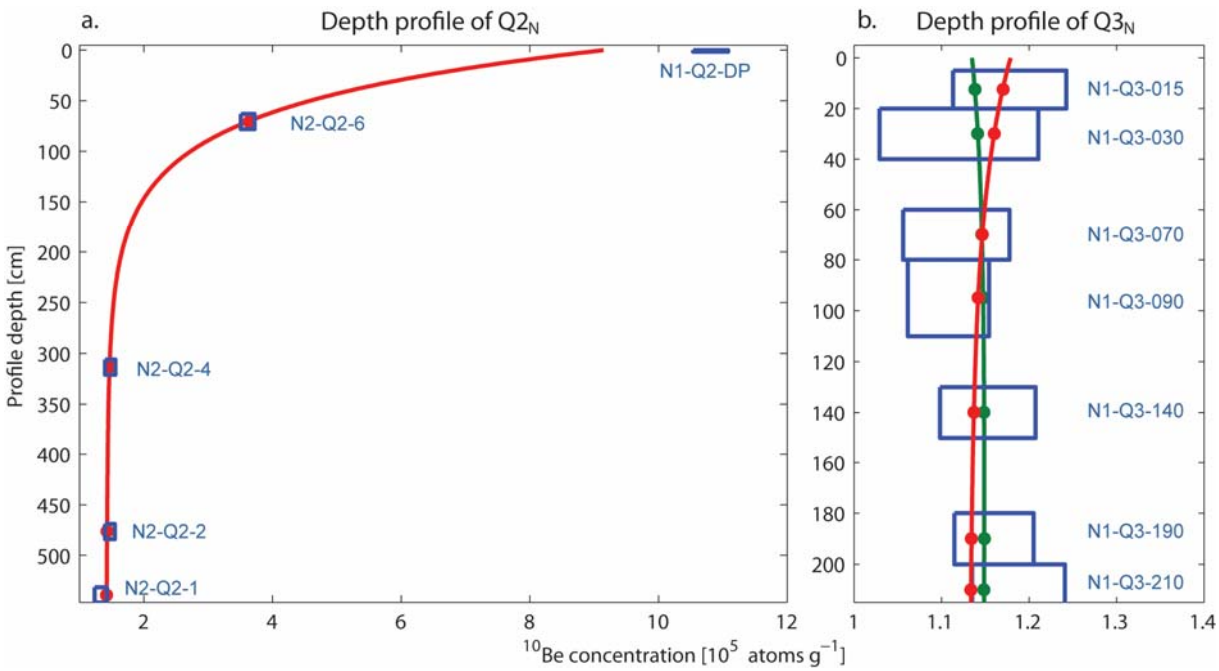

Figure 25: Cosmogenic depth profiles of Q2 and Q3 terraces at the Neqarot Gorge site.
Blue squares represent samples' depth and concentrations (each within its 1σ uncertainty). Continuous curves with dots represent modeled concentration profile for a) deposition at rate of 200 m/ma followed by exposure period of 200 ka. b) red line: deposition at 600 m/Ma followed by 2 ka exposure; green line: deposition at 200 m/Ma followed by 2 ka exposure.

Table 3: Site locations, CN concentrations, OSL ages, and CN exposure and model ages.

Sample Name	Sample type	Location Lat / Lon	Elev. [m asl]	Depth [m]	^{10}Be [10^5 atoms g^{-1}]	Exp [1] age [ka]	Dep [2] age [ka]	OSL Age [ka]
Neqarot active channel								
N4-N-SD	sediment	30°35.246' / 34°56.288'	405		3.06 ± 0.18	62 ± 7		
N4-R-SD	sediment	30°35.992' / 34°56.249'	390		1.65 ± 0.08	33 ± 4		
N4-NR-SD	sediment	30°35.471' / 34°56.571'	380		1.56 ± 0.14	33 ± 4		
N1-SD	sediment	30°39.706' / 35°06.413'	70		1.13 ± 0.06	29 ± 3		
Neqarot gorge, Q3 terrace								
N1-Q3-B1	boulder	30°39.736' / 35°06.351'	73		6.35 ± 0.18	170 ± 19		
N1-Q3-B3	boulder	30°39.698' / 35°06.335'	73		3.35 ± 0.12	88 ± 10		
N1-Q3-015	depth	30°39.722' / 35°06.354'	73	0.05	1.18 ± 0.06		2.5 ± 1.5	10.9 ± 4.4
N1-Q3-030	depth	30°39.722' / 35°06.354'	73	0.20	1.12 ± 0.09		2.9 ± 1.6	
N1-Q3-070	depth	30°39.722' / 35°06.354'	73	0.60	1.12 ± 0.06		4.1 ± 1.9	
N1-Q3-090	depth	30°39.722' / 35°06.354'	73	0.80	1.11 ± 0.05		4.7 ± 2.1	12.6 ± 3.1
N1-Q3-140	depth	30°39.722' / 35°06.354'	73	1.30	1.15 ± 0.05		6.1 ± 2.8	
N1-Q3-190	depth	30°39.722' / 35°06.354'	73	1.80	1.16 ± 0.05		7.6 ± 3.6	
N1-Q3-210	depth	30°39.722' / 35°06.354'	73	2.00	1.19 ± 0.05		8.2 ± 3.9	11.0 ± 4.9
Neqarot gorge, Q2 terrace								
N1-Q2-B1	boulder	30°39.642' / 35°06.278'	78		10.67 ± 0.34	294 ± 33		
N1-Q2-B2	boulder	30°39.651' / 35°06.286'	78		19.52 ± 0.86	576 ± 73		
N1-Q2-DP	Des. pav.	30°39.656' / 35°06.277'	78		10.81 ± 0.27	288 ± 32		
N2-Q2-6	depth	30°39.636' / 35°06.281'	78	0.83	3.61 ± 0.11		182 ± 11	199 ± 27
N2-Q2-4	depth	30°39.636' / 35°06.281'	78	3.06	1.48 ± 0.08		199 ± 15	231 ± 17
N2-Q2-2	depth	30°39.636' / 35°06.281'	78	4.69	1.47 ± 0.08		212 ± 19	
N2-Q2-1	depth	30°39.636' / 35°06.281'	78	5.31	1.33 ± 0.10		216 ± 21	206 ± 19
Karkom Graben, Q2 and Q1 terraces								
P1-Q2-DP	Des. pav.	30°20.456' / 34°55.898'	273		18.53 ± 0.43	440 ± 51		125 ± 16 *
P1-Q1-DPS	Des. pav.	30°20.527' / 34°56.800'	284		15.04 ± 0.36	346 ± 39		304 ± 35 *

Note: A ^{10}Be half-life of 1.36 ± 0.07 Ma (Nishizumi et al., 2007), Sea Level High Latitude (SLHL) production rate of 4.58 ^{10}Be atoms g^{-1} SiO_2, attenuation length of 150 ± 4 g cm^{-2}, sediment density of 1.8 g cm^{-3} and latitude-altitude scaling factors of Stone (2000) were used for all age calculations. Age uncertainties include analytical error and an additional 10% uncertainty in reference production rate and scaling factors (Lal, 1991).
[1] "Simple" exposure age, assuming zero inheritance, erosion and uplift.
[2] Deposition model age calculated using Equations (8) and (9).
* Previously unpublished data

Table 4: Optically Stimulated Luminiscence results.

OSL ID	Sample ID	Depth [m]	Grain Size [µm]	γ +cosm. [Gy/a]	K [%]	U [ppm]	Th [ppm]	Ext. [Gy/a]	Total Dose [Gy/a]	No. of Discs	De [Gy]	Age [ka]
NQR-1	N1-Q3-015	0.15	125-177	367	0.1	1.9	0.7	328	669 ± 42	18/23	7.6 ± 3.1	10.9 ± 4.4
NQR-2	N1-Q3-090	1.05	88-125	400	0.09	1.3	1.1	239	664 ± 45	14/24	8.4 ± 2.0	12.6 ± 3.1
NQR-3	N1-Q3-210	2.05	88-125	414	0.07	1.5	0.4	254	673 ± 47	19/24	7.4 ± 3.2	11.0 ± 4.9
NQR-6	N2-Q2-6	0.83	88-125	331	0.11	2.2	0.7	380	718 ± 40	11/12	143 ± 18	199 ± 27
NQR-5	N2-Q2-4	3.05	88-125	365	0.09	1.5	0.7	275	643 ± 42	7/12	149 ± 5	231 ± 17
NQR-4	N2-Q2-1	5.30	88-125	358	0.12	1.1	0.5	239	601 ± 42	7/12	123 ± 7	206 ± 19

Note: all analyses were carried out on quartz grains which were etched in concentrated HF for 40 minutes. Equivalent doses (De) were determined using the standard Single Aliquot Regenerative dose (SAR) protocol (Murray and Wintle, 2000), using preheats of 10 s at 220–260 °C. Samples had recycling ratios mostly within 10% of 1.0 and negligible IR signals. No. of discs – the number of measurements (out of all repeated measurements) used for calculation of the equivalent dose (De) used in age calculation. Annual γ and cosmic dose rates were measured in the field using a portable gamma scintillator. Dose rates of α and β radiation were calculated from the concentrations of the radio-elements U, Th, and K in the sediment, measured by ICP-MS and ICP-AES. Water content was estimated at 1%.

The initial inheritance of chert and sand in the alluvial terraces was approximated using different estimates, including (i) "excess" cosmogenic age of desert pavement (relative to OSL age; Equation 10), (ii) depth profile best-fits (Equation 8), or (iii) treating the measured concentration in the present-day active channel as the representative inheritance (N4-N-SD, N4-NR-SD). Based on these inheritance values, basin-wide erosion rates (Table 5) were estimated using Equation 11. The apparent erosion rate of sandstone range from 16 ± 2 m/Ma to 21 ± 2 m/Ma, inferred from current active channel and from the $Q3_N$ terrace, respectively (Table 5). The apparent erosion rate of chert has a wide variance, ranging from 13 ± 16 m/Ma to 1.6 ± 0.2 m/Ma inferred from $Q1_P$ terrace and $Q2_P$ terrace, respectively, and shows a trend of a diminishing erosion rate with time.

Table 5: Calculated inheritance and basin-wide erosion rates for late Quaternary terraces

Terrace	sample	OSL age [ka BP]	material	erosion rate [m/Ma]	method of estimation
$Q1_P$	P1-Q1-DP	304 ± 35	DP chert	13 ± 16	"excess" cosmo age
$Q2_N$	N1-Q2-DP	212 ± 38	DP chert	7 ± 4	"excess" cosmo age
$Q2_N$	N1-Q2-x	212 ± 38	alluvial sand	17 ± 2	profile best-fit
$Q2_P$	P1-Q2-DP	125 ± 16	DP chert	1.6 ± 0.2	"excess" cosmo age
$Q3_N$	N1-Q3-xxx	12 ± 8	alluvial sand	21 ± 2	profile best-fit
Q	N4-R, N4-NR	0 ± 0	alluvial sand	16 ± 2	measured concentration

Note: A ^{10}Be half-life of 1.36 ± 0.07 Ma (Nishizumi et al., 2007), Sea Level High Latitude (SLHL) production rate of 4.58 ^{10}Be atoms g^{-1} SiO_2, attenuation length of 150 ± 4 g cm^{-2}, bedrock density of 2.7 g cm^{-3} and latitude-altitude scaling factors of Stone (2000) were used in calculations. Uncertainties in concentration, ^{10}Be half-life, OSL age and a 10% in reference cosmogenic production rate and scaling factors (Lal, 1991) were propagated in all calculations. Basin-wide production rate was assumed to be equal to the production rate at each site, leading to a possible systematic underestimation of erosion rates of <20%. Method of estimation is the means by which the inheritance was calculated (see text)

4.5. Discussion

Terrace ages

Cosmogenic model deposition ages of terraces $Q2_N$ and $Q3_N$ in the Neqarot Gorge are generally in good agreement with OSL ages sampled exactly from the same horizons (Table 4). In the ~200-ka old $Q2_N$, the age probability distributions derived by the two methods significantly overlap and thus support each other. In the ~10-ka old $Q3_N$, the cosmogenic model ages of the two upper layers (N1-Q3-090 and N1-Q3-015) are by several ka younger than the OSL matching sample. This discrepancy arises from the poor age constraint for a straight concentration profile, which could be equally created by instantaneous deposition of the 2 m section (~600 m/Ma; Figure 25b, red line), or by a slower deposition of the same section (~200 m/Ma; Figure 25b, green line) both followed by a short exposure period of ~2 ka. This small age difference of only a few ka between OSL and cosmogenic profile in $Q3_N$

can be reconciled in two ways: (i) the high noise of the OSL signal (25%-45%) indicates insufficient exposure ("bleaching") of some sand grains to sunlight before their deposition; the "older" grains could have originated from the nearby $Q2_N$ terrace, whose bank could have been eroded by a flood, providing sediment for the accumulating terrace immediately downstream. (ii) The original height of $Q3_N$ terrace was ~2 m above the present terrace head; this supposedly "absent" profile, which could have had a 10-ka cosmogenic profile developed, was only recently (~2 ka) truncated by a flood, exposing the deeper and "straight" component of the cosmogenic profile to the surface. In either scenario, the discrepancy between the OSL and cosmogenic age is small (< 10 ka, especially when we look at it in a perspective of much older alluvial surfaces higher above the channel), and is most likely to be the result of flood impact on lower terraces and sporadic transport of material in the stream.

Simple exposure ages of all surficial samples (desert pavement and boulders) are significantly older (15%–250% for desert pavement; 140%–1700% for boulders) than the model deposition ages and the OSL ages of the sandy deposits in the depth profile of the terrace. A recent study (Carretier et al., 2009) shows that clast attrition and size-dependent transport velocity can, in some cases, produce measurable differences in cosmogenic concentrations of bedload clasts. Since in arid environments, clast size does seem to influence transport times of riverbed alluvium (Clapp et al., 2000, 2002), the higher inheritance of chert clasts and quartzite boulders is more likely to reflect the difference in the bedrock erosion rates of the three different lithologies (chert, quartzite and sandstone). The high inheritance in boulders may also be explained by the limited transport and reworking of dosed boulders from adjacent higher terraces. The spatial relationships between $Q2_N$ and $Q3_N$ suggest that $Q2_N$ boulders probably rolled onto $Q3_N$ when $Q2_N$ was incised and the top surface of $Q3_N$ became the riverbed. Indeed, the ages of $Q3_N$ boulders (N1-Q3-B1, N1-Q3-B3) are bracketed between the ages of $Q3_N$ (the terrace that they are lying on) and $Q2_N$ (the terrace above them), supporting boulder reworking from higher onto lower terraces. We might speculate that the ~600-ka old boulder at $Q2_N$ has been reworked from a then-higher and now absent terrace as well. To conclude, larger clasts measured on top of the terrace show somewhat increased exposure ages, due to higher inheritance and probably reworking of dosed material from higher terraces. More work is to be done to characterize the inheritance of desert pavement clasts covering middle to late Quaternary terraces.

The ~100 ky age difference between the terrace identified as "Q2" in Neqarot Gorge ($Q2_N$) and in the Karkom Graben ($Q2_P$) (Table 3) points to an erroneous correlation of these surfaces

made at the beginning of this work: although looking similar, these terraces were aggraded at significantly different times.

Active channel sediment, inheritance and basin-wide erosion rates

Makhtesh Ramon (Figure 19) is the main sand source for quartz sandstone that is being transported in the Neqarot channel. Although upper Neqarot basin contributes sands derived from relicts of Hazeva and Arava Formations with a high ^{10}Be concentration of (3.06 ± 0.18) × 10^5 atoms g^{-1} SiO_2, this signal is overwhelmed by a great amount of sand originating from inside Makhtesh Ramon with a mean ^{10}Be concentration of (1.61 ± 0.16) × 10^5 ^{10}Be atoms g^{-1} SiO_2 (average for samples N4-R and N4-NR) (Figure 24). This concentration corresponds to an apparent basin-wide erosion rate within Makhtesh Ramon of 16 ± 2 m/Ma (Table 3). This rate is smaller by an order of magnitude than the inferred exhumation rate of the sandstone bedrock in Makhtesh Qatan (~100 m/Ma, based on in-situ ^{10}Be in the sandstone bedrock. Noa Fruchter, pers. comm., 2009), suggesting that the ^{10}Be concentration in the outlet of Makhtesh Ramon is largely influenced by a relatively long residence time of sand within Makhtesh Ramon (e.g., being stored in terraces). The characteristics of this residence mechanism have not been addressed in the present study.

The observed downstream decrease of the cosmogenic concentration from the outlet of Makhtesh Ramon down to the Neqarot Gorge site (Figure 24; Table 3) violates the steady-state assumption of Bierman and Steig (1996). Such behavior implies mixing of several sources of sediment (Clapp et al., 2000, 2002); the low concentration end-member may originate from excavated terraces where the cosmogenic signal either has decayed or has been originally low during its sedimentation. Terrace-wall collapse seems to be a significant contributor of sediment along the Neqarot stream, which is supported by the identical concentrations of all depth samples at terrace $Q3_N$ and in the adjacent active channel sediment (sample N1-SD).

The cosmogenic inheritance of sand as measured in the current active channel, and the reconstructed best-fit inheritance of sand in the depth profiles of $Q3_N$ and $Q2_N$ terraces have similar values. This can be interpreted as apparent basin-wide erosion rates ranging between 16 – 21 m/Ma; Table 5; Figure 26). Although due to terrace stripping, it is possible that the inheritance of the present active channel is dominated by a signal of a much earlier and faster erosion rate, overall these rates seem to be similar. A somewhat different trend is obtained in

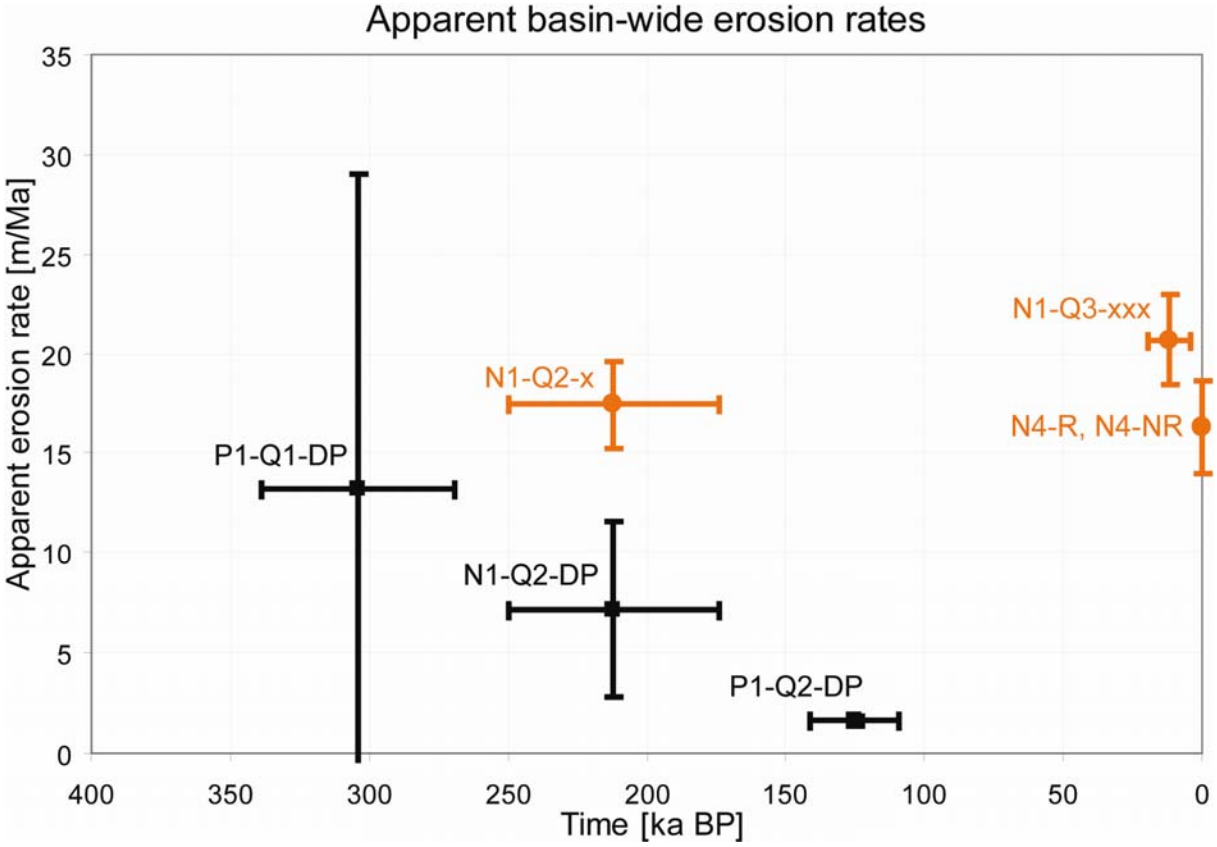

Figure 26: Apparent basin-wide erosion rates for chert and sand.
The ranges of age and erosion rate for chert (black) and sandstone (yellow) are based on individual or averaged samples as shown in Table 5)

regard to inheritance of chert, as reconstructed by deducing an OSL-age-equivalent cosmogenic concentration from the measured concentration (Equation 10). Overall, the apparent basin-wide erosion rates of chert have a much greater variance (0 – 30 m/Ma) and are generally 2 – 3 times smaller than those of sandstone. Moreover, a trend of reduction of the apparent chert erosion rate with time may be noticed (Figure 26), which is also supported by external data such as the early Pleistocene apparent chert erosion rate of ~14 m/Ma (Matmon et al., 2009) and a present-day apparent chert erosion rate of ~2 m/Ma in the Judea Desert (Itai Haviv, pers. comm., 2009). While this trend could reflect the stabilization of hard rock slopes during the Quaternary, these data must be treated carefully due to the large uncertainty in high erosion rate which is inevitable when the OSL and cosmogenic ages almost overlap. For future work, it is suggested that to clarify this trend, depth profiles of chert clasts should be collected, and the inheritance of chert be best-fitted the same way as have been done here for sand.

4.6. Summary

Middle – late Quaternary terraces preserved in the Neqarot Gorge and in Karkom Graben present a record of ancient fluvial activity including the timing of large depositional episodes and basin-wide erosion rates. The cosmogenic model deposition age (Equation 8) is a robust method of interpreting cosmogenic depth profiles as *deposition ages* of individual strata, rather than ages of abandonment. These ages can then be straightforwardly compared to OSL ages; for terraces of ~200 ka and ~10 ka in the Neqarot Gorge, ages derived using both dating techniques are in agreement. Terrace sedimentation rate, which is the least constrained parameter, can be increased or decreased within reasonable time spans (a few tens of ka) to attain a full match between OSL and model cosmogenic ages.

Cosmogenic inheritance in sediment has been estimated using best fitting of terrace depth profiles for sand samples and by subtracting an OSL-equivalent age for desert pavement samples. From the reconstructed inheritance values, apparent rates of bedrock erosion were calculated. In the last 300 ka, the apparent rate of sandstone exhumation is around 15 – 20 m/Ma; the apparent rate of chert exhumation shows a diminishing trend from ~13 m/Ma at 300 ka down to ~2 m/Ma at present. However, to validate this comparison, the inheritance of chert clasts should be determined obtaining depth profiles as well.

5. An attempt to determine the deposition time of the Arava Formation

5.1. The cosmogenic burial-dating method

The two-isotope dating method utilizes the fact that ^{26}Al decays approximately twice as fast as ^{10}Be (Lal and Arnold, 1985). The ratio of ^{26}Al/^{10}Be in a newly exposed rock is equal to the ratio between the production rates, i.e., $R(0) = P_{26} / P_{10}$. In sediment which has been dosed and then instantaneously buried, this isotopic ratio $R(t)$ decreases exponentially with the time (Lal, 1991):

$$R(t) = R(0) \cdot \exp\left((-\lambda_{26} + \lambda_{10}) \cdot t\right) \tag{12}$$

If the present-day ratio $R(t)$ is measured and $R(0)$ can be correctly assumed, Equation (12) can be solved for the burial age t (Granger et al., 1997, 2001).

Thick sequences of the Arava Formation are widely exposed within the Karkom Graben, including a 40 m–thick lacustrine sequence which interfingers with the fluviatile sequence (Garfunkel and Horowitz, 1966; Avni et al., 2001). Three deep caves of 2.3 m, 4 m and >10 m have been located within a 70 m section of the Arava and the Zehiha formations at the outlet of Nahal Arod (Figure 27). The calcareous sandy limestone of the Kuntilla Member was sampled within the caves (MK1 – 3), assuring that the sampled material has not experienced any radiation since their deposition. At the surface we sampled and analyzed the desert pavement developed on top of the Zehiha Formation (Sample MK; Figure 10b; Figure 12; Table 1) in order to determine the abandonment age of the sequence (see Chapter 3).

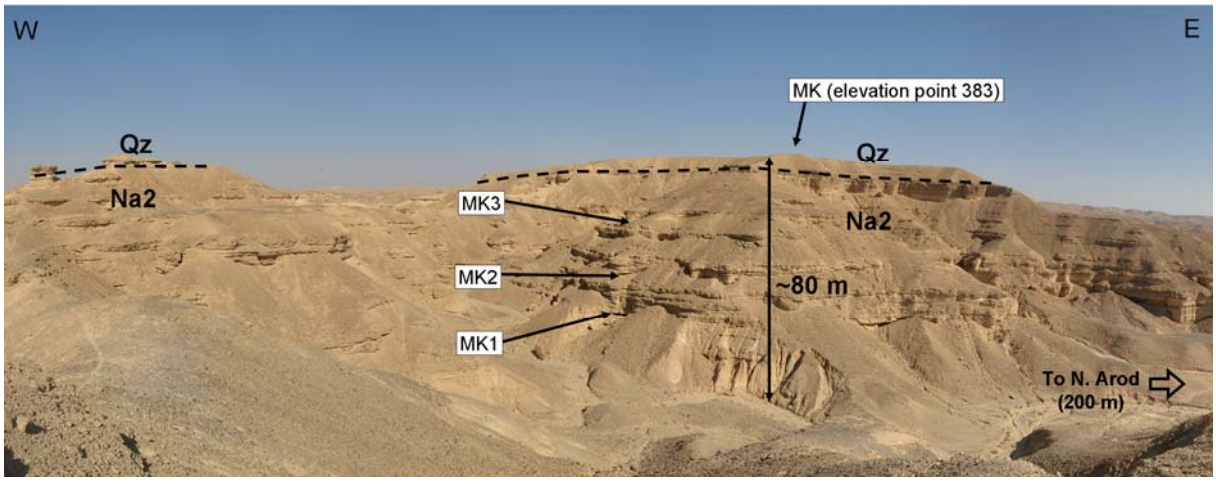

Figure 27: Arava Formation profile at Graben Karkom site.
Na2 – Kuntilla Member of the Arava Formation. Qz – Zehiha Formation. MK1,2,3 – burial dating samples. MK – surface exposure sample (1.86 ± 0.32 Ma according to ^{10}Be)

Table 6: ^{26}Al and ^{10}Be ratios and burial ages for the Arava formation at Graben Karkom.

Sample name	Profile depth	Location Lat / Lon	Elevation [m asl]	^{10}Be [10^4 atoms g^{-1}]	^{26}Al [10^4 atoms g^{-1}]	^{26}Al / ^{10}Be ratio	Burial Age [Ma]	Erosion [m/Ma]
MK	0	30°21.319' / 34°55.515'	383	616 ± 14	1414 ± 112	2.30 ± 0.19	0.90 ± 0.60	0.03 ± 0.39
MK3	48	30°21.239' / 34°55.489'	335	4.30 ± 0.62				
MK2	63	30°21.220' / 34°55.496'	320	7.46 ± 0.41	< 4.09	< 0.56	> 5.11	2.4 - 3.0
MK2*	63	30°21.220' / 34°55.496'	320	22.87 ± 0.74	2.74 ± 1.17	0.12 ± 0.05	7.07 ± 1.20	0.12 ± 0.94
MK1	67	30°21.214' / 34°55.502'	316	1.46 ± 0.41	< 2.80	< 2.34	> 2.02	32 - 107
MK1*	67	30°21.214' / 34°55.502'	316	0.63 ± 0.24	2.58 ± 1.46	4.08 ± 2.76	1.08 ± 1.44	289 ± 446

Note: Constants used for calculations are: a ^{10}Be half-life of 1.36 ± 0.07 Ma (Nishizumi et al., 2007), ^{26}Al half-life of 710 ± 5 ka (Gosse and Phillips, 2001), Sea Level High Latitude (SLHL) production rate of 4.58 ^{10}Be atoms g^{-1} SiO_2, ^{26}Al /^{10}Be production rate ratio of 6.87 (Kong et al., 2009), sediment density of 2.7 g cm^{-3} and latitude-altitude scaling factors of Stone (2000). Samples MK1, MK2, MK3 and MK were analyzed at ANSTO. Samples MK1* and MK2* represent duplicate samples reanalyzed at LLNL.

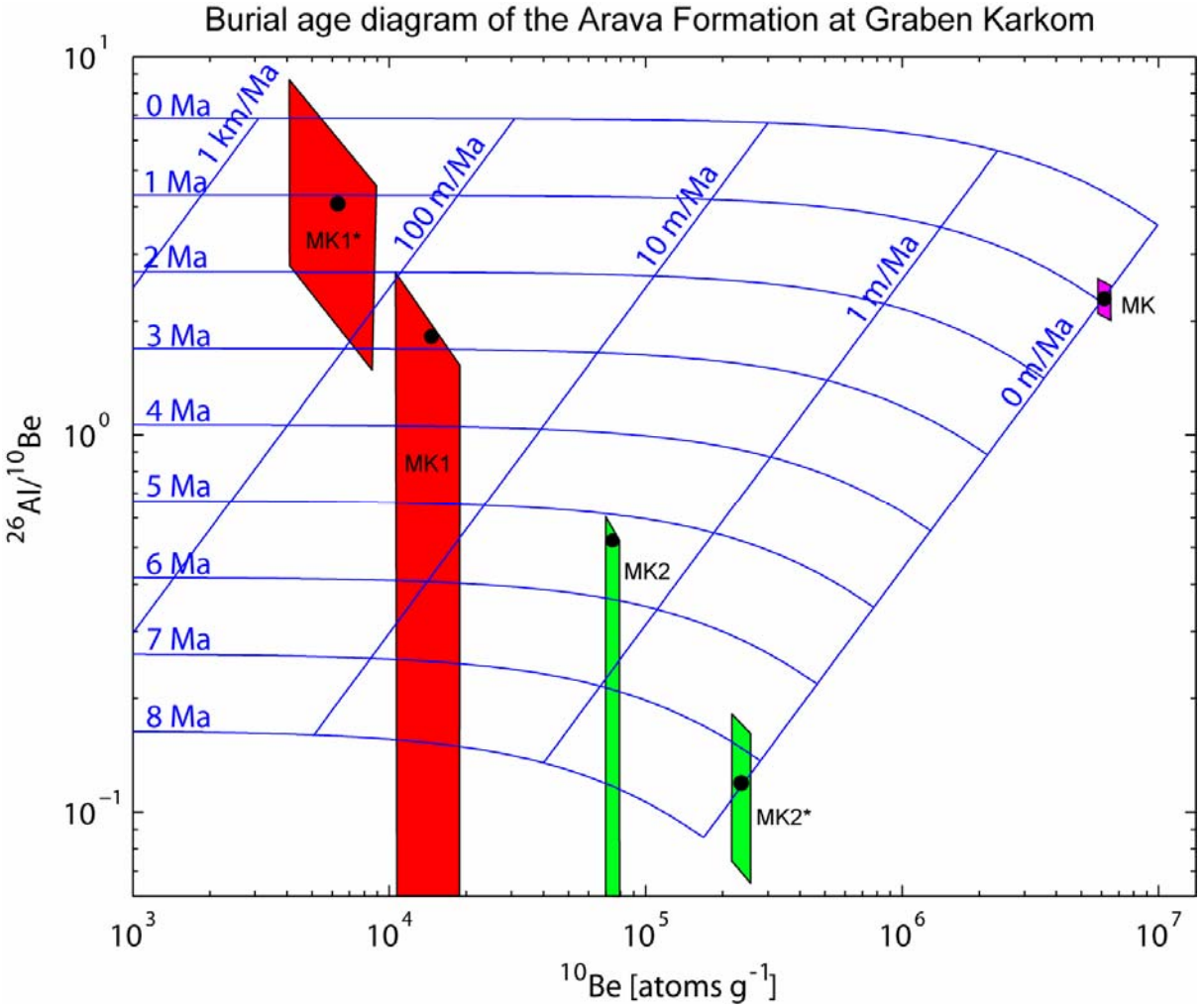

Figure 28: A plot of ^{26}Al/^{10}Be vs. ^{10}Be for the Arava Formation at Graben Karkom site.
Subhorizontal thin lines represent equal burial periods, tilted thin lines represent pre-burial erosion rates. All samples are plotted as black dots, shaded areas represent 1σ uncertainty. For MK1 and MK2 samples, the true ^{26}Al/^{10}Be ratio is not greater than indicated by the dots (see text).

5.2. Results: minimal burial ages of the Arava Formation

The upper desert paved surface yielded concentrations of (6.16 ± 0.14) × 10^6 atoms ^{10}Be g^{-1} SiO_2, and (14.14 ± 1.12) × 10^6 atoms ^{26}Al g^{-1} SiO_2 (Table 6), which correspond to simple exposure ages of 1.86 ± 0.32 Ma and 0.52 ± 0.09 Ma, respectively, and implying a severe discrepancy between the Be and Al ages. Moreover, on the $^{26}Al/^{10}Be$ vs. ^{10}Be plot, the MK data point indicates a burial signal of 0.90 ± 0.60 Ma, and falls adjacent to the "forbidden zone" (Lal, 1991; Figure 28).

The ^{10}Be and ^{26}Al concentrations of depth samples MK1 and MK2 have been first analyzed at ANSTO. However, low ^{26}Al content allowed this lab only to estimate the maximum concentration of ^{26}Al in the bulk rock (resulting in maximal $^{26}Al/^{10}Be$ ratios, and hence, minimal burial ages). More material from these samples was sent and reanalyzed in LLNL (Table 6, column 6), yielding actual (not just minimal) ^{26}Al concentrations, and reanalyzed ^{10}Be concentrations. The burial age of material from the lower cave is either >2.02 Ma (MK1) or 1.08 ± 1.44 Ma (MK1*). Similarly, the burial age of the middle cave is either >5.11 Ma (MK2) or 7.07 ± 1.20 Ma (MK2*).

5.3. Discussion

From the pedological standpoint, the soil development stage at site MK is the most mature (Stage E of Amit et al., 1993, 1996), and no evidence of profile erosion is present. From the geomorphological perspective, site MK is part of a larger and major wind gap in the central Negev, related to the abandonment of the paleo-Paran in the early Pleistocene (Avni et al., 2000; Ginat et al., 2000), which occured in this region at 1.86 ± 0.32 Ma (Table 1, p. 24). Finally, from the paleo-gradient constraints discussed in Chapter 3.3, the region of Graben Karkom has experienced only insignificant (<50 m) subsidence since the Pliocene (Table 2, p. 24), which should have only a slight effect on the production rate. Overall, there is solid geological evidence that sample MK represents an extremely ancient terrace, whose ^{10}Be concentration in chert yields an exposure age of 1.86 ± 0.32 Ma, which fits well into the established geologic and temporal framework of the central Negev (Avni et al., 2000, and in this work). Similar concentrations and ages across other major wind gaps in the central Negev argue in favor of the validity and correctness of the ^{10}Be concentration measurement, and forces us interpret the ~1 Ma "burial" signal and the point's proximity to the "forbidden zone" as an analytical problem in measuring ^{26}Al. A significantly lower-than-expected $^{26}Al/^{10}Be$ ratio in exposed chert bedrock and desert pavements are a common phenomenon, and is

currently being investigated (Ari Matmon, pers. comm., 2009). Although the lithology of samples MK1-3 is sandy limestone, small quantities of sand-sized chert fragments in samples MK2 and MK3 have been observed. Such presence of chert might be therefore the reason for the lowered $^{26}Al/^{10}Be$ ratio in samples MK2 and MK2*, and their apparent old age.

5.4. Summary

Simulatenous measurement of ^{10}Be and ^{26}Al in deeply buried sediment which has been totally shielded from cosmogenic production soon after its deposition allows calculating its burial age. In this study, we attempted to date the burial age of the upper member of the Pliocene Arava Formation in Graben Karkom. Procedural and instrumental problems encountered during extraction and measurement of ^{26}Al resulted in highly inaccurate burial ages spanning over the last 7 Ma. We therefore cannot at present refine the currently accepted 4 – 2 Ma time framework for the Arava Formation (Avni et al., 2000). More work is to be done in this field in order to obtain reasonable and valid deposition ages of the Arava Formation. Comparison of terrace abandonment ages to their deposition times will be truly fascinating, and might reveal invaluable information regarding the paleoaltimetry and the tectonic history of the region.

6. Conclusions

6.1. Overview of the major findings

As in other rifts in the world (e.g., McKee and McKee, 1972; Rosendahl, 1987), the Plio-Pleistocene subsidence of the Dead Sea rift's western margin imposed a major change on the regional drainage pattern, resulting in the fragmentation of the paleo-Paran basin into separate sub-basins and their capture towards the rift. While relicts of the paleo-Paran river are currently best preserved along major water divides, the incision history of the new basins is recorded by a "staircase" of alluvial terraces preserved at the margins of present-day streams. Upon both ancient and newer abandoned terraces, desert pavements were formed by a unique mechanism involving (i) dust accumulation beneath the original riverbed clasts (ii) zero erosion of chert clasts and (iii) the latter's constant residence on the soil. Extreme hyperaridity conditions and the exceptional non-destructive character of the DSR margin tectonics resulted in an excellent preservation of desert-paved surfaces; the cosmogenic exposure ages of these surfaces allow reconstructing the regional drainage response and reorganization to tectonics during the Quaternary, and specifically:

1. The breakdown of the paleo-Paran drainage system due to the progressive subsidence of the western margin of the Dead Sea Rift occurred at 1.8 ± 0.2 Ma, based on the average age of 5 wind gaps located along major water divides in the central and southern Negev. The record of fluvial activity within present-day basins started at ~1.4 Ma, and is continuous; however, the rarity of older surfaces is explained by rapid tectonic movements in the early Pleistocene, which probably excavated large amounts of sediment leaving but a few terraces. The pioneering age determination of 1.6 Ma of the Lower Paleolithic hand-tool bearing Zehiha formation may serve as cornerstone for establishing the temporal framework of initial hominid migration through the Levant.
2. The dependence of the cosmogenic surface production rate on altitude (~8% decrease for every 100 m of subsidence at near–sea level altitude) was used to reconstruct the elevation-time path of the "backbone of Arava", a major interbasinal ridge along the rift which survived ~200 m of Quaternary subsidence without being buried under sediment. The reconstruction which is based on comparing the cosmogenic concentration of the same unit (Zehiha Formation) across different tectonic domains (subsided vs. stable), yields an average subsidence rate of 110 – 150 m/Ma; the actual

instantaneous rate has most likely diminished from ~350 m/Ma during during 1.6 – 1.2 Ma down to ~35 m/Ma ever since 1.0 Ma.

3. Late Quaternary aggradational terraces within the present-day Neqarot and Paran basins yielded deposition ages of ~300ky, ~200ky, ~100ky and ~10ky. Good correlation between OSL and cosmogenic profile ages supports the validity of both methods. Modeled cosmogenic inheritance of sand and chert in these terrace deposits were interpreted as basin-wide paleo-erosion rates. The apparent erosion rate of sandstone seems to be at about 16 – 21 m/Ma for the last ~300 ka; the erosion rate of chert displays a trend of diminishing erosion with time (13 m/Ma at ~300 ka down to 2 m/Ma today), and may provide evidence for late Quaternary aridification of the region.

6.2. Open questions for future research

Although a reasonable spatial pattern of the *abandonment* ages of the paleo-Paran has been established, the *deposition* age of the Arava Formation is still poorly constrained. Several chemical and analytical problems (related to the measurement of ^{26}Al) must be solved in order to obtain reliable cosmogenic burial ages. It is suggested that the possibility of using the $^{26}Al/^{10}Be$ ratio in buried sediment as a paleoaltimeter should be explored, for it may serve for unveiling the very initial stages of rift-related subsidence of the Negev during Pliocene times. Easily accessible thick sections of the Arava Formation at sites NN, EY, ES and EZ present excellent locations where the two-isotope dating technique should be, in my opinion, addressed first.

The "collection" of the wind gap surfaces related to the paleo-Paran breakup can be further extended, both by sampling more water divides in the Negev, but more interestingly, by addressing the uplifted eastern shoulder of the Dead Sea rift. If terraces of the Edom River (or an analogous river) can be recognized, mapped and sampled in Jordan, the cosmogenic concentration in their pavements is likely to produce a different, "uplift" signal, which can be used for understanding the characteristics of the crustal deformation happening simultaneously on both sides of the rift. Targeting water divides in Sinai or along the Suez rift will allow a synthesis of a larger regional landscape evolution framework.

Finally, since the cosmogenic dating of terraces is performed on chert clasts, depth profiling of chert in the dated terraces seems to be a necessary task in order to characterize its

inheritance during the different periods. This is important both for correcting the ages of the younger (middle – late Pleistocene) terraces, and for adequate reconstruction of past basin-wide erosion rates in the Negev.

7. References

Aitken, M.J., 1998. An introduction to optical dating. Oxford University Press, Oxford, 267 p.

Amit, R., Enzel, Y., Sharon D., 2006. Permanent Quaternary hyperaridity in the Negev, Israel, resulting from regional tectonics blocking Mediterranean frontal systems. Geology 34, 509–512.

Amit, R., Gerson, R., Yaalon, D.H., 1993. Stages and rate of the gravel shattering process by salts in desert Reg soils. Geoderma 57, 295–324.

Amit, R., Gerson., R., 1986. The evolution of Holocene Reg (gravelly) soil in deserts – an example from the Dead Sea region. Catena 13, 59–79.

Amit, R., Harrison, J.B.J., Enzel, Y., and Porat, N., 1996. Soils as a tool for estimating ages of Quaternary fault scarps in a hyperarid environment – The southern Arava valley, the Dead Sea Rift, Israel. Catena 28, 21–45.

Amit, R., Leckach, J., Ayalon, A., Porat, N., Grodek, T., 2007, A new insight into pedogenic processes in an extremely arid environments and their paleoclimatic implications—The Negev Desert, Israel. Quaternary International 162–163, 61–75

Anderson, R.S., Repka, J.L., Dick, G.S., 1996. Explicit treatment of inheritance in dating depositional surfaces using in situ ^{10}Be and ^{26}Al. Geology 24, 47–51

Avni Y., Porat N., and Amit R. 2000b. Morphostratigraphy, soil chronosequence and luminescence dating of Pleistocene terraces at Nahal Paran, central Negev, Israel. Ann. Meet. Isr. Geol. Soc.

Avni, Y., 1998. Paleogeography and tectonics of the central Negev and the Dead Sea Rift western margin during the late Neogene and Quaternary. Geol. Surv. Isr. Rep. GSI/24/98, 231 pp. (in Hebrew, English abstr.)

Avni, Y., Bartov, Y., Garfunkel, Z., Ginat, H., 2000. The evolution of the Paran drainage basin and its relation to the Plio-Pleistocene history of the Arava Rift western margin, Israel. Isr. J. Earth Sci. 49, 215–238.

Avni, Y., Bartov, Y., Garfunkel, Z., Ginat, H., 2001. The Arava Formation – a Pliocene sequence in the Arava Valley and its western margin, southern Israel. Isr. J. Earth Sci. 50, 101–120.

Avni, Y., Zilberman, E. 2007. Landscape evolution triggered by neotectonics in the Sede Zin region, central Negev, Israel. Isr. J. Earth Sci. 55, 189–208.

Balco, G., Stone, J.O., Lifton, N.A., Dunai, T.J., 2008. A complete and easily accessible means of calculating surface exposure ages or erosion rates from ^{10}Be and ^{26}Al measurements. Quat. Geochron. 3, 174–195.

Bart, P.J., 2004. West-directed flow of the West Antarctic Ice Sheet across Eastern Basin, Ross Sea during the Quaternary. Earth Planet. Sci. Lett. 228, 425–438.

Bartov, Y., 1974. A structural and paleogeographical study of the central Sinai faults and domes. Ph.D. Thesis, Hebrew Univ., Jerusalem, 143 pp. (in Hebrew, English summary).

Bartov, Y., Agnon, A., Enzel, Y., Stein, M., 2006. Late Quaternary faulting and subsidence in the central Dead Sea basin. Isr. J. Earth Sci. 55, 17–31.

Bartov, Y., Steinitz, G., Eyal, M., Eyal, Y., 1980. Sinistral movement along the Gulf of Aqaba – its age and relation to the opening of the Red Sea. Nature 285, 220–221.

Ben-David, R., Eyal, Y., Zilberman, E., Bowman, D., 2002. Fluvial systems response to rift margin tectonics: Makhtesh Ramon area, southern Israel. Geomorphology 45, 147–163.

Bentor, Y.K., Vroman, A. 1957. The geological map of Israel, Arava Valley, Sheet 19, 1:100,000, with explanatory notes. Geol. Surv. Isr., 66 pp.

Bierman P, Steig E.J. 1996. Estimating rates of denudation using cosmogenic isotope abundances in sediment. Earth Surface Processes and Landforms 21, 125–139.

Bierman, P.R., Caffee, M.W., 2001. Slow rates of rock surface erosion and sediment production across the Namib Desert and escarpment, southern Africa. American J. Sci. 301, 326–358.

Blard, P.H., Bourles, D., Lavé, J., Pik, R., 2006. Applications of ancient cosmic-ray exposures: Theory, techniques and limitations. Quat. Geochron. 1, 59–73.

Blard, P.H., Lavé, J, Pik, R., Quidelleur, X., Bourlès, D., Kieffer, G., 2005. Fossil cosmogenic 3He record from K Ar dated basaltic flows of Mount Etna volcano (Sicily, 38°N): Evaluation of a new paleoaltimeter. Earth Planet. Sci. Lett. 236, 613–631.

Brook, E.J., Brown, E.T., Kurz, M.D., Ackert, R.P., Raisbeck, G.M., Yiou, F., 1995. Constraints on age, erosion, and uplift of Neogene glacial deposits in the Transantarctic Mountains determined from in situ cosmogenic ^{10}Be and ^{26}Al. Geology 23, 1063–1066.

Brown, E., Stallard, R.F., Larsen, M.C., Raisbeck, G.M., and Yiou, F., 1995. Denudation rates determined from the accumulation of in situ-produced 10Be in the Luquillo Experimental Forest, Puerto Rico. Earth Planet. Sci. Lett. 129:193–202.

Brown, E.T., Edmond, J.M., Raisbeck, G.M., Yiou, F. , Kurz, M.D., Brook, E.J., 1991; Examination of surface exposure ages of Antarctic moraines using in situ ^{10}Be and ^{26}Al. Geochim. Cosmochim. Acta 55, 2269–2283.

Bruno, L.A., Baur, H., Graf, T., Schlüchter, C., Signer, P., Wieler, R., 1997. Dating of Sirius Group tillites in the Antarctic Dry Valleys with cosmogenic ^{3}He and ^{21}Ne. Earth Planet. Sci. Lett. 147, 37–54.

Burbank, D.W., Anderson, R.S., 2001. Tectonic Geomorphology. Blackwell Science, Oxford, U.K. 274 pp.

Calvo, R. 2002. Stratigraphy and petrology of the Hazeva Formation in the Arava and the Negev. Geol. Surv. Isr. Rep. GSI/22/02, 264 pp. (in Hebrew, English abstr.)

Calvo, R., Bartov, Y. 2001. Hazeva Group, southern Israel: New observations, and their implications for its stratigraphy, paleogeography, and tectono-sedimentary regime. Isr. J. Earth Sci. 50, 71–99.

Carretier, S., Regard, V., Soual, C., 2009. Theoretical cosmogenic nuclide concentration in river bed load clasts: Does it depend on clast size? Quaternary Geochronology 4, 108–123

Cerling, T.E., Craig, H., 1994. Geomorphology and in-situ cosmogenic isotopes. Ann. Rev. Earth Planet. Sci. 22, 273–317.

Clapp, E.M., Bierman, P.R., Caffee, M., 2002. Using 10Be and 26Al to determine sediment generation rates and identify sediment source areas in an arid region drainage basin. Geomorphology 45, 89–104

Clapp, E.M., Bierman, P.R., Schick, A.P., Lekach, J., Enzel, Y., Caffee, M., 2000. Sediment yield exceeds sediment production in arid region drainage basins. Geology 28:995–998.

Clark, D.H., Bierman, P.R., Larsen, P., 1995, Improving in situ cosmogenic chronometers. Quat. Res. 44, 367–377.

Craddock, R.A., Maxwell, T.A., 1993. Geomorphic evolution of the Martian highlands through ancient fluvial processes. J. Geophys. Res. 98, 3453–3468

Craig, H., Poreda, R.J., 1986. Cosmogenic ^{3}He in terrestrial rocks: the summit lavas of Maui. Proc. Natl. Acad. Sci. USA 83 (7), 1970–1974.

Curtis L.J. 1978. Concept of the exponential law prior to 1900. American Journal of Physics 46:896–906

Davis, R., Schaeffer, O. A., 1955. Chlorine-36 in nature. Annals New York Acad. Sci. 62, 105–122.

Desilets, D., Zreda, M., Prabu, T., 2006. Extended scaling factors for in situ cosmogenic nuclides: New measurements at low latitude. Earth Planet. Sci. Lett. 246, 265–276.

Desilets, D., Zreda, M.G., 2003. Spatial and temporal distribution of secondary cosmic-ray nucleon intensities and applications to in situ cosmogenic dating. Earth Planet. Sci. Lett. 206, 21–42.

Dunai, T.J., 2000. Scaling factors for production rates of in situ produced cosmogenic nuclides: a critical reevaluation. Earth Planet. Sci. Lett. 176, 157–169.

Dunai, T.J., 2001. Influence of secular variation of the geomagnetic field on production rates of in situ produced cosmogenic nuclides. Earth Planet. Sci. Lett. 193, 197-212.

Faure G., Mensing T.M., 2005. Isotopes: principles and applications. Wiley, Hoboken, NJ, pp 897

Fink, D., Hotchkis, M.A.C., Hua, Q., Jacobsen, G.E., Smith, A.M., Zoppi, U., Child, D., Mifsud, C., van der Gaast, H.A., Williams, A.A., Williams, M., 2004. The ANTARES AMS facility at ANSTO. Nucl. Instr. and Meth. B109, 223–224.

Fink, D., Smith, A., 2007. An inter-comparison of ^{10}Be and ^{26}Al AMS reference standards and the ^{10}Be half-life. Nucl. Instr. Meth. Phys. Res. B259, 600–609.

Fitzgerald, P. J., Gleadow, A. J. W., 1990. New approaches in fission track geochronology as a tectonic tool: Examples from the transantarctic mountains. International Journal of Radiation Applications and Instrumentation. Part D. Nuclear Tracks and Radiation Measurements, 17, 351-357

Garfunkel, Z., 1970. The tectonics of the western margin of the southern Arava. Ph.D thesis, Hebrew Univ., Jerusalem, 204 p. (in Hebrew, English abstr.)

Garfunkel, Z., 1981. Internal structure of the Dead Sea leaky transform (rift) in relation to plate kinematics. Tectonophysics 80, 81–108.

Garfunkel, Z., 1988. Relations between continental rifting and uplifting: evidence from the Suez rift and northern Red Sea. Tectonophysics 150, 33–49.

Garfunkel, Z., Horowitz, A. 1966. The Upper Tertiary and Quaternary morphology of the Negev, Israel. Isr. J. Earth Sci. 15, 101–117.

Gerson, R., Grossman, S., Bowman, D., 1985. Stages in the Creation of a Large Rift Valley, Geomorphic Evolution Along the Southern Dead Sea Rift. In: Morisawa, M. and Hack, J.T. (Eds.). Tectonic Geomorphology, Allen & Unwin, Boston, pp. 53–73.

Ginat, H., 1997. Paleogeography and landscape evolution of the Nahal Hiyyon and Nahal Zihor basins (sedimentology, climatic and tectonic aspects). Geol. Surv. Isr. Rep. GSI/19/97, 206 pp. (in Hebrew, English abstr.)

Ginat, H., Enzel Y., Avni, Y., 1998. Translocated Plio-Pleistocene drainage systems along the Arava fault of the Dead Sea transform. Tectonophysics 284, 151–160.

Ginat, H., Zilberman, E., Amit, R., 2002. Red sedimentary units as indicator for reconstructing Early Pleistocene tectonic activity in the Southern Negev desert, Israel. Geomorphology 45, 127–146.

Ginat, H., Zilberman, E., Avni, Y., 2000. Tectonic and paleogeographic significance of the Edom River, a Pliocene stream that crossed the Dead Sea Rift valley. Isr. J. Earth Sci. 49, 159–177.

Ginat, H., Zilberman, E., Saragusti, I., 2003. Early pleistocene lake deposits and Lower Paleolithic finds in Nahal (wadi) Zihor, Southern Negev desert, Israel. Quat. Res. 59, 445–458.

Gosse, J., Stone, J., 2001, Terrestrial cosmogenic nuclide methods passing milestones toward palaeo-altimetry. EOS 82, p. 82, 86, 89

Gosse, J.C., Phillips, F.M., 2001. Terrestrial in situ cosmogenic nuclides: theory and application. Quat. Sci. Rev. 20, 1475–1560.

Granger, D. E., Muzikar, P., 2001. Dating sediment burial with cosmogenic nuclides: Theory, techniques, and limitations, Earth Planet. Sci. Lett. 188, 269–281.

Granger, D.E., Kirchner, J.W., and Finkel, R., 1996. Spatially averaged long-term erosion rates measured from in-situ produced cosmogenic nuclides in alluvial sediment. J. Geology 104, 249–257.

Greenbaum, N., Enzel, Y., Schick, A.P., 2001. Magnitude and frequency of paleofloods and historical floods in the Arava basin, Negev Desert, Israel. Isr. J. Earth Sci. 50, 159–187.

Hall, J.K., 1993. The GSI digital terrain model (DTM) project completed. Geological Survey of Israel Current Research 8, 47– 50.

Holzforster, F., Schmidt, U., 2007. Anatomy of a river drainage reversal in the Neogene Kivu–Nile Rift. Quat. Sci. Rev. 26, 1771–1789.

Kafri, U., Heimann, A., 1994. Reversal of the palaeodrainage system in the sea of Galilee area as an indicator of the formation timing of the Dead Sea rift valley base level in northern Israel. Palaeog., Palaeocl., Palaeoec. 109, 101–109.

Keller, E.A., Gurrola, L., Tiernay, T.E., 1999. Geomorphic criteria to determine direction lateral propagation of reverse faulting and folding. Geology 27, 515–518.

Klein J., Giegengack R., Middleton R., Sharma P., Underwood J.R., Weeks, R.A., 1986. Revealing histories of exposure using in situ produced ^{26}Al and ^{10}Be in Libyan desert glass. Radiocarbon 28, 547–555.

Kohl, C.P., Nishiizumi, K., 1992. Chemical isolation of quartz for measurement of in-situ-produced cosmogenic nuclides. Geochim. Cosmochim. Acta 56, 3583–3587.

Kong, P., Granger, D.E., Wu, F., Caffee, M.W., Wang, Y., Zhao, X., Zheng, Y., 2009. Cosmogenic nuclide burial ages and provenance of the Xigeda paleo-lake: Implications for evolution of the Middle Yangtze River. Earth Planet. Sci. Lett. 278, 131–141

Kurz, M.D., Colodner, D, Trull, T.W., Moore, R.B., O'Brien, K., 1990. Cosmic-ray exposure dating with in situ produced cosmogenic ^{3}He: results from young Hawaiian flows. Earth Planet. Sci. Lett. 97, 177–189.

Lal, D., 1991. Cosmic ray labeling of erosion surfaces: in situ nuclide production rates and erosion models. Earth Planet. Sci. Lett. 104, 424–439.

Lal, D., Arnold, J.R., 1985. Tracing quartz through the environment. Proceedings of the Indian Academy of Science (Earth Planetary Science Section) 94, 1-5.

Lal, D., Peters, B., 1967. Cosmic ray produced radioactivity on the Earth. In: Sitte, K. (Ed.), Handbuch Der Physik. Springer–Verlag, Berlin, pp. 551–612.

Leavy, B.D., Phillips, F.M., Elmore, D., Kubik, P.W., Gladney, E., 1987. Measurement of cosmogenic ^{36}C1/Cl in young volcanic rocks: an application of accelerator mass spectrometry in geochronology. Nuclear Instr. Meth. Phys. Res. B29, 246–250.

Lifshitz, A., Livnat, A., Flexer, A., 1985. The geology of Nahal Yaalon. Isr. Geol. Soc. Ann. Meet. Yotvata, 181-186

Lifton, N.A., Bieber, J.W., Clem, J.M., Duldig, M.L., Evenson, P., Humble, J.E., Pyle, R., 2005. Addressing solar modulation and long-term uncertainties in scaling in situ cosmogenic nuclide production rates. Earth Planet. Sci. Lett. 239(1–2), 140–161

Lifton, N.A., Smart, D.F., Shea, M.A., 2008. Scaling time-integrated in situ cosmogenic nuclide production rates using a continuous geomagnetic model. Earth Planet. Sci. Lett. 268, 190–201.

Livnat, A., Kronfeld, J., 1990. Pleistocene lakes in the Arava Rift of Israel (Sayif Formation): facies and paleoenvironmental setting. J. Afr. Earth Sci. 10: 409–420.

Mack, G.H., Seager, W.R., Leeder, M.R., Perez-Arlucea, M., Salyards, S.L., 2006. Pliocene and Quaternary history of the Rio Grande, the axial river of the southern Rio Grande rift, New Mexico, USA. Earth Sci. Rev. 79 (1-2), 141–162.

Mandl, G., 1987. Tectonic deformation by rotating parallel faults: the "bookshelf" mechanism. Tectonophysics, 141, 277-316.

Matmon, A., Enzel, Y., Zilberman E., Heimann A., 1999. Late Pliocene and Pleistocene reversal of drainage systems in northern Israel: tectonic implications. Geomorphology 28, 43–59

Matmon, A., Simhai, O., Amit, R., Haviv, I., Enzel, Y., Porat, N., McDonald, E.V., Benedetti, L., Finkel, R.C., 2009. Desert pavement–coated surfaces in extreme deserts present the longest-lived landforms on Earth. Geol. Soc. Am. Bull., doi: 10.1130/B26422.1.

McFadden, L.D., Wells, S.G., Jercinovic, M.J., 1987. Influences of aeolian and pedogenic processes on the evolution and origin of desert pavements. Geology 15, 504–508.

McKee, E.D., McKee, E.H., 1972. Pliocene uplift of the Grand Canyon Region – time of drainage adjustment, Geol. Soc. Am. Bull. 83, 1923–1932.

Murray, A., Wintle, A.G., 2000. Luminescence dating of quartz using an improved single-aliquot regenerative-dose protocol. Radiation Measurements 32, 57–73.

Neev, D., 1960. A Pre-Neogene erosion channel in the southern coastal plain of Israel. Geol. Surv. Isr. Bull. 25, 20 pp.

Nichols, K. K., Bierman, P. R., Hooke, R. L., Clapp, E. M., and Caffee, M., 2002. Quantifying sediment transport on desert piedmonts using ^{10}Be and ^{26}Al: Geomorphology 45, 105–125.

Nichols, K.K., Bierman, P.R., Eppes, M.C., Caffee, M., Finkel, R., Larsen, J., 2005. Deciphering the late Pleistocene and Holocene history of the complex Chemehuevi Mountain piedmont using ^{10}Be and ^{26}Al. Am. J. Sci. 305, 345–368.

Nishiizumi, K., Imamura, M., Caffee, M.W., Southon, J.R., Finkel, R.C., McAninch, J. 2007. Absolute calibration of ^{10}Be AMS standards. Nucl. Instr. Methods in Phys. Res. B, 258–403.

Nishiizumi, K., Kohl, C.P., Arnold, J.R., Klein, J., Fink, D., Middleton, R., 1991. Cosmic ray produced 10Be and 26Al in Antarctic rocks: exposure and erosion history. Earth Planetary Sci. Lett. 104, 440-454.

Nishiizumi, K., Winterer, K., Kohl, C.P., Klein, J., Middleton, R., Lal, D., Arnold J.R., 1989. Cosmic ray production rates of ^{10}Be and ^{26}Al in quartz from glacially polished rocks. J. Geophys. Res. 94 (B12), 17 907–17 915.

Ollier, C.D., 1995. Tectonics and landscape evolution in southeast Australia. Geomorphology 12, 37–44.

Phillips, F.M., Leavy, B.D., Jannik, N.O., Elmore, D., Kubik, P., 1986. The accumulation of cosmogenic chlorine-36 in rocks: a method for surface exposure dating. Science 231, 41-43.

Phillips, W.M., McDonald, E.V., Reneau, S.L., Poths, J., 1998. Dating soils and alluvium with cosmogenic 21Ne depth profiles: case studies from the Pajarito Plateau, New Mexico, USA. Earth Planet. Sci. Lett. 160, 209–223.

Picard, L., 1943. Structure and evolution of Palestine (with comparative notes on neighbouring countries). Hebrew Univ., Jerusalem, Dept. Geol. Bull. 4(2–4), 187 pp.

Porat, N. 2007. Analytical procedures in the luminescence dating laboratory. Isr. Geol. Surv. technical report TR-GSI/08/2007, 33 P.

Rabb'a, I. 1994. The geology of the Al Qurayqira (Jabel Hamra Faddan) map, sheet no. 3051-II, scale 1:50,000. Natural Resources Authority, Jordan. Bull. 28, 60 pp.

Repka, J.L., Anderson, R.S., Finkel, R.C., 1997. Cosmogenic dating of fluvial terraces, Fremont River, Utah; Earth Planet. Sci. Lett. 152, 59–73.

Robinson, R.A.J., Spencer, J.Q.G., Phillips, W.M., Strecker, M.R., Alonso, R.N., Kubik, P.W., 2004. Integrating Optically Stimulated Luminescence and cosmogenic nuclide dating methods to constrain the timing and rates of sedimentation and erosion in late quaternary deposits of NW Argentina. Geophys. Res. Abstr. 6, 06179

Ron, H., Levi, S., 2001. When did hominids first leave Africa?: New high-resolution magnetostratigraphy from the Erk-el-Ahmar Formation, Israel. Geology 29, 887–890.

Rosendahl, B.R., 1987. Architecture of continental rift with special reference to East Africa, Ann. Rev. Earth Planet. Sci. 15, 445–503.

Rosenfeld, A., Avni, Y., Ginat, H., Honigstein, A., Scarpa, D., Saragusti, I., 1997. Pliocene - Pleistocene paleo-lakes in the Arava Valley, southern Israel – Ostracods and Homo erectus. Abstr. 13th Intern. Symp. Ostracods, Univ. of Greenwich, U.K.

Rutherford, E., 1900. A Radioactive Substance emitted from Thorium Compounds. Philosophical Magazine, ser. 5, xlix, 1-14

Rutherford, E., Soddy, F., 1902. The cause and nature of radioactivity. Philos. Mag. 4, 370–396 [as abridged and reprinted in Henry A. Boorse and Lloyd Motz, The World of the Atom, Vol. 1 (New York: Basic Books, 1966)].

Sakal, E. 1967. The geology of the Menuha Ridge. M.Sc. Thesis, Hebrew Univ., Jerusalem, 80 pp. (in Hebrew).

Schäfer, J.M., Ivy-Ochs, S., Wieler, R., Leyo, I., Baur, H., Denton, G.H., Schlüchter, C., 1999. Cosmogenic noble gas studies in the oldest landscape on earth: surface exposure ages of the Dry Valleys, Antarctica. Earth Planet. Sci. Lett. 167, 215–226.

Shaw, S.H. 1947. Geological map of southern Palestine, 1:250,000, with explanatory notes. Gov. Printing Office, Jerusalem, 42 pp.

Simhai, O., Matmon, A., Amit, R., Enzel, Y., Haviv, I., McDonald, E. V., Porat, N., Finkel, R. C. 2007. The age of the ancient, tectonically stable Paran Plains, and their sedimentological and pedological characteristics. Isr. Geol. Soc. Abstracts p.115

Sneh, A., 1982. Quaternary of the northwestern Arava, Israel. Isr. J. Earth Sci. 31:9-16

Sneh, A., Bartov, Y., Rosensaft, M., 1998. Geological Map of Israel – 1:200,000 (4 sheets). Jerusalem: Geological Survey of Israel - Jerusalem.

Srinivasan, B., 1976. Barites: anomalous xenon from spallation and neutron induced reactions. Earth Planet. Sci. Lett. 31,129–141.

Stone, J.O., 2000. Air pressure and cosmogenic isotope production. J. Geophys. Res. 105, 23 753– 23 759.

Summerfield, M.A., 1991. Global Geomorphology: an introduction to the study of landforms. Longman Scientific and Technical, Boston, 537pp.

Swinehart, D.J., 1962. The Beer-Lambert law. J. Chem. Edu. 39:333–335

Tchernov, E., 1987. The age of 'Ubeidiya Formation – an Early Pleistocene hominid site in the Jordan Valley. Israel J. Earth Sci. 36, 3–30.

Van der Wateren, F.M., Cloetingh S.A.P.L., 1999. Feedbacks of lithosphere dynamics and environmental change of the Cenozoic West Antarctic Rift System. Global Planet. Change 23, 1–24.

Wdowinski, S., Zilberman, S., 1997. Systematic analyses of the large-scale topography and structure across the Dead Sea Rift. Tectonics 16, 409–424.

Wells, S.G., McFadden, L.D., Poths, J., Olinger, C.T., 1995. Cosmogenic ^{3}He exposure dating of stone pavements: implications for landscape evolution in deserts. Geology 23, 613–616.

Zak, I., Freund, R., 1981. Asymmetry and basin migration in the Dead Sea Rift. Tectonophysics 80, 27–38.

Zelilidis, A., 2000. Drainage evolution in a rifted basin, Corinth graben, Greece. Geomorphology 35, 69–85.

Zilberman, E., 2000. Formation of "makhteshim" – unique erosion cirques in the Negev, southern Israel. Isr. J. Earth Sci. 49, 127–141

Zilberman, E., Amit, R., Heimann, A., Porat, N., 2000. Changes in Holocene paleoseismic activity in the Hula pull-apart basin, northern Dead Sea Rift, Israel. Tectonophysics 321, 237–252.

Zilberman, E., Avni, Y., 2006. The Hemar Conglomerate – a remnant of a middle-late Miocene cross-rift stream. Geol. Soc. Isr. Ann. Meet., p. 138.

Zilberman, E., Baer, G., Avni, Y., Feigin, D., 1996. Pliocene fluvial systems and tectonics in the central Negev, southern Israel. Isr. J. Earth. Sci. 45, 113–126.

8. Appendices

8.1. Cosmogenic isotopes: raw data, age calculations

In this work, 41 new cosmogenic samples have been processed and analyzed. The raw results (including 2 recalculated samples from a previous study of Matmon et al., 2009) are summarized in Table 7. Each sample is represented by a row; the columns containing information about each sample are grouped into field data (columns 1-16), lab data (columns 17-25), AMS data (columns 26-38) and calculations of concentration and exposure age (columns 39-55). The meaning of data in each column and its calculation steps (if exist) appear in the pages following the table.

Propagation of uncertainty for *each calculated value* was done via the full differential of the function that produced it as described below. Let f be a function of n variables: $f(X_1, X_2, \ldots, X_n)$, and u be its value for a particular set of variables: $u = f(x_1 \pm \sigma_1, x_2 \pm \sigma_2, \ldots, x_n \pm \sigma_n)$. We can express the uncertainty in u using the full differential of f as follows:

$$\sigma_u = \sqrt{\sum_{i=1}^{n} \left(\frac{\partial f(x_1, x_2, \ldots, x_n)}{\partial X_i} \right)^2 \cdot \sigma_i^2} \qquad (13)$$

In the above formula (also known as the "law of combination of errors"), the covariance terms have been neglected, assuming that the variables and their uncertainties are not dependent on each other.

Table 7a: Field and cosmogenic lab raw data

1	2	3	4	5	6	7	8	9	10	11	12	13	14	15	16	17	18	19	20	21	22
SAMPLE ID	**ALIAS**	**ORD**	**TYPE**	**LITHO-LOGY**	**BASIN**	**ITM EAST**	**ITM NORTH**	**LON**	**LAT**	**ALT**	**DEPTH**	**DENSITY**	**SAMPLE THICK.**	**TOPO SHIELD.**	**DIST**	**SAMPLE MASS**	**BE CAR. MASS**	**AL CAR. MASS**	**DILUTED SAMPLE**	**ALIQUOT MASS**	**DILUTED ALIQUOT**
									lat	*z*	*x*	*ρ*	*h*	*ft*	*l*	*ws*	*wcbe*	*wcal*	*ws'*	*wa*	*wa'*
						[m]	[m]	[deg]	[deg]	[masl]	[m]	[g cm^{-3}]	[cm]		[km]	[g]	[g]	[g]	[g]	[g]	[g]
24 N5-Na1-DP	NN	34	DP on inset	chert	Nemiya	217864	507027	35.18714	30.65316	-5	0	2.7	1.5	1.000	1.0	20.184	0.303	0.298	136.427	1.369	10.017
24 M1-WG3-DP	KK	32	DP on windgap	chert	Meshar	200691	487231	35.00833	30.47445	388	0	2.7	1.5	1.000	6.9	20.062	0.303	0.201	143.866	1.356	9.956
24 M1-WG2-DP	KM	31	DP on windgap	chert	Meshar	199158	483509	34.99244	30.44085	405	0	2.7	1.5	1.000	7.1	20.179	0.303	0.200	144.031	1.347	9.952
28 M1-ARI-DPQ	KZ	38	DP on inset	chert	Meshar	193700	483600	34.93562	30.44157	380	0	2.7	1.5	1.000	2.5	20.017	0.308	0.201	139.185	1.363	10.071
24 Z1-Na-DP	MZ	33	DP on inset	chert	Zihor	200280	468960	35.00439	30.30963	275	0	2.7	1.5	1.000	16.4	20.155	0.302	0.297	139.457	1.343	10.069
12 P1-Z1	MK	7	DP on windgap	chert	Arod	192681	474041	34.92526	30.35532	383	0	2.7	1.5	1.000	7.0	22.923	0.302	0.000	139.678	1.328	9.947
23 Y1-Nae-DPS	EY-R	26	DP on inset	chert	Yaalon	209511	444568	35.10059	30.08971	328	0	2.7	1.5	1.000	36.9	20.018	0.303	0.502	143.310	1.363	n/a
23 Y1-Nae-DPN	EY	25	DP on inset	chert	Yaalon	209635	444622	35.10188	30.09020	331	0	2.7	1.5	1.000	36.9	20.085	0.303	0.502	132.046	1.382	n/a
24 S2-Q1-DP	ES	35	DP on windgap	chert	Shitta	208342	450873	35.08840	30.14658	255	0	2.7	1.5	1.000	33.0	20.103	0.303	0.300	124.295	1.405	10.039
24 H1-Nae-DP	EH	36	DP on inset	chert	Hiyyon	196437	453716	34.96477	30.17205	355	0	2.7	1.5	1.000	20.8	20.032	0.303	0.300	143.401	1.345	10.093
24 Z2-Nae-DP	EZ	37	DP on windgap	chert	Zihor	193184	456055	34.93094	30.19309	433	0	2.7	1.5	1.000	16.9	20.096	0.302	0.200	146.641	1.348	10.042
PS-4-DP	PS4	41	DP on windgap	chert	Paran	179414	444094	34.78840	30.08482	522	0	2.7	1.5	1.000	0.5	32.931	0.302				
PS-6-DP	PS6	42	DP on windgap	chert	Paran	180627	436571	34.80126	30.01699	545	0	2.7	1.5	1.000	1.3	35.132	0.298				
19 PS-8	PS8	43	DP on inset	chert	Paran	173912	449419	34.73110	30.13266	450	0	2.7	1.5	1.000	1.0	25.011	0.305	0.102	156.419	1.403	9.926
12 N1-SD	N1-SD	1	stream sediment	sand	Neqarot	210172	507985	35.10688	30.66176	70	0	1.8	5.0	0.997		31.888	0.333	0.995	194.082	1.321	9.894
12 N1-Q3-B1	N1-Q3-B1	4	boulder on inset	quartzite	Neqarot	210073	508041	35.10585	30.66227	73	0	2.7	5.0	0.999		25.045	0.306	1.015	157.563	1.329	10.042
21 N1-Q3-B3	N1-Q3-B3	19	boulder on inset	quartzite	Neqarot	210048	507971	35.10559	30.66164	73	0	2.7	5.0	0.999		25.151	0.305	1.014	150.697	1.415	10.117
12 N1-Q3-015	N1-Q3-015	2	inset profile	sand	Neqarot	210078	508015	35.10590	30.66203	73	0.05	1.8	15.0	0.999		27.485	0.310	1.009	166.174	1.347	9.899
22 N1-Q3-030	N1-Q3-030	21	inset profile	sand	Neqarot	210078	508015	35.10590	30.66203	73	0.20	1.8	20.0	0.999		30.091	0.309	0.500	186.293	1.408	10.264
22 N1-Q3-070	N1-Q3-070	22	inset profile	sand	Neqarot	210078	508015	35.10590	30.66203	73	0.60	1.8	20.0	0.999		30.150	0.306	0.512	179.776	1.391	10.016
21 N1-Q3-090	N1-Q3-090	20	inset profile	sand	Neqarot	210078	508015	35.10590	30.66203	73	0.80	1.8	30.0	0.999		30.118	0.305	0.503	170.336	1.429	10.051
22 N1-Q3-140	N1-Q3-140	23	inset profile	sand	Neqarot	210078	508015	35.10590	30.66203	73	1.30	1.8	20.0	0.999		35.050	0.306	0.506	192.018	1.438	9.992
22 N1-Q3-190	N1-Q3-190	24	inset profile	sand	Neqarot	210078	508015	35.10590	30.66203	73	1.80	1.8	20.0	0.999		35.091	0.305	0.506	225.201	1.419	9.977
12 N1-Q3-210	N1-Q3-210	3	inset profile	sand	Neqarot	210078	508015	35.10590	30.66203	73	2.00	1.8	20.0	0.999		41.352	0.325	1.010	217.553	1.361	10.038
21 N1-Q2-B1	N1-Q2-B1	17	boulder on inset	s. dol.	Neqarot	209956	507867	35.10463	30.66070	78	0	2.7	5.0	0.998		25.017	0.305	0.306	146.313	1.420	9.709
21 N1-Q2-B2	N1-Q2-B2	18	boulder on inset	quartzolite	Neqarot	209969	507884	35.10476	30.66085	78	0	2.7	5.0	0.998		25.068	0.303	0.301	145.319	1.419	9.855
12 N1-Q2-DP	N1-Q2-DP	5	DP on inset	chert	Neqarot	209955	507893	35.10462	30.66093	78	0	2.7	1.5	0.999		26.293	0.301	0.000	155.713	1.337	9.914
18 N2-Q2-6B	N2-Q2-6	13	inset profile	sand	Neqarot	209962	507856	35.10469	30.66060	78	0.83	1.8	10.0	0.997		25.023	0.304	0.503	161.120	1.384	10.074
21 N2-Q2-5	N2-Q2-5	16	inset profile	sand	Neqarot	209962	507856	35.10469	30.66060	78	2.20	1.8	10.0	0.997		30.099	0.305	0.503	176.406	1.430	10.078
18 N2-Q2-4	N2-Q2-4	12	inset profile	sand	Neqarot	209962	507856	35.10469	30.66060	78	3.06	1.8	10.0	0.997		30.026	0.303	0.502	183.398	1.417	10.220
21 N2-Q2-3	N2-Q2-3	15	inset profile	sand	Neqarot	209962	507856	35.10469	30.66060	78	4.09	1.8	10.0	0.997		30.136	0.304	0.503	176.945	1.417	9.985
21 N2-Q2-2	N2-Q2-2	14	inset profile	sand	Neqarot	209962	507856	35.10469	30.66060	78	4.69	1.8	10.0	0.997		30.193	0.305	0.504	179.750	1.428	10.012
18 N2-Q2-1	N2-Q2-1	11	inset profile	sand	Neqarot	209962	507856	35.10469	30.66060	78	5.31	1.8	10.0	0.997		29.993	0.304	0.501	166.012	1.425	10.081
23 N4-N-SD	N4-N-SD	27	stream sediment	sand	Neqarot	193979	499771	34.93813	30.58744	405	0	1.8	5.0	0.993		30.056	0.310	0.503	205.369	1.359	n/a
23 N4-R-SD	N4-R-SD	29	stream sediment	sand	Ramon	193921	501149	34.93749	30.59986	390	0	1.8	5.0	1.000		30.085	0.303	0.501	200.976	1.384	n/a
23 N4-NR-SD	N4-NR-SD	28	stream sediment	sand	Neqarot	194433	500185	34.94285	30.59118	380	0	1.8	5.0	0.966		30.008	0.305	0.503	200.635	1.369	n/a
18 P1-Q2-DP	P1-Q2-DP	10	DP on inset	chert	Paran	193291	472444	34.93164	30.34093	273	0	2.7	1.5	1.000		28.497	0.302	0.000	172.021	1.401	10.012
12 P1-Q1-DPS	P1-Q1-DPS	6	DP on inset	chert	Paran	194736	472572	34.94667	30.34211	284	0	2.7	1.5	1.000		26.837	0.308	0.000	148.713	1.386	10.061
23 P2-A3	MK3	30	windgap profile	s. lst. **	Arod	192638	473893	34.92481	30.35398	335	48.00	2.7	10.0	0.999		35.104	0.305	0.502	228.964	1.376	10.177
18 P1-A2	MK2	9	windgap profile	s. lst. **	Arod	192650	473858	34.92494	30.35367	320	63.00	2.7	10.0	0.996		37.202	0.303	0.503	226.274	1.416	10.079
29A P1-A2	MK2*	40	windgap profile	s. lst. **	Arod	192650	473858	34.92494	30.35367	320	63.00	2.7	10.0	0.996		35.010	0.210	0.304	181.769	1.460	9.853
18 P1-A1	MK1	8	windgap profile	s. lst. **	Arod	192659	473847	34.92503	30.35357	316	67.00	2.7	10.0	0.996		37.087	0.304	0.503	224.508	1.403	10.068
29A P1-A1	MK1*	39	windgap profile	s. lst. **	Arod	192659	473847	34.92503	30.35357	316	67.00	2.7	10.0	0.996		35.001	0.204	0.306	209.911	1.436	9.891

* s. dol. = silicified dolomite ** s. lst. = sandy limestone

Table 7b: ICP and AMS raw data

1	2	23	24	25	26	27	28	29	30	31	32	33	34	35	36	37	38
SAMPLE ID	**ALIAS**	**TOTAL AL (ICP)**			**AMS LAB**	**CATH.**	**REF**	**MEASURED 10Be/9Be**			**NEW**	**RECALC'D**	**AMS LAB**	**CATH.**	**MEASURED 26Al/27Al**		
		MEAS	**ERR**	**ERR**	**NAME**	**ID**	**STD**	**RATIO**	**ERR**	**ERR**	**STD**	**10/9 RATIO**	**NAME**	**ID**	**RATIO**	**ERR**	**ERR**
		al		*σal*			*std*	*R1*	*σR1*		*std'*	*R1'*			*R2*	*σR2*	
		[ppm]	**[%]**	**[ppm]**			**[10^{-12}]**	**[10^{-15}]**	**[10^{-15}]**	**[%]**	**[10^{-12}]**	**[10^{-15}]**			**[10^{-15}]**	**[10^{-15}]**	**[%]**
24 N5-Na1-DP	NN				ANSTO	B3424	30200	2890.7	43.1	1.5%	27750	2656.2	ANSTO	?	705.2	39.7	5.6%
24 M1-WG3-DP	KK				ANSTO	B3422	30200	2687.4	41.4	1.5%	27750	2469.4	ANSTO	?	515.2	33.2	6.4%
24 M1-WG2-DP	KM				ANSTO	B3421	30200	1428.7	51.7	3.6%	27750	1312.8	ANSTO	?	237.6	22.5	9.5%
28 M1-ARI-DPQ	KZ				LLNL	BE26322	28500	2378.1	42.1	1.8%	28500	2378.1					
24 Z1-Na-DP	MZ				ANSTO	B3423	30200	5187.3	96.0	1.9%	27750	4766.5	ANSTO	?	651.8	35.1	5.4%
12 P1-Z1	MK	8.117	5.0%	0.406	ANSTO	B2861	30200	7766.9	83.1	1.1%	27750	7136.8	ANSTO	A1689	1710.2	99.7	5.8%
23 Y1-Nae-DPS	EY-R				ANSTO	B3414	30200	3307.5	57.2	1.7%	27750	3039.2	ANSTO	?	1588.2	93.6	5.9%
23 Y1-Nae-DPN	EY				ANSTO	B3413	30200	3860.3	98.4	2.6%	27750	3547.1	ANSTO	?	1773.7	87.4	4.9%
24 S2-Q1-DP	ES				ANSTO	B3425	30200	5639.3	81.2	1.4%	27750	5181.8	ANSTO	?	778.8	41.2	5.3%
24 H1-Nae-DP	EH				ANSTO	B3426	30200	2380.4	32.1	1.4%	27750	2187.3	ANSTO	?	1148.9	64.2	5.6%
24 Z2-Nae-DP	EZ				ANSTO	B3427	30200	6744.9	88.4	1.3%	27750	6197.7	ANSTO	?	1348.0	44.2	3.3%
PS-4-DP	PS4				LLNL	BE22963	31500	11683.9	218.7	1.9%	28500	10571.2					
PS-6-DP	PS6				LLNL	BE22968	31500	14429.9	258.2	1.8%	28500	13055.7					
19 PS-8	PS8				LLNL	BE25258	28500	6011.9	138.9	2.3%	28500	6011.9					
12 N1-SD	N1-SD				ANSTO	B2855	30200	179.5	9.6	5.3%	27750	164.9					
12 N1-Q3-B1	N1-Q3-B1				ANSTO	B2858	30200	863.8	17.8	2.1%	27750	793.7					
21 N1-Q3-B3	N1-Q3-B3				ANSTO	B3176	30200	459.7	12.8	2.8%	27750	422.4					
12 N1-Q3-015	N1-Q3-015				ANSTO	B2856	30200	173.6	8.9	5.1%	27750	159.5					
22 N1-Q3-030	N1-Q3-030				ANSTO	B3182	30200	181.3	14.2	7.8%	27750	166.6					
22 N1-Q3-070	N1-Q3-070				ANSTO	B3183	30200	183.0	9.2	5.0%	27750	168.1					
21 N1-Q3-090	N1-Q3-090				ANSTO	B3177	30200	181.8	6.7	3.7%	27750	167.1					
22 N1-Q3-140	N1-Q3-140				ANSTO	B3184	30200	219.5	9.4	4.3%	27750	201.7					
22 N1-Q3-190	N1-Q3-190				ANSTO	B3185	30200	221.9	7.4	3.3%	27750	203.9					
12 N1-Q3-210	N1-Q3-210				ANSTO	B2857	30200	251.2	10.0	4.0%	27750	230.8					
21 N1-Q2-B1	N1-Q2-B1				ANSTO	B3174	30200	1454.9	34.6	2.4%	27750	1336.9					
21 N1-Q2-B2	N1-Q2-B2				ANSTO	B3175	30200	2684.1	104.4	3.9%	27750	2466.4					
12 N1-Q2-DP	N1-Q2-DP	6.280	5.0%	0.314	ANSTO	B2859	30200	1568.6	23.0	1.5%	27750	1441.3	ANSTO	A1687	836.7	47.4	5.7%
18 N2-Q2-6B	N2-Q2-6	2.855	5.0%	0.143	ANSTO	B3157	30200	494.3	10.5	2.1%	27750	454.2	ANSTO	A1726	706.5	79.5	11.3%
21 N2-Q2-5	N2-Q2-5				ANSTO	B3173	30200	FAIL					ANSTO	A1735	FAIL		
18 N2-Q2-4	N2-Q2-4	2.563	5.0%	0.128	ANSTO	B3156	30200	243.6	12.2	5.0%	27750	223.9	ANSTO	A1725	299.0	37.4	12.5%
21 N2-Q2-3	N2-Q2-3				ANSTO	B3172	30200	FAIL					ANSTO	A1734	FAIL		
21 N2-Q2-2	N2-Q2-2				ANSTO	B3171	30200	242.5	11.5	4.7%	27750	222.8	ANSTO	A1733	305.5	30.1	9.9%
18 N2-Q2-1	N2-Q2-1	3.084	5.0%	0.154	ANSTO	B3155	30200	218.0	14.9	6.9%	27750	200.3	ANSTO	A1724	352.5	36.9	10.5%
23 N4-N-SD	N4-N-SD				ANSTO	B3416	30200	493.5	26.8	5.4%	27750	453.5					
23 N4-R-SD	N4-R-SD				ANSTO	B3418	30200	271.8	11.9	4.4%	27750	249.7					
23 N4-NR-SD	N4-NR-SD				ANSTO	B3417	30200	255.6	22.1	8.6%	27750	234.8					
18 P1-Q2-DP	P1-Q2-DP	10.523	5.0%	0.526	ANSTO	B3154	30200	2906.2	32.9	1.1%	27750	2670.4	ANSTO	A1723	450.7	44.0	9.8%
12 P1-Q1-DPS	P1-Q1-DPS	7.418	5.0%	0.371	ANSTO	B2860	30200	2178.0	28.2	1.3%	27750	2001.3	ANSTO	A1688	914.0	41.0	4.5%
23 P2-A3	MK3				ANSTO	B3419	30200	82.2	11.7	14.2%	27750	75.5	LLNL	AL12059	25.9	3.7	14.3%
18 P1-A2	MK2	4.018	5.0%	0.201	ANSTO	B3153	30200	152.1	7.8	5.1%	27750	139.8	ANSTO	A1721	10.0		0.0%
29A P1-A2	MK2*	4.018	0.050	0.201	LLNL	BE26330	28500	582.2	14.4	2.5%	28500	582.2	LLNL	AL12069	8.7	3.7	42.5%
18 P1-A1	MK1	2.744	5.0%	0.137	ANSTO	B3152	30200	29.6	8.2	27.8%	27750	27.2	ANSTO	A1722	10.0		0.0%
29A P1-A1	MK1*	2.744	0.050	0.137	LLNL	BE26329	28500	16.5	6.1	37.2%	28500	16.5	LLNL	AL12067	10.2	5.7	56.2%

Table 7c: Calculated concentrations, site production rates and "simple" exposure ages

1	2	39	40	41	42	43	44	45	46	47	48	49	50	51	52	53	54	55
SAMPLE ID	**ALIAS**		**10Be**			**26Al**		**LAT-ALT**	**CORRECTIONS**			**10Be**				**26Al**		
		CONC.	**ERR**	**ERR**	**CONC.**	**ERR**	**ERR**	**SCALING**	**DEPTH**	**THICK**	**PROD.**	**EXP AGE**	**INT**	**EXT**	**PROD.**	**EXP AGE**	**INT**	**EXT**
		N10		*σN10*	*N26*		*σN26*	*fla*	*fx*	*fh*	*P10*	*t10*	*σt10**	*σt10*	*P26*	*t26*	*σt26**	*σt26*
		[at/g]	**[%]**	**[at/g]**	**[at/g]**	**[%]**	**[at/g]**				**[at/g/y]**	**[Ma]**	**[Ma]**	**[Ma]**	**[at/g/y]**	**[Ma]**	**[Ma]**	**[Ma]**
24 N5-Na1-DP	NN	2.611E+06	2.5%	6.618E+04				0.833	1.000	0.987	3.766	0.855	0.027	0.111	25.574			
24 M1-WG3-DP	KK	2.442E+06	2.6%	6.262E+04				1.141	1.000	0.987	5.154	0.542	0.016	0.065	34.998			
24 M1-WG2-DP	KM	1.291E+06	4.2%	5.370E+04				1.155	1.000	0.987	5.218	0.264	0.012	0.031	35.433			
28 M1-ARI-DPQ	KZ	2.396E+06	2.7%	6.486E+04				1.133	1.000	0.987	5.119	0.535	0.017	0.064	34.762			
24 Z1-Na-DP	MZ	4.677E+06	2.8%	1.292E+05				1.042	1.000	0.987	4.708	1.385	0.056	0.211	31.972			
12 P1-Z1	MK	6.157E+06	2.3%	1.424E+05	1.414E+07	7.9%	1.122E+06	1.134	1.000	0.987	5.123	1.860	0.072	0.325	34.788	0.520	0.054	0.087
23 Y1-Nae-DPS	EY-R	3.012E+06	2.7%	8.081E+04				1.082	1.000	0.987	4.888	0.740	0.024	0.093	33.191			
23 Y1-Nae-DPN	EY	3.504E+06	3.3%	1.147E+05				1.085	1.000	0.987	4.899	0.890	0.037	0.119	33.268			
24 S2-Q1-DP	ES	5.115E+06	2.5%	1.281E+05				1.023	1.000	0.987	4.624	1.628	0.064	0.266	31.399			
24 H1-Nae-DP	EH	2.167E+06	2.5%	5.318E+04				1.106	1.000	0.987	4.999	0.490	0.014	0.057	33.946			
24 Z2-Nae-DP	EZ	6.099E+06	2.4%	1.484E+05				1.175	1.000	0.987	5.308	1.729	0.067	0.290	36.044			
PS-4-DP	PS4	6.349E+06	2.8%	1.762E+05				1.254	1.000	0.987	5.666	1.661	0.073	0.275	38.475			
PS-6-DP	PS6	7.252E+06	2.7%	1.974E+05				1.274	1.000	0.987	5.757	2.015	0.096	0.373	39.094			
19 PS-8	PS8	4.801E+06	3.1%	1.483E+05				1.189	1.000	0.987	5.371	1.193	0.051	0.173	36.474			
12 N1-SD	N1-SD	1.128E+05	5.7%	6.439E+03				0.888	1.000	0.971	3.937	0.029	0.002	0.003	26.733			
12 N1-Q3-B1	N1-Q3-B1	6.351E+05	2.9%	1.845E+04				0.890	1.000	0.956	3.897	0.170	0.005	0.019	26.464			
21 N1-Q3-B3	N1-Q3-B3	3.354E+05	3.5%	1.161E+04				0.890	1.000	0.956	3.897	0.088	0.003	0.010	26.461			
12 N1-Q3-015	N1-Q3-015	1.178E+05	5.5%	6.474E+03				0.890	0.942	0.915	3.512				23.850			
22 N1-Q3-030	N1-Q3-030	1.120E+05	8.1%	9.074E+03				0.890	0.787	0.889	2.850				19.353			
22 N1-Q3-070	N1-Q3-070	1.117E+05	5.4%	6.080E+03				0.890	0.487	0.889	1.764				11.975			
21 N1-Q3-090	N1-Q3-090	1.108E+05	4.2%	4.648E+03				0.890	0.383	0.840	1.310				8.898			
22 N1-Q3-140	N1-Q3-140	1.153E+05	4.7%	5.463E+03				0.890	0.210	0.889	0.761				5.170			
22 N1-Q3-190	N1-Q3-190	1.160E+05	3.9%	4.528E+03				0.890	0.115	0.889	0.418				2.837			
12 N1-Q3-210	N1-Q3-210	1.188E+05	4.5%	5.303E+03				0.890	0.091	0.889	0.329				2.232			
21 N1-Q2-B1	N1-Q2-B1	1.067E+06	3.1%	3.353E+04				0.894	1.000	0.956	3.909	0.294	0.010	0.033	26.542			
21 N1-Q2-B2	N1-Q2-B2	1.952E+06	4.4%	8.584E+04				0.894	1.000	0.956	3.909	0.576	0.029	0.073	26.542			
12 N1-Q2-DP	N1-Q2-DP	1.081E+06	2.5%	2.722E+04	5.150E+06	7.8%	4.028E+05	0.894	1.000	0.987	4.037	0.288	0.008	0.032	27.416	0.208	0.018	0.029
18 N2-Q2-6B	N2-Q2-6	3.614E+05	2.9%	1.066E+04	2.110E+06	12.5%	2.632E+05	0.894	0.369	0.942	1.421				9.648			
21 N2-Q2-5	N2-Q2-5							0.894	0.071	0.942	0.275				1.864			
18 N2-Q2-4	N2-Q2-4	1.479E+05	5.4%	8.026E+03	7.534E+05	13.6%	1.026E+05	0.894	0.025	0.942	0.098				0.664			
21 N2-Q2-3	N2-Q2-3							0.894	0.007	0.942	0.028				0.193			
21 N2-Q2-2	N2-Q2-2	1.474E+05	5.2%	7.612E+03				0.894	0.004	0.942	0.014				0.094			
18 N2-Q2-1	N2-Q2-1	1.330E+05	7.2%	9.508E+03	9.498E+05	11.8%	1.120E+05	0.894	0.002	0.942	0.007				0.045			
23 N4-N-SD	N4-N-SD	3.063E+05	5.8%	1.778E+04				1.158	1.000	0.971	5.113	0.061	0.004	0.007	34.716			
23 N4-R-SD	N4-R-SD	1.647E+05	4.8%	7.964E+03				1.145	1.000	0.971	5.087	0.033	0.002	0.004	34.540			
23 N4-NR-SD	N4-NR-SD	1.563E+05	8.9%	1.386E+04				1.136	1.000	0.971	4.876	0.032	0.003	0.004	33.108			
18 P1-Q2-DP	P1-Q2-DP	1.853E+06	2.3%	4.340E+04	4.567E+06	11.1%	5.090E+05	1.041	1.000	0.987	4.704	0.440	0.012	0.051	31.942	0.154	0.019	0.025
12 P1-Q1-DPS	P1-Q1-DPS	1.504E+06	2.4%	3.647E+04	6.087E+06	7.0%	4.266E+05	1.050	1.000	0.987	4.745	0.346	0.009	0.039	32.218	0.209	0.016	0.028
23 P2-A3	MK3	4.298E+04	14.3%	6.158E+03				1.093	0.000	0.915	0.000				0.000			
18 P1-A2	MK2	7.456E+04	5.5%	4.105E+03	3.882E+04	5.4%	2.092E+03	1.080	0.000	0.915	0.000				0.000			
29A P1-A2	MK2*	2.287E+05	3.2%	7.395E+03	2.738E+04	42.8%	1.173E+04	1.080	0.000	0.915	0.000				0.000			
18 P1-A1	MK1	1.462E+04	27.8%	4.072E+03	2.661E+04	5.4%	1.434E+03	1.077	0.000	0.915	0.000				0.000			
29A P1-A1	MK1*	6.316E+03	37.2%	2.351E+03	2.580E+04	56.4%	1.456E+04	1.077	0.000	0.915	0.000				0.000			

Constants used in calculations in table 7:

1. **^{10}Be half-life:** *t1/2(10)* = (1.36E+06 ± 7.00E+04) y
2. **^{10}Be decay constant:** $\lambda 10$ = (5.10E-07 ± 2.623E-08) y^{-1}

   $\lambda = \ln(2) / t_{1/2}$, $\sigma_\lambda = \sqrt{\left(-\ln(2) / (t_{1/2})^2\right)^2 \cdot \sigma_{t_{1/2}}^2}$
3. **^{10}Be production rate at SLHL:** *P10** = (4.580 ± 0.458) atoms g^{-1} y^{-1}
4. **Concentration of Be carrier:** *cbe* = (980 ± 3) ppm
5. **Atomic mass of Be:** *M(Be)* = 9.012 g mol^{-1}. Uncertainty is negligible
6. **AMS reproducibility of the Be SRM:** *srmbe* = 2%
7. **^{26}Al half-life:** *t1/2(26)* = (7.01E+05 ± 1.963E+04) y
8. **^{26}Al decay constant:** $\lambda 26$ = (9.89E-07 ± 2.769E-08) y^{-1} (propagated as in 2)
9. **^{26}Al production rate at SLHL:** *P26** = (31.10 ± 3.110) atoms g^{-1} y^{-1}
10. **Atomic mass of Al:** *M(Al)* = 26.982 g mol^{-1}. Uncertainty is negligible
11. **AMS reproducibility of the Al SRM:** *srmal* = 2%
12. **Avogadro's number:** *NA* = 6.022E+23 atoms mol^{-1}. Uncertainty is negligible
13. **Analytic weight error:** *we* = 0.001 g
14. **Attenuation length:** Λ = (150 ± 4) g cm^{-2}

Field data

1. **Sample ID**. A unique identifier, referring to the initial name of the sample as given in the field. Sample bags, notebook entries, and all holders of processed material in the various labs have this identifier.
2. **Alias.** A shorter and friendlier acronym for the sample's name, appearing on the various maps and referred to in the text.
3. **Ord.** Reflects the natural order in which the sample has been processed (relative to other samples) in the cosmogenic lab of the Hebrew University during this work.
4. **Type.** Either of the following:

   D(esert) P(avement) on an abandoned terrace (wind gap / inset terrace)
   Boulder on an abandoned terrace
   Cosmogenic depth profile (either of an inset terrace or a windgap)
   Active stream sediment
5. **Lithology.** Description of the source rock from which the sample has been prepared.
6. **Basin.** Geographical reference to the nearest major stream.
7. **ITM East: [m].** The "Easting" coordinate of the sampling location on the Israeli Transverse Mercator (ITM) reference grid.
8. **ITM North: [m].** The "Northing" coordinate on ITM.
9. **Lon [decimal degrees].** Longitude of the sampled site.
10. **Lat: *lat* [decimal degrees].** Latitude of the sampled site.
11. **Alt: *z* [m above sea level].** Current elevation of the sampled site.
12. **Depth: *x* [m].** Depth of the sampled material below the ground.
13. **Density: ρ [g cm^{-3}].** The estimated density of the sampled material.
14. **Sample thickness: *h* [cm].** The thickness of the sample.
15. **Topographic shielding: *ft*.** A unitless factor accounting for the obstruction of the cosmic flux at the given site by the surrounding topography. Calculated using the relief shadow modeling technique (Codilean, 2000), using a 25x25 m cell DTM.

16. **Distance: *l* [km]**. For the regional set of samples, the site's distance from the Quaternary tilt axis of the Negev.

Lab data

17. **Sample mass: *ws* [g].** The weight of the purified quartz sample prior to its dissolution in HF acid.
18. **Be carrier mass: *wcbe* [g].** The weight of the 9Be spike added to all samples.
19. **Al carrier mass: *wcal* [g].** The weight of the Al spike added to samples which had low contents of native Aluminum.
20. **Diluted sample: *ws'* [g].** The cumulative weight of the quartz sample and the HF acid in which it has been dissolved.
21. **Aliquot mass: *wa* [g].** The weight of the aliquot taken out of the dissolved quartz sample.
22. **Diluted aliquot: *wa'* [g].** The weight of the dried and diluted aliquot prior to its measurement in ICP-AES.
23. **Total Al measurement: *al* [ppm].** The concentration of Al in the diluted aliquot as measured by ICP-AES.
24. **Total Al relative error: [%].** Relative error of the ICP-AES concentration reading.
25. **Total Al absolute error: *σal* [ppm].** Absolute error of the ICP-AES concentration reading.

AMS data

26. **Lab name.** The AMS facility where 10Be of this sample was run.
27. **Cathode ID.** Internal code of the AMS facility identifying the exact sample run.
28. **Reference standard: *std* [10^{-12}].** The nominal concentration of 10Be in the Standard Reference Material (SRM) as accepted and reported by the lab during the time when the measurement was performed.
29. **Measured ^{10}Be/^{9}Be ratio: *R1* [10^{-15}].** The isotopic ratio of 10Be/9Be as counted and returned by the AMS.
30. **Measured ^{10}Be/^{9}Be absolute error: *σR1* [10^{-15}].** The reported absolute instrumental error of the AMS regarding this measurement.
31. **Measured ^{10}Be/^{9}Be relative error: *σR1 / R1* [%].** The relative uncertainty of the reported ratio.
32. **New standard: *std'* [10^{-12}].** Re-evaluated nominal concentration of 10Be in the SRM (see Nishiizumi et al., 2007; Fink and Smith, 2007)
33. **Recalculated ^{10}Be/^{9}Be ratio: *R1'* [10^{-15}].** The measured isotopic ratio corrected for the presently accepted nominal concentration of 10Be in the SRM, via the relation:
    $R1' = std' / std \times R1$
    where
    R1 [10^{-15}] is the recalculated isotopic ratio (column 29)
    std [10^{-12}] is the reported nominal 10Be conc. in the SRM (column 28)
    std' [10^{-12}] is the recalibrated nominal 10Be conc. in the SRM (column 32)
34. **Lab name.** The AMS facility where 26Al of this sample was run.
35. **Cathode ID.** Internal code of the AMS facility identifying the exact sample run.
36. **Measured ^{26}Al/^{27}Al ratio: *R2* [10^{-15}].** The isotopic ratio of 26Al/27Al as counted and reported by the AMS.

37. **Measured $^{26}Al/^{27}Al$ absolute error: *σR2* [10^{-15}].** The reported absolute instrumental error of the AMS regarding this measurement.

38. **Measured $^{26}Al/^{27}Al$ relative error: *σR2 / R2* [%].** The relative uncertainty of the reported ratio.

Concentrations and exposure ages:

39. **^{10}Be concentration: *N10* [atoms g^{-1}].** The concentration of 10Be per gram of sample, based on the relationship (Gosse and Phillips, 2001):

$$N9 = cbe \cdot wcbe / M(Be) \cdot NA;\ N10 = N9 \cdot R1' / ws$$

$$N10 = cbe \cdot wcbe / M(Be) \cdot NA \cdot R1' / ws$$

where
cbe [ppm] is the conc. of Be in the spike (constant 4 multiplied by 10^{-6})
wcbe [g] is the weight of the spike added to the sample (column 18)
M(Be) [g mol^{-1}] is the atomic mass of Be (constant 5)
NA [atoms mol^{-1}] is avogadro's number (constant 12)
R1' [10^{-15}] is the recalculated isotopic ratio (column 33 multiplied by 10^{-15})
ws [g] is the initial weight of the processed quartz sample (column 17)

40. **^{10}Be concentration relative error: *σN10 / N10* [%].** The propagated relative uncertainty of the 10Be concentration in sample:

$$\frac{\sigma N10}{N10} = \sqrt{\frac{we^2}{ws^2} + \frac{we^2}{wcbe^2} + \frac{\sigma cbe^2}{cbe^2} + \left(\frac{\sigma R1}{R1}\right)^2 + srmbe^2}$$

where
we [g] is the uncertainty in the analytical weight (constant 13)
ws [g] is the initial weight of the processed quartz sample (column 17)
wcbe [g] is the weight of the spike added to the sample (column 18)
cbe and *σcbe* [ppm] are the Be spike conc. value and uncertainty (constant 4)
σR1/R1 [%] is the relative uncertainty of the measured isotopic ratio (column 31)
srmbe [%] is the reproducibility error of the 10Be SRM (constant 6)

41. **^{10}Be concentration absolute error: *σN10* [atoms g^{-1}].** The product of columns 39 and 40.

42. **^{26}Al concentration: *N26* [atoms g^{-1}].** The concentration of 26Al per gram of sample, based on the relationship (Gosse and Phillips, 2001):

$$N27 = al \cdot (ws' / ws) \cdot (wa' / wa) / M(Al) \cdot ws \cdot NA;\ N26 = N27 \cdot R2 / ws$$

$$N26 = al \cdot (ws' / ws) \cdot (wa' / wa) / M(Al) \cdot NA \cdot R2$$

where
al [ppm] is the aluminum conc. in the aliquot measured by ICP (column 23 multiplied by 10^{-6})
ws [g] is the initial weight of the processed quartz sample (column 17)
ws' [g] is the weight of the quartz sample dissolved in HF acid (column 20)
wa [g] is the weight of the extracted aliquot (column 21)
wa' [g] is the weight of the diluted aliquot (column 22)
M(Al) [g mol^{-1}] is the atomic mass of Al (constant 10)
NA [atoms mol^{-1}] is avogadro's number (constant 12)
R2 [10^{-15}] is the measured isotopic ratio (column 36 multiplied by 10^{-15})

43. **^{26}Al concentration relative error: *σN26 / N26* [%].** The propagated relative uncertainty of the 26Al concentration in sample:

$$\frac{\sigma N26}{N26} = \sqrt{\frac{\sigma al^2}{al^2} + \frac{we^2}{ws^2} + \left(\frac{we^2}{wcal^2}\right) + \frac{we^2}{ws'^2} + \frac{we^2}{wa^2} + \frac{we^2}{wa'^2} + \left(\frac{\sigma R2}{R2}\right)^2 + srmal^2}$$

where

al and *σal* [ppm] are the aluminum conc. in the aliquot and its analytical uncertainty (columns 23 and 25)

we [g] is the uncertainty in the analytical weight (constant 13)

ws [g] is the initial weight of the processed quartz sample (column 17)

wcal [g] is the weight of the spike added to the sample. This term is omitted if no spike was added (column 19)

ws' [g] is the weight of the quartz sample dissolved in HF acid (column 20)

wa [g] is the weight of the extracted aliquot (column 21)

wa' [g] is the weight of the diluted aliquot (column 22)

σR2/R2 [%] is the relative uncertainty of the measured isotopic ratio (column 38)

srmal [%] is the reproducibility error of the 10Be SRM (constant 11)

44. **^{26}Al concentration absolute error: *σN26* [atoms g^{-1}].** The product of columns 42 and 43.

45. **Latitude-altitude scaling: *fla*.** A unitless scaling factor which is a function of latitude (*lat* [dec. deg.], column 10) and altitude (*z* [masl], column 11). Calculated following Stone (2000).

46. **Correction for depth: *fx*.** A unitless correction factor for samples collected below the ground, following the relation (Lal, 1991):

$$fx = \exp(-\rho x / \Lambda)$$

where

ρ [g cm^{-3}] is the density of the material above the sample (column 13)

x [m] is the depth of the sample below ground (column 12, multiplied by 100 to convert to centimeters)

Λ [g cm^{-2}] is the attenuation length of cosmic rays (constant 14)

47. **Correction for thickness: *fh*.** A unitless correction factor for sample thickness, following the relation (Gosse and Phillips, 2001):

$$fh = \Lambda / \rho h \cdot (1 - \exp(-\rho h / \Lambda))$$

where

Λ [g cm^{-2}] is the attenuation length of cosmic rays (constant 14)

h [cm] is the sample thickness (column 14)

ρ [g cm^{-3}] is the density of the material (column 13)

48. **^{10}Be in-situ production rate: *P10* [atoms g^{-1} y^{-1}].** The in-situ production rate is calculated as follows: (Gosse and Phillips, 2001)

$$P10 = ft \cdot fla \cdot fx \cdot fh \cdot P10^*$$

where

*P10** is the production rate of 10Be at Sea Level High Latitude (constant 3)

ft is the topographic shielding factor (column 15)

fla is the latitude-altitude scaling factor (column 45)

fx is the correction factor for sample depth beneath ground (column 46)

fh is the correction factor for sample thickness (column 47)

49. **^{10}Be "simple" exposure age: *t10* [Ma].** A "simple" exposure age (assuming no erosion and no uplift) is given by $t(\lambda, N, P) = -\lambda^{-1} \ln(1 - \lambda N / P)$ (Lal, 1991). Substituting the relevant values yields:

$$t10 = -\lambda 10^{-1} \ln(1 - \lambda 10 \cdot N10 / P10)$$

where
$\lambda 10$ [y^{-1}] is the decay constant of 10Be (constant 2)
$N10$ [atoms g^{-1}] is the concentration of 10Be per gram of sample (column 39)
$P10$ [atoms g^{-1} y^{-1}] is the in-situ production rate of 10Be (column 48)

50. **^{10}Be "simple" exposure age internal error: $\sigma t10^*$ [Ma].** See below

51. **^{10}Be "simple" exposure age external error: $\sigma t10$ [Ma].**
Given the function $t(\lambda, N, P) = -\lambda^{-1} \ln(1 - \lambda N / P)$, the actual observed values $\lambda \pm \sigma\lambda$, $N \pm \sigma N$, $P \pm \sigma P$, and assuming that the uncertainties of these values are independent one of another, the uncertainty σt may be expressed via the partial derivatives of t as follows (modified from Gosse and Phillips, 2001, where the derivation contains a typo):

$$\sigma_t(\lambda, \sigma\lambda, N, \sigma N, P, \sigma P) =$$

$$\left(\frac{N}{\lambda P(1-\lambda N/P)} + \frac{\ln(1-\lambda N/P)}{\lambda^2}\right)^2 \sigma_\lambda^2$$

$$+\left(\frac{1}{P(1-\lambda N/P)}\right)^2 \sigma_N^2 + \left(\frac{-N}{P^2(1-\lambda N/P)}\right)^2 \sigma_P^2$$

Since "internal" error accounts for instrumental uncertainty only (Balco et al., 2008), the terms relating to uncertainties regarding the nuclide's half-life and the production rate appear only in the "external" uncertainty, used for comparing the sample's age to other geochronometers:

$$\sigma t10^* = \sigma_t(\lambda 10, 0, N, \sigma N10, P, 0)$$

$$\sigma t10 = \sigma_t(\lambda 10, \sigma\lambda 10, N, \sigma N10, P, (\sigma P10^*/P10^*))$$

where
$\lambda 10$ [y^{-1}] and $\sigma\lambda 10$ [y^{-1}] are the decay constant of 10Be and its absolute uncertainty (constant 2)
$N10$ [atoms g^{-1}] and $\sigma N10$ [atoms g^{-1}] are the concentration of 10Be per gram of sample and its absolute uncertainty (columns 39 and 41, respectively)
$P10$ [atoms g^{-1} y^{-1}] is the in-situ production rate of 10Be (column 48)
$P10^*$ and $\sigma P10^*$ [atoms g^{-1} y^{-1}] are the SLHL production rate and its absolute uncertainty (constant 3)

52. **^{26}Al in-situ production rate: $P26$ [atoms g^{-1} y^{-1}].** (See discussion in column 49.)
$$P26 = ft \cdot fla \cdot fx \cdot fh \cdot P26^*$$
where
$P26^*$ is the production rate of 26Al at Sea Level High Latitude (constant 9)
ft is the topographic shielding factor (column 15)
fla is the latitude-altitude scaling factor (column 45)
fx is the correction factor for sample depth beneath ground (column 46)
fh is the correction factor for sample thickness (column 47)

53. **^{26}Al "simple" exposure age: $t26$ [Ma].** (See discussion in column 50.)
$$t26 = -\lambda 26^{-1} \ln(1 - \lambda 26 \cdot N26 / P26)$$
where
$\lambda 26$ [y^{-1}] is the decay constant of 26Al (constant 8)
$N26$ [atoms g^{-1}] is the concentration of 26Al per gram of sample (column 42)
$P26$ [atoms g^{-1} y^{-1}] is the in-situ production rate of 26Al (column 52)

54. **^{26}Al "simple" exposure age internal error: σt26* [Ma].** See column 51

55. **^{26}Al "simple" exposure age external error: σt26 [Ma].** See column 51

$$\sigma t26 = \sigma_t\left(\lambda 26, 0, N, \sigma N26, P, 0\right)$$

$$\sigma t26^* = \sigma_t\left(\lambda 26, \sigma\lambda 26, N, \sigma N26, P, \left(\sigma P26^*/P26^*\right)\right)$$

where

λ26 [y^{-1}] and *σλ26* [y^{-1}] are the decay constant of 26Al and its absolute uncertainty (constant 8)

N26 [atoms g^{-1}] and *σN26* [atoms g^{-1}] are the concentration of 26Al per gram of sample and its absolute uncertainty (columns 42 and 44, respectively)

P26 [atoms g^{-1} y^{-1}] is the in-situ production rate of 26Al (column 52)

*P26** and *σP26** [atoms g^{-1} y^{-1}] are the SLHL production rate and its absolute uncertainty (constant 9)

8.2. Derivation of the basic cosmogenic equations

As of 2009, the lack of a structured textbook on the use of cosmogenic isotopes in geomorphology makes the peer-reviewed journals to be the primary source of information regarding basic methods of calculation. Frequently encountered typos, mistakes, and ambiguous or definition of variables across different papers have led me to write the following chapter, which is an attempt to systematically explain and derive the basic equations related to (i) modeling of the cosmic flux and (ii) quantifying the exposure time with regard to effects of erosion and uplift.

The production rate of cosmogenic nuclides

As radiation penetrates through matter, its intensity decreases due to interactions with particles in the traversed medium. A law discovered by Bouguer in 1729, and studied later by Lambert and Beer (Curtis, 1978), relates the radiant power in a beam of electromagnetic radiation, usually ordinary light, to the length of the path of the beam in an absorbing medium and to the concentration of the absorbing species, respectively (Swinehart, 1962). Lambert's law states that the fraction of radiant power absorbed ($-dP/P$) when it passes through an infinitesimal thickness of the absorbing medium (dx) is proportional to the infinitesimal thickness, i.e., $-dP / P = a_1 \cdot dx$, where a_1 is an arbitrary constant. Beer's law states that the fractional loss of power due to absorption when an infinitesimal increase is made in the concentration (dc) is proportional to that infinitesimal increase. In general this proportionality "constant" is a linear function of the length of the light path in the solution (b), thus $-dP / P = a_2 \cdot b \cdot dc$.

The combined solution of the two differential equations is known as the Bouguer-Beer-Lambert law, and is usually written as:

$$P(b) = P(0) \cdot \exp(-abc) \tag{14}$$

where a is the so-called "absorptivity" constant, b is the path length traversed by the radiant power and c is concentration of the absorbing species (taken to be uniform throughout the medium). While cosmic-rays of interest to cosmogenic studies consist of subatomic particles, their attenuation is similar to that of light. The rate of reaction of cosmic-ray particles with the medium through which the beam passes depends on the number of nucleons (protons and neutrons) in the medium per unit path length, regardless of the actual elemental composition

or atomic structure (Gosse and Phillips, 2001). The cumulative mass traversed by a cosmic-ray beam is given by:

$$D(x) = \int_0^x \rho(x)dx \tag{15}$$

where x is ordinary linear distance, $\rho(x)$ is the medium's local density at x and $D(x)$ is the so-called atmospheric or rock "depth" (g cm^{-2}), i.e., the medium's density integrated over a straight path. For this matter, an atmospheric column immediately above sealevel of a 1.5 km height has roughly the same "depth" as 60 cm of a typical rock, since both contain roughly the same number of nucleons per unit area.

The attenuation of the cosmic-ray intensity with "depth" is directly proportional to the intensity of the incipient radiation:

$$\frac{dP}{dD} = \frac{P}{\Lambda} \tag{16}$$

where P is the cosmic-ray intensity (particles cm^{-2} s^{-1} or as integrated over time to resultant atoms g^{-1} y^{-1}) and Λ is the so-called "attenuation length" (g cm^{-2}), the cumulative mass traversed that is required to attenuate the intensity by a factor of e^{-1}. The solution of the differential equation is:

$$P(x) = P(0) \cdot \exp\left(-\frac{D(x)}{\Lambda}\right) \tag{17}$$

(Gosse and Phillips, 2001). In a homogenous media where density can be taken to be constant (e.g., rock or soil), the medium's "depth" $D(x)$ is a linear function of distance, such as:

$$P(x) = P(0) \cdot \exp\left(-\frac{\rho x}{\Lambda}\right) \tag{18}$$

In a non-homogenous media (e.g., the atmosphere), $D(x)$ must be further evaluated as discussed below. The hydrostatic balance $\partial\overline{p} / \partial z = -g\rho$ assumes that the atmospheric pressure gradient (i.e., the decrease of pressure with increasing height to a negligible value at ca. 20 km) is proportional to the air density via the gravity constant (g). Expressing the air density using the ideal gas state law ($\rho = n / V = \overline{p} / RT$) and integrating the hydrostatic equation with the aforesaid substitution, gives an expression for pressure $\overline{p}(z)$ as a function of elevation (assuming an isothermal atmosphere):

$$\overline{p}(z) = \overline{p}(0) \cdot \exp\left(-\frac{z}{H}\right) \tag{19}$$

where $H = RT / g$ is the "scale height", i.e., distance after which the pressure drops by a factor of e^{-1} of its initial value. To get the "depth" (mass per unit area) of the entire atmospheric column above elevation z, the hydrostatic equation can be rearranged to yield:

$$D(z) = \int_z^\infty \rho \partial z = \frac{p(z)}{g} = \frac{\overline{p}(0)}{g} \exp\left(-\frac{z}{H}\right) \tag{20}$$

This expression of $D(z)$ may be substituted back into Equation (17) to yield:

$$P(z) = P(0) \cdot \exp\left(\frac{\overline{p}(0)}{\Lambda g} \exp\left(\frac{z}{H}\right)\right) \tag{21}$$

While analytically correct, the final formula in (21) is cumbersome. The inner exponent can be avoided by choosing an altitude range where the atmospheric depth changes linearly with elevation, i.e., $D(z) \sim z$. Then, Equation (21) may be simplified to either of the equations

$$P(z) = P(0) \cdot \exp\left(-Mz\right) \tag{22}$$

$$P(D) = P(0) \cdot \exp\left(-M'D\right) \tag{23}$$

(Lal, 1991; Brown, 1991), where M and M' are given by

$$M = \frac{\partial P}{P \cdot \partial z}; M' = \frac{\partial P}{P \cdot \partial D} \tag{24}$$

i.e., the "scale height" and "scale depth" which attenuate the rays by a factor of e^{-1}. In the atmosphere, M^{-1} is of the order of 1–2 km for elevations below 5 km (Lal, 1991). We will hereby use Lal's formulation (Equation 22) because it is more straightforward to discuss uplift and subsidence rates in m Ma^{-1} rather than in g cm^{-2} Ma^{-1}. A similar attenuation coefficient may be also defined for rock:

$$\mu = \frac{\partial P}{P \cdot \partial x} \tag{25}$$

being equal to the constant ρ / Λ. μ^{-1} is of the order of 60 cm for a typical rock. The production rate at a fixed geomagnetic latitude may then be described by the following equations:

$$\begin{aligned} P(z) &= P(z_0)\, e^{Mz};\ e^{Mz_0} \equiv 1 \\ P(x) &= P(x_0) e^{-\mu x};\ e^{-\mu x_0} \equiv 1 \end{aligned} \tag{26}$$

Usually, both z_0 and x_0 are set to 0, i.e., the production functions are scaled to sealevel and the top surface respectively. However, for equations considering elevation changes, z_0 is the initial elevation of the surface which underwent tectonic perturbation. From $x_0 = 0$, it follows

that $P(z, x_0) \equiv P(z)$, and we can express the production rate as a function of both regional elevation and rock depth:

$$P(z, x) = P(z_0) e^{Mz - \mu x} \tag{27}$$

Cosmogenic nuclide build-up

The discovery of radioactivity by Becquerel in 1896 marked the beginning of nuclear age. Soon after, Rutherford (1900) introduced the concept of a half-life of an unstable isotope, measuring it to a high precision for ^{220}Rn (originally referred to as "Thorium emanation") by an electrical circuit. Having noticed that "the intensity of the radiation given out by the radioactive particles falls off in a geometrical progression with the time", he conducted a verifying experiment, in which he let the decaying ^{220}Rn to reach a steady state by placing its radioactive parent ^{224}Ra close nearby (originally referred to as a "Thorium compound"). Defining N as the number of radioactive ions, and P as the number of radioactive ions supplied per second, Rutherford (1900) expressed the rate of change in radioactivity as $dN / dt = P - \lambda N$, which has the solution:

$$N = \frac{P}{\lambda}\left(1 - e^{-\lambda t}\right) \tag{28}$$

Rutherford and Soddy (1902) explain that Equation (28) expresses "the rise of activity to a constant maximum of a system consisting of radiating particles in which (1) the rate of supply of fresh radiating particles is constant and (2) the activity of each particle dies down geometrically with the time [...]". It is noteworthy that this equation is used today in cosmogenic research in the same form as it was stated in Rutherford's 1900 paper.

Our formulation of the geomorphological problem follows that of Cerling and Craig (1994): a geomorphic surface, fixed in geomagnetic coordinates on the Earth's surface is bombarded by the incident cosmic radiation, creating new (in-situ) isotopes, both stable and radioactive, by an exponentially attenuated flux both in the atmosphere and in the substrate of the surface. Describing the concentration as a function of time leads to a "double-moving-boundary problem", since (a) the surface is undergoing local erosion or deposition, and (b) the surface is subject to regional tectonic motion, experiencing large-scale elevation changes. Assuming a constant uplift (U, negative for subsidence) and erosion (ε, negative for sedimentation) rates (m Ma^{-1}) over a given period of time, one can express the "moving boundaries" as linear functions of time (t), so that:

$$\begin{aligned} z(t) &= z_0 + Ut \\ x(t) &= x_0 - \varepsilon t \end{aligned} \tag{29}$$

A geological process where either the erosion or uplift rate changes with time should be split to sub-periods wherein they can be taken constant. The derivation of the cosmogenic concentration as a function of time, erosion and uplift is (after Cerling and Craig, 1986):

$$\frac{dN(t)}{dt} = P(z(t), x(t)) - \lambda N(t)$$

$$N(t) = e^{\int -\lambda dt}\left(\int e^{\int \lambda dt} P(z_0, x_0) e^{M(z_0+Ut)} e^{-\mu(x_0 \varepsilon t)} dt + c\right)$$

$$= ce^{-\lambda t} + P(z_0, x_0)\cdot e^{-\lambda t}\int e^{(\lambda+MU+\mu\varepsilon)t} dt = ce^{-\lambda t} + \frac{P(z_0, x_0)\cdot e^{-\lambda t}}{\lambda + MU + \mu\varepsilon}\left[e^{(\lambda+MU+\mu\varepsilon)t}\right]_0^t$$

Setting the boundary condition $c = N_{inh}$ (the inherited concentration from previous exposure history) leads to the "master equation"

$$N(t) = N_{inh}\cdot e^{-\lambda t} + \frac{P(z_0, x_0)\cdot e^{-\lambda t}}{\lambda + MU + \mu\varepsilon}\left(e^{(\lambda+MU+\mu\varepsilon)t} - 1\right) \tag{30}$$

from which many familiar equations describing erosion (Lal, 1991), deposition (Lal and Arnold, 1985), uplift (Brown, 1991) and combinations thereof (Brook et al., 1994) may be easily derived (Equations 41 – 44). Below we will, however, focus on an earlier formulation by Cerling and Craig (1986), which expresses the in-situ cosmogenic nuclide concentration as a function of the current production rate at surface (P), and the effective mean life (T), defined as:

$$T = \left(\lambda + \delta\right)^{-1} \tag{31}$$

(Cerling and Craig, 1986; Lal, 1991), where δ is the *combined effect of tectonic and surficial processes* on the nuclide's mean life value:

$$\delta = MU + \mu\varepsilon \tag{32}$$

U may represent uplift ($U > 0$), subsidence ($U < 0$) or tectonic quiescence ($U = 0$), while ε similarly represents erosion ($\varepsilon > 0$), sedimentation ($\varepsilon < 0$) or an absence of local surficial processes ($\varepsilon = 0$). Combining Equations (30), (31) and (32) we get:

$$N(z,x,t) = N_{inh}\cdot e^{-\lambda t} + P(z_0, x_0)\cdot e^{-\lambda t}\cdot T\left(e^{t/T} - 1\right)$$

$$= N_{inh}\cdot e^{-\lambda t} + P(z_0, x_0)\cdot e^{-\lambda t}\cdot e^{(\lambda+MU+\mu\varepsilon)t}\cdot e^{Mz_0 - \mu x_0}\cdot T\left(1 - e^{-t/T}\right)$$

$$= N_{inh}\cdot e^{-\lambda t} + P(z_0, x_0)\cdot e^{Mz(t) - \mu x(t)}\cdot T\left(1 - e^{-t/T}\right)$$

$$N(z,x,t) = N_{inh}\cdot e^{-\lambda t} + P(z(t), x(t))\cdot T\left(1 - e^{-t/T}\right)$$

Assuming that the inheritance from previous exposure histories is insignificant ($N_{inh}\cdot e^{-\lambda t} = 0$), we can rearrange the last equation to *separate all knowns from the unknowns*:

$$N / P = T\left(1 - \exp\left(-t / T\right)\right) \tag{33}$$

or even more explicitly:

$$N/P=\left(\lambda+\delta\right)^{-1}\left(1-\exp\left(\frac{-t}{\left(\lambda+\delta\right)^{-1}}\right)\right) \tag{34}$$

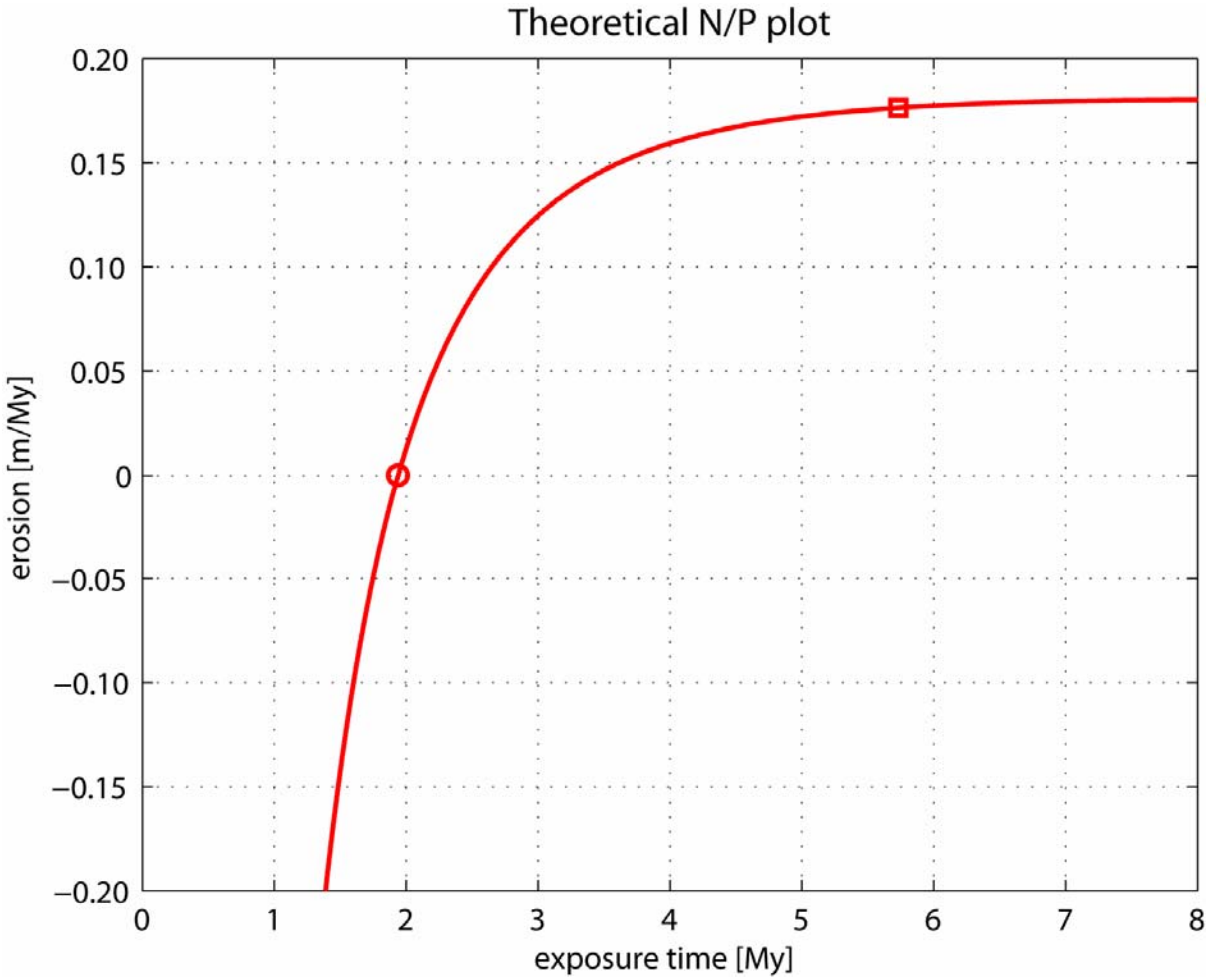

Figure 29: Theoretical N/P plot.
The N/P ratio of a sample from any surface which was exposed for 2My at latitude 30º experiencing zero tectonics and erosion will fall on this curve, invariant of the surface's current elevation or the sample's depth. For convenience, δ is expressed in units of erosion ($U=0;\varepsilon=\mu^{-1}\delta$). Circle represents "simple exposure age" (intersection with $\delta=0$, see text). Square represents maximum time for exposure-age dating (95% of steady-state ratio). The upper limit of erosion in given by $\delta_{sat}=P/N-\lambda$ (see text), being equal here to ~0.2 m/My.

where t and δ are the unknowns. N, the measured in-situ cosmogenic concentration, is usually measured in AMS within a <5% error, while the uncertainty in the estimated in-situ production rate P is ~10% (Lal, 1991). Since production rates are calibrated based on in-situ concentration measurements (Nishiizumi et al., 1989), the uncertainties cannot be treated as independent and the total uncertainty of the N/P ratio rises to ~15%. The N/P ratio represents the *concentration scaled to production rate*. This means that the N/P ratio is independent of elevation and soil depth. If surfaces at different elevations (including horizons below these surfaces) have been exposed for the same amount of time (t) and experienced

similar tectonic and surficial processes (δ), they all will possess the same N/P ratio regardless of their current elevation and depth below ground (Figure 29).

Similar to the concentration in Equation (28), the ratio N/P reaches a saturation value at $t \to \infty$, more specifically:

$$\left(N/P\right)_{sat} = \left(\lambda + \delta\right)^{-1} = T \tag{35}$$

i.e., the nuclide's effective mean life. Solving Equation (34) for t, we can get an expression of the exposure age as a function of the other unknown, δ:

$$t = -\left(\lambda + \delta\right)^{-1} \ln\left(1 - \frac{N/P}{\left(\lambda + \delta\right)^{-1}}\right) \tag{36}$$

At this stage, two straightforward interpretations are usually made. The first is to assume a lack of tectonic and surficial processes ($\delta = 0$), and solve Equation (36) to get the "simple exposure age":

$$t_s = -\lambda^{-1} \ln\left(1 - \frac{N/P}{\lambda^{-1}}\right) \tag{37}$$

For Equation (36) to be valid, the expression inside the logarithm must be positive. It means that the assumed saturation ratio $\left(N/P\right)_{sat}$ in Equation (35) (which is a function of δ) must be greater than the observed N/P ratio, otherwise we make a violation to the steady state equilibrium law (equation 28). The upper-limit of δ in Equation (36) is hence:

$$\delta < \frac{1}{N/P} - \lambda \tag{38}$$

More realistically, the steady-state equilibrium is reached at $\delta = \frac{0.95}{N/P} - \lambda$, and any greater value of δ must therefore assume system saturation beyond dating. Assuming saturation condition leads to the second interpretation. The observed N/P ratio is taken to be a saturated value ($N/P = \left(N/P\right)_{sat}$), and using Equation (35) one calculates δ_{sat}, the upper-limit value of δ:

$$\delta_{sat} = \frac{1}{N/P} - \lambda \tag{39}$$

The suitability of a given radionuclide to determine δ is determined by the condition that $\lambda \approx \left|\delta\right|$, i.e., the effective mean life and the radionuclide's mean life should be of the same order (Lal, 1991).

For shorter exposure histories, the N/P curves for depth samples (Figure 29) do not plot well. A necessary modification for the N/P ratio for short exposure histories might be:

$$\left(\frac{N}{P}\right)_{\text{mod}} = \frac{N - N_{inh}\cdot e^{-\lambda t}}{P} \tag{40}$$

where N_{inh} must be first estimated from a profile plot of measured concentration vs. depth.

Derivation of familiar cosmogenic equations

Starting at the "master equation" (30), it is straightforward to derive all the familiar cosmogenic equations, as shown below.

Erosion (Lal, 1991)

$$\begin{aligned}
&U = 0, z = const;\\
&N(x,t) = N_{inh}\cdot e^{-\lambda t} + \frac{P(z_0,x_0)\cdot e^{-\lambda t}}{\lambda+\mu\varepsilon}\left(e^{(\lambda+\mu\varepsilon)t}-1\right)\\
&= N_{inh}\cdot e^{-\lambda t} + \frac{P(z_0)\cdot e^{-\lambda t}\cdot e^{(\lambda+\mu\varepsilon)t}\cdot e^{Mz_0-\mu x_0}}{\lambda+\mu\varepsilon}\left(1-e^{-(\lambda+\mu\varepsilon)t}\right)\\
&= N_{inh}\cdot e^{-\lambda t} + \frac{P(z_0)e^{-\mu(x_0-\varepsilon t)}}{\lambda+\mu\varepsilon}\left(e^{MUt}-e^{-(\lambda+\mu\varepsilon)t}\right)\\
&N(x,t) = N_{inh}\cdot e^{-\lambda t} + \frac{P(z_0)e^{-\mu x}}{\lambda+\mu\varepsilon}\left(1-e^{-(\lambda+\mu\varepsilon)t}\right)
\end{aligned} \tag{41}$$

where $N_{inh} = N(x,0)$ is the initial concentration of a strata now at depth x, and z_0 is the constant elevation of the surface.

Deposition (Lal and Arnold, 1985)

To account for the profile which develops in the newly deposited strata, we define sedimentation rate as "negative" erosion $\varepsilon < 0$, and the thickness of material deposited above the disconformity as $x_{ss} = -\varepsilon t$. The time since burial of any layer now at depth x is hence $t_x = -x/\varepsilon$. The complete solution splits into two. For layers below the disconformity ($x > x_{ss}$), Equation 41 applies, while for layers above the disconformity ($x \le x_{ss}$), $-x/\varepsilon$ is substituted for t.

$$N(x,t) = \begin{cases} x \le x_{ss} & N(0)e^{-\lambda\frac{x}{-\varepsilon}} + \dfrac{P(0)e^{-\mu x}}{\lambda+\mu\varepsilon}\left(1-e^{(\frac{\lambda}{\varepsilon}+\mu)x}\right) \\ x > x_{ss} & N(x,0)e^{-\lambda t} + \dfrac{P(0)e^{-\mu x}}{\lambda+\mu\varepsilon}\left(1-e^{-(\lambda+\mu\varepsilon)t}\right) \end{cases} \tag{42}$$

Uplift without erosion (Brown, 1991)

$$\varepsilon = 0, x = x_0 = 0;$$
$$N(x_0,t) = N_{inh} \cdot e^{-\lambda t} + \frac{P(z_0,x_0)}{\lambda + MU}\left(e^{MUt} - e^{-\lambda t}\right) \tag{43}$$

Uplift with erosion (Brook et al., 1994)

$$\begin{aligned} N(t) &= N_{inh} \cdot e^{-\lambda t} + \frac{P(z_0,x_0) \cdot e^{-\lambda t}}{\lambda + MU + \mu\varepsilon}\left(e^{(\lambda+MU+\mu\varepsilon)t} - 1\right) \\ &= N_{inh} \cdot e^{-\lambda t} + \frac{P(z_0,x_0) \cdot e^{-\lambda t} \cdot e^{(\lambda+\mu\varepsilon)t} \cdot e^{-\mu x_0}}{\lambda + MU + \mu\varepsilon}\left(e^{MUt} - e^{-(\lambda+\mu\varepsilon)t}\right) \\ &= N_{inh} \cdot e^{-\lambda t} + \frac{P(z_0,x_0) e^{-\mu(x_0-\varepsilon t)}}{\lambda + MU + \mu\varepsilon}\left(e^{MUt} - e^{-(\lambda+\mu\varepsilon)t}\right) \\ N(t) &= N_{inh} \cdot e^{-\lambda t} + \frac{P(z_0,x)}{\lambda + MU + \mu\varepsilon}\left(e^{MUt} - e^{-(\lambda+\mu\varepsilon)t}\right) \end{aligned} \tag{44}$$

8.3. Paleo-drainage exploration scheme

With growing interest in deciphering the fluviatile histories of extraterrestrial planets such as Mars (e.g., Craddock and Maxwell, 1993), it is interesting to review the 50-year evolution of the paleo-drainage research in the Negev Desert (e.g., Bentor and Vroman, 1957; Garfunkel and Horowitz, 1966; Ginat, 1997; Avni, 1998; Matmon et al., 2009), and suggest the following conceptual scheme of paleo-drainage exploration.

1. **Description and characterization of fluviatile units** by means of
    a) Representative columnar sections
    b) Classification into units, and description of their field relations
    c) Recognition of "facies" (different clast assemblages within the same unit at different geographical locations)
    d) Field mapping of units and facies
2. **Reconstruction of paleo-flow directions** based on a unit's
    a) lithology of clasts and their possible sources (outcrop origins); diminishing input of clasts farther away from their source
    b) clast imbrication
    c) spatial continuity of mapped units
    d) present-day topographical position.
3. **Description of the present-day spatial configuration of a unit** by means of
    a) Stream length profiles, geological cross-sections
    b) Fence diagrams between columnar sections, isopach maps
    c) Structural maps of the base and/or top of a unit
    d) morphostratigraphic relations between units
4. **Identification of topographic, morphostratigraphic and lithologic problems** that arise from (3), such as:
    a) Evidence of river gradient change: steepening, shallowing, cancelling or even reversal of the original gradients (given its present-day topographical configuration of outcrops, the river could not have flown in the reconstructed direction.)
    b) Beheaded streams, evidence of shifting of channels and of water divides.
    c) Different morphostratigraphic relations between the same units (e.g., up- vs. down-stream)
    d) Clast size not matching current or reconstructed gradients etc.

5. **Resolution of the problems posed in (4)** by looking for evidence of:
    a) **Tectonic deformation:**
        - Pre- or syn-depositional tectonic activity.
        - Post-depositional faults and flexures, tilting on a large wavelength
        - Geomorphic disturbances (laterally offset channels, knickpoints, windgaps, badlands, sharp changes in stream direction etc.)
        - Recent seismicity along tectonic lines
    b) **River incision and erosion processes**
        - Effects of basin area, stream gradient and channel width
        - Limiting factors on sediment generation and/or accumulation rates.
        - Hiatuses and unconformities.
    c) **Climate or environmental change**
        - Effects of global climate cycles
        - A different paleoclimate, e.g., recorded by paleosols and/or fauna
        - Emergence of topographical barriers and their effect on local climate
        - Mechanisms of water accumulation in lake deposits
6. **Geological history:**
    a) Paleogeography of each unit
    b) Refined delineation of flow directions and basin outlines
    c) A time framework of drainage evolution via absolute dating of the deposition and abandonment times of the sediments, their accumulation rates and basin-wide erosion rates.

8.4. Algorithms

Below are given some of the algorithms (written in MatLab) which were used for calculation and plotting of the results shown in the thesis.

blockrot.m

```
% Block rotation module
% written by Benny Guralnik (benny.guralnik@gmail.com)
%
% This program performs rotation of blocks with a given initial geometry
% of width, fault angle and elevations.
windowpos=[30 200 1100 500];
axisdef=[-5e3 40e3 -400 700];

h=figure(1); set(h,'Position',windowpos)
w = [
% width[m]  b[deg]  west[m] east[m] block to the east of fault...
    10e3    80      420     350     %Halamish
     5e3    90      440     320     %Zehiha
     2e3    100     355     320     %Hiyyon
     8e3    90      360     210     %Qetzev
     8e3    80      260     200     %Milhan
];

%initial gradient
params=[
    2e2    %blocks height [m]
    450    %elevation on the west [m]
    0.25   %original westward gradient [deg]
   -.55     %block rotation [deg]
   -.60     %surface rotation [deg]
   -5e3    %surface rotation x axis [m]
    400    %surface rotation y axis [m]
];

steps=40;
% read the parameters
x=0;
h=params(1);
top=params(2);
gr=tan(deg2rad(params(3)));
alpha=params(4);
beta=params(5);
sfcrot = params(6:7)';
abstop=top;

%construct the geometry of the blocks
nb=size(w,1); %number of blocks
wu(1,:)=[0 abstop 0 abstop-h];
for j=1:nb;
    b=w(j,2);
    if b==90; dx=0; else dx=-h./tan(deg2rad(b)); end;
    wu(j+1,:)=[wu(j,1)+w(j,1) wu(j,2)+w(j,1).*gr wu(j,1)+w(j,1)+dx abstop-h];
end
for j=1:nb;
    data{j} = [wu(j,1:2); wu(j+1,1:2); wu(j+1,3:4); wu(j,3:4); wu(j,1:2);];
    w(j,5)=wu(j+1,3)- wu(j,3);
    datac(j,:) = data{j}(3,:);
    plot(data{j}(:,1), data{j}(:,2)); hold on
end;
sb=size(data{1},1); %number of points in each block
axis(axisdef); F = getframe(gcf); hold off;

%do visualization steps
for i=(1-(steps>0)):1:steps;
    alphanow=alpha./steps.*i;
    betanow=beta./steps.*i;
    rotalpha=[cos(deg2rad(alphanow)) sin(deg2rad(alphanow)); -sin(deg2rad(alphanow))
cos(deg2rad(alphanow))];
    rotbeta=[cos(deg2rad(betanow)) sin(deg2rad(betanow)); -sin(deg2rad(betanow))
cos(deg2rad(betanow))];
    dx=w(:,5).*(sin(deg2rad(w(:,2)))./sin(deg2rad(w(:,2)))-deg2rad(alphanow)-1); dx(1)=0;
    for j=1:nb
        block=data{j};
        %rotate the blocks one against the other on a flat surface
        origin=repmat(datac(j,:),sb,1);
```

```
        bl=origin+(block-origin)*rotalpha+repmat([sum(dx(1:j)) 0],sb,1);
        %rotate the surface on which the blocks are leaned
        origin=repmat(sfcrot,sb,1);
        bl=origin+(bl-origin)*rotbeta;
        plot(bl(:,1),bl(:,2)); hold on;
        mdl(2*(j-1)+1:2*(j-1)+2,1)=bl(1:2,2);
    end %j
axis(axisdef); F = getframe(gcf); hold off;
%if steps>1; wait=waitforbuttonpress; end
end %i

%plot observed elevations
hold on;
x=0; obs=[];
for j=1:size(w,1)
    obs = [obs; x w(j,3); x+w(j) w(j,4)];
    x=x+w(j,1);
end %j
plot(obs(:,1),obs(:,2),'-r'); hold on;

o=obs;
m=mdl;
```

npexact.m

```
% N/P exact curve module
% written by Benny Guralnik (benny.guralnik@gmail.com)
%
% This program calculates and plots the N/P ratio for a sample with KNOWN:
%   1. latitude:                          lat  [decimal deg.]
%   2. present elevation:                 Z    [masl]
%   3. depth below ground:                X    [m]
%   4,5. measured concentration:          N ± Nerr [atoms /g]
%   6. amount of vertical tectonic mvt:   dz [m]
clear; clc; tic;
%%% Constants
thalf = 1.36e6; lam = log(2)./thalf;  % halflife and decay const
LAM = 150;           % attenuation depth [g/cm^2]
P_SLHL = 4.58;       % Sea Level High Latitude production rate
grid_dz = 2;              % elevation spacing of the age-uplift grid
grid_dt = 1e4;            % time spacing of the age-uplift grid
Perr = 0;            % relative error of production rate
%%% Data goes below
data = [
% 1      2   3   4   5   6     7    8        9        10   11
% lat    Z   X   rho h   ft    l    N        Nerr     dz   dzerr name
30.19309 433 0.0 2.7 1.5 1.000 15.0 6.099E+6 1.484E+5 -10  10    %EZ
%30.14658 255 0.0 2.7 1.5 1.000 30.0 5.115E+6 1.281E+5 -195 20   %ES
];
%%% RGB color data (in the same order of "data")
datac = [
0 0 1
1 0 0
];
%%% Main program starts here
% create an age-uplift grid
[t,U]=meshgrid(1.3e6:grid_dt:1.9e6, 0:-grid_dz:-200);
for i=1:size(data,1)
    lat=data(i,1); Zf=data(i,2); X=data(i,3); rho=data(i,4); h=data(i,5);
    ft=data(i,6); fx=exp(-rho./LAM.*X); fh=LAM./(rho.*h).*(1-exp(-(rho.*h)./LAM));
    N=data(i,8); Nerr=data(i,9); dz=data(i,10); dzerr=data(i,11);
    NP=t.*0; % initialize the modeled concentration grid
    for it=1:1:size(t,1);     % iterate through age
        for iU=1:1:size(t,2); % iterates through uplift
            tnow=t(it,iU); Unow=U(it,iU);
            Zi=Zf-Unow;       % determine initial elevation
            elevs = Zi:-grid_dz:Zf;  % create the elevation change record
            lats = lat.*ones(1,size(elevs,2)); % repeat the latitude
            time = tnow./size(elevs,2); % time spent at each elevation
            % calculate the in-situ production for each elevation
            fla = stone2000(lats,elevs); Pis = ft.*fla.*fx.*fh.*P_SLHL;
            % model the concentration according to the tectonic history
            mN=0;
            for ie=1:size(elevs,2)
                mN=mN.*exp(-lam.*time)+Pis(ie)./lam.*(1-exp(-lam.*time));
            end %ie
            NP(it,iU)=mN;
        end %gU
    end %gt
    % divide modeled concentrations by the current in-situ production rate
```

```
    P = Pis(end); NP=NP./P;
    %%% Plot starts here
    v=[ (N./P).*(1 - sqrt((Nerr./N).^2 + Perr.^2));
        (N./P).*(1 + sqrt((Nerr./N).^2 + Perr.^2)); ];
    C = contour(t,U,NP,v,'LineWidth', 2, 'Color', datac(i,:)); hold on;
    tU = t.*U./1e6;
    v = [ dz-dzerr;
          dz+dzerr; ];
    C = contour(t,U,tU,v,'LineWidth', 2, 'Color', datac(i,:)); hold on;
end %i

% calculate age*uplift product for each point on the plot
% for i=1:length(contdata)
%     contdata{i}(:,3)=contdata{i}(:,2).*contdata{i}(:,1)./1e6;
% end;
% pretty up the plot
title('Age-subsidence plot');
xlabel('True exposure age [Ma]');
ylabel('Uplift [m/Ma]');
toc
```

tecthist.m

```
% Tectonic history module
% written by Benny Guralnik (benny.guralnik@gmail.com)
%
% This program constructs random monotonous elevation-time paths and
% simulates the cosmogenic concentration of an exposed surface through time.
% Only such paths are shown, for which the modeled concentration reproduces
% the actual one within its error. The following parameters are used:
% KNOWN:
%   1. current latitude:                    lat        [decimal deg.]
%   2. current site elevation:              Zf         [masl]
%   3. sample depth below ground:           X          [m]
%   4. sediment density:                    rho        [kg / m^3]
%   5. sample thickness:                    h          [cm]
%   6. topographic shielding factor:        ft         [1]
%   8,9. measured final concentration:      N ± Nerr   [atoms /g]
% ASSUMED:
%   10,11. amount of vertical change:       dz ± dZerr [masl]
%   12,13. total exposure time:             ti ± tierr [yr]
%   14,15. initial cosmogenic concentration: N0 ± N0err [atoms /g]
clear; clc;
%%% Constants
thalf = 1.36e6; lam = log(2)./thalf;  % halflife and decay const
LAM = 150;              % attenuation depth [g/cm^2]
M = 1250.^-1;           % mean attenuation distance in atmosphere [m^-1]
k = 0;                  % succesful paths counter
P_SLHL=4.58;                % Sea Level High Latitude production rate
Perr = 0.02;                % relative error on in-situ production rate
tries = 1500;               % number of paths to be generated and tested
axisdef = [-.05 1.8 240 460]; % definition of x and y axes extents
xticks = -.1:0.1:1.8;         % ticks on the x axis
yticks = 240:20:460;          % ticks on the y axis

%%% Data goes below
data = [
% 1      2   3   4   5   6     7    8        9        10   11    12     13     14  15    16
% lat    Z   X   rho h   ft    l    N        Nerr     dz   dzerr ti     tierr  N0  N0err name
30.14658 255 0.0 2.7 1.5 1.000 30.0 5.115E+6 1.281E+5 -195 0     1.616e6 0.089e6 2e5 0     %ES
];

%%% Main program starts here
% constant values
i=1;
lat=data(i,1); Zf=data(i,2); X=data(i,3); rho=data(i,4); h=data(i,5);
ft=data(i,6); fx=exp(-rho./LAM.*X); fh=LAM./(rho.*h).*(1-exp(-(rho.*h)./LAM));
N=data(i,8); Nerr=data(i,9);
mZi = Zf - data(i,10); mZierr = data(i,11);
mti = data(i,12); mtierr = data(i,13);
mN0 = data(i,14); mN0err = data(i,15);
tf = 0;                                     % current time
fla = stone2000(lat,Zf); Pis = ft.*fla.*fx.*fh.*P_SLHL; % in-situ production rate
NPl = N./Pis.*(1 - sqrt((Nerr./N).^2 + Perr.^2)); % lower limit
NPu = N./Pis.*(1 + sqrt((Nerr./N).^2 + Perr.^2)); % upper limit
for i=1:tries;
    i %show counter
    % generate starting values
    Zi = mZi+mZierr.*(rand-0.5).*2;    % elevation
    ti = mti+mtierr.*(rand-0.5).*2;    % time
```

```
    mN = mN0+mN0err.*(rand-0.5).*2;    % inheritance
    % generate event points of a random monotonous tectonic history
    % and calculate time increments between event points
    h=randpathfix([ti Zi; tf Zf;]); nh=size(h,1);
    for j=1:nh-1; h(j,3) = abs(h(j+1,1)-h(j,1)); end %j
    lats = lat.*ones(size(h,1),1); % repeat the latitude
    % in-situ production rate
    fla = stone2000(lats,h(:,2)); Pis = ft.*fla.*fx.*fh.*P_SLHL;
    % go over the time increments and build up the concentration
    for j=1:nh-1;
        dt=h(j,3); znow=h(j,2);
        mN = mN.*exp(-lam.*dt) + Pis(j)./lam.*(1-exp(-lam.*dt));
    end %j
    % save history whose modeled N/P ratio replicates the observed value
    NPmod=mN./Pis(end);
    if (NPmod>=NPl && NPmod<=NPu); k = k + 1; paths{k} = h; end %if
end %i
% calculate the "mean" tectonic history
meanhist = [];
for t=0:((ti+mtierr)/100):(ti+mtierr);
    elev=[];
    for i=1:length(paths);
        elev(i) = paths{i}(nearestpoint(t, paths{i}(:,1)),2);
    end %i
    meanhist = [meanhist; t mean(elev)];
end %t
% calculate the instantaneous tectonic rate
for i=2:size(meanhist,1);
    meanhist(i,3)=(meanhist(i,2)-meanhist(i-1,2)); %dz
    meanhist(i,4)=(meanhist(i,1)-meanhist(i-1,1)); %dt
    meanhist(i,5)=meanhist(i,3)./meanhist(i,4).*1e6; %dz/dt
end;
%%% Plots start here
figure(1)
% plot all possible paths
for i=1:length(paths);
    h=paths{i};
    plot(h(:,1)./1e6,h(:,2),'-k','Color',[.5 .5 .5],'Linewidth',1); hold on
end
% plot the mean path
plot(meanhist(:,1)./1e6,meanhist(:,2),'-r','LineWidth', 2); hold on
% pretty up the plot
title('Possible subsidence histories at site ES');
xlabel('Time [Ma BP]'); ylabel('Elevation [masl]');
set(gca,'XDir','reverse'); set(gca,'XTick',xticks); set(gca,'YTick',yticks);
axis(axisdef);
% plot instantaneous rates
figure(2)
plot(-meanhist(:,1)./1e6,meanhist(:,5),'-r'); hold on;
```

randpath.m

```
function out = randpath(origin, target);
% written by Benny Guralnik (benny.guralnik@gmail.com)
% Usage:
%   returns a random monotonous path from [origin] to [target] using steps
%   no bigger than [v_min]
% Input arguments:
%   origin and target are 2D vectors of the form [x y]
% Output arguments:
%   out is a vector containting cosecutive [x y] pair in each row, i.e.
%   [x1 y1; x2 y2; ... ; xn yn;]
% Example:
%   a = randpath([0 0],[1 1])
%   plot(a(:,1),a(:,2))
v_min = 0.05; % minimal displacement (out of 1)
path = [];    % path history
current_position = origin;
v_togo = target-origin;
while norm(v_togo) > v_min;
    v = [target - current_position].*[rand rand]; %random displacement
    if norm(v) > v_min % break a large displacement further down by recursion
        path=[path; randpath(current_position, current_position + v)];
    end
    path=[path; current_position + v]; % save current position
    v_togo = v_togo - v;
    current_position = current_position + v;
end
out=path;
```

randpathfix.m

```
function out = randpathfix(data);
% written by Benny Guralnik (benny.guralnik@gmail.com)
% Usage:
%   returns a random monotonous path going consecutively through all points
%   specified in [data]
% Input arguments:
%   data is a vector containting cosecutive [x y] pair in each row, i.e.
%   [x1 y1; x2 y2; ... ; xn yn;]
% Output arguments:
%   out is a vector containting cosecutive [x y] pair in each row, i.e.
%   [x1 y1; x2 y2; ... ; xn yn;]
% Example:
% data = [0 0; 1 1; 3.5 4.6; 5 5;];
% a = randpathfix(data); plot(a(:,1),a(:,2),'-k'); hold on; plot(data(:,1),data(:,2),'or');
chain=data(1,:);
for i=1:size(data,1)-1
    elevhist=[];
    rp=randpath([0,0],[1,1]);
    elevhist(:,1) = data(i,1) + (data(i+1,1)-data(i,1)).*rp(:,1);
    elevhist(:,2) = data(i,2) + (data(i+1,2)-data(i,2)).*rp(:,2);
    chain=[chain; elevhist; data(i+1,:)];
end
out=chain;
```

nearestpoint.m

```
function [IND, D] = nearestpoint(x,y,m) ;
% NEARESTPOINT - find the nearest value in another vector
%
%   IND = NEARESTPOINT(X,Y) finds the value in Y which is the closest to
%   each value in X, so that abs(Xi-Yk) => abs(Xi-Yj) when k is not equal to j.
%   IND contains the indices of each of these points.
%   Example:
%      NEARESTPOINT([1 4 12],[0 3]) -> [1 2 2]
%
%   [IND,D] = ... also returns the absolute distances in D,
%   that is D == abs(X - Y(IND))
%
%   NEARESTPOINT(X, Y, M) specifies the operation mode M:
%   'nearest' : default, same as above
%   'previous': find the points in Y that are closest, but preceeds a point in X
%               NEARESTPOINT([0 4 3 12],[0 3],'previous') -> [NaN 2 1 2]
%   'next'    : find the points in Y that are closets, but follow a point in X
%               NEARESTPOINT([1 4 3 12],[0 3],'next') -> [2 NaN 2 NaN]
%
%   If there is no previous or next point in Y for a point X(i), IND(i)
%   will be NaN.
%
%   X and Y may be unsorted.
%
%   This function is quite fast, and especially suited for large arrays with
%   time data. For instance, X and Y may be the times of two separate events,
%   like simple and complex spike data of a neurophysiological study.
%   Nearestpoint('test') will run a test to show it's effective ness for
%   large data sets
% Created       : august 2004
% Author        : Jos van der Geest
% Email         : matlab@jasen.nl
% Modifications :
%  aug 25, 2004 - corrected to work with unsorted input values
%  nov 02, 2005 -
%  apr 28, 2006 - fixed problem with previous points
if nargin==1 & strcmp(x,'test'),
    testnearestpoint ;
    return
end
error(nargchk(2,3,nargin)) ;
if nargin==2,
    m = 'nearest' ;
else
    if ~ischar(m),
        error('Mode argument should be a string (either ''nearest'', ''previous'', or
''next'')') ;
    end
end
if ~isa(x,'double') | ~isa(y,'double'),
    error('X and Y should be double matrices') ;
end
```

```
% sort the input vectors
sz = size(x) ;
[x, xi] = sort(x(:)) ;
[dum, xi] = sort(xi) ; % for rearranging the output back to X
nx = numel(x) ;
cx = zeros(nx,1) ;
qx = isnan(x) ; % for replacing NaNs with NaNs later on
[y,yi] = sort(y(:)) ;
ny = length(y) ;
cy = ones(ny,1) ;
xy = [x ; y] ;
[xy, xyi] = sort(xy) ;
cxy = [cx ; cy] ;
cxy = cxy(xyi) ; % cxy(i) = 0 -> xy(i) belongs to X, = 1 -> xy(i) belongs to Y
ii = cumsum(cxy) ;
ii = ii(cxy==0).' ; % ii should be a row vector
% reduce overhead
clear cxy xy xyi ;
switch lower(m),
    case {'nearest','near','absolute'}
        % the indices of the nearest point
        ii = [ii ; ii+1] ;
        ii(ii==0) = 1 ;
        ii(ii>ny) = ny ;
        yy = y(ii) ;
        dy = abs(repmat(x.',2,1) - yy) ;
        [dum, ai] = min(dy) ;
        IND = ii(sub2ind(size(ii),ai,1:nx)) ;
    case {'previous','prev','before'}
        % the indices of the previous points
        ii(ii < 1) = NaN ;
        IND = ii ;
    case {'next','after'}
        % the indices of the next points
        ii = ii + 1 ;
        ii(ii>ny) = NaN ;
        IND = ii ;
    otherwise
        error(sprintf('Unknown method "%s"',m)) ;
end
IND(qx) = NaN ; % put NaNs back in
% IND = IND(:) ; % solves a problem for x = 1-by-n and y = 1-by-1
if nargout==2,
    % also return distance if requested;
    D = repmat(NaN,1,nx) ;
    q = ~isnan(IND) ;
    D(q) = abs(x(q) - y(IND(q))) ;
    D = reshape(D(xi),sz) ;
end
% reshape and sort to match input X
IND = reshape(IND(xi),sz) ;
% because Y was sorted, we have to unsort the indices
q = ~isnan(IND) ;
IND(q) = yi(IND(q)) ;
% END OF
```

profileage.m

```
% fit profile age module
% written by Benny Guralnik (benny.guralnik@gmail.com)
%
% This program calculates the best-fit exposure age for a profile of
% several depth samples, for which the following is known:
%   1. current latitude:                    lat        [decimal deg.]
%   2. current site elevation:              Zf         [masl]
%   3. sample depth below ground:           X          [m]
%   4. sediment density:                    rho        [kg / m^3]
%   5. sample thickness:                    h          [cm]
%   6. topographic shielding factor:        ft         [1]
%   8,9. measured final concentration:      N ± Nerr   [atoms /g]
%
% Parameters which the program finds are:
%   1. N0:    the inheritance (uniform to all samples) [atoms /g]
%   2. tdep:  the time period of deposition [y]
%   3. t:     the time period since exposure (erosion=0) [y]
clear; clc; tic;
%%% Constants
thalf = 1.36e6; lam = log(2)./thalf;  % halflife and decay const
LAM = 150;           % attenuation depth [g/cm^2]
P_SLHL = 4.58;       % Sea Level High Latitude production rate
```

```
%%% Data goes below
% % Q3
% data = [
% % 1      2   3   4   5   6     7    8        9
% % lat    Z   X   rho h   ft    l    N        Nerr     name
% 30.66203 73 0.05 1.8 15.0 0.999 0.0 1.178E+5 6.474E+3 %N1-Q3-015
% 30.66203 73 0.20 1.8 20.0 0.999 0.0 1.120E+5 9.074E+3 %N1-Q3-030
% 30.66203 73 0.60 1.8 20.0 0.999 0.0 1.117E+5 6.080E+3 %N1-Q3-070
% 30.66203 73 0.80 1.8 30.0 0.999 0.0 1.108E+5 4.648E+3 %N1-Q3-090
% 30.66203 73 1.30 1.8 20.0 0.999 0.0 1.153E+5 5.463E+3 %N1-Q3-140
% 30.66203 73 1.80 1.8 20.0 0.999 0.0 1.160E+5 4.528E+3 %N1-Q3-190
% 30.66203 73 2.00 1.8 20.0 0.999 0.0 1.188E+5 5.303E+3 %N1-Q3-210
% ];
% % value ranges for the Monte-Carlo simulation
% %1. inher. [atoms/g]   2. deposition time [y]      3. exposure time [y]
% N0val=2e5; N0err=1e5;  tdepval=50e3; tdeperr=50e3; tval=50e3; terr=50e3;
% xaxisdef=[1e5 1.4e5]; userows=[1 2 3 4 5 6 7];

% Q2
data = [
% 1      2   3   4   5   6     7    8        9
% lat    Z   X   rho h   ft    l    N        Nerr     name
30.66093 78 0.00 1.8 1.5 0.999 0.0 1.081E+6 2.722E+4 %N1-Q2-DP
30.66060 78 0.83 1.8 15.0 0.997 0.0 3.614E+5 1.066E+4 %N2-Q2-6
30.66060 78 3.06 1.8 15.0 0.997 0.0 1.479E+5 8.026E+3 %N2-Q2-4
30.66060 78 4.69 1.8 15.0 0.997 0.0 1.474E+5 7.612E+3 %N2-Q2-2
30.66060 78 5.31 1.8 15.0 0.997 0.0 1.330E+5 9.508E+3 %N2-Q2-1
];
% value ranges for the Monte-Carlo simulation
%1. inher. [atoms/g]   2. deposition time [y]      3. exposure time [y]
N0val=2e5; N0err=1e5;  tdepval=50e3; tdeperr=30e3; tval=200e3; terr=200e3;
xaxisdef=[1e5 1.2e6]; userows=[2 3 4 5];

%%% Main program starts here
% read data
i=1;
lat=data(i,1); Zf=data(i,2);
X=data(userows,3).*100
rho=data(userows,4); h=data(userows,5);
ft=data(userows,6); N=data(userows,8); Nerr=data(userows,9);
fla=stone2000(lat,Zf); %fla=dunai2000(lat,Zf);
mu=rho./LAM;
A = [];
for j=1:100
Pis = ft.*fla.*(P_SLHL + P_SLHL.*.1.*(rand-0.5).*2);
minchisquare=1e20;
for i=1:10000
    %generate random inheritance, deposition time and exposure time values
    N0=N0val+N0err.*(rand-0.5).*2;
    tdep=tdepval+tdeperr.*(rand-0.5).*2;
    t=tval+terr.*(rand-0.5).*2;
    %calculate depositional profile
    ero=-X(end)./tdep; sed=ero; N0=N0.*ones(length(X),1);
    NmodX = N0./lam.*ero.*exp(lam.*X./ero)+Pis./(lam+mu.*ero).* ...
        (-1./mu.*exp(-mu.*X)-1./lam.*ero.*exp(lam.*X./ero));
    NmodXh = N0./lam.*ero.*exp(lam.*(X+h)./ero)+Pis./(lam+mu.*ero).* ...
        (-1./mu.*exp(-mu.*(X+h))-1./lam.*ero.*exp(lam.*(X+h)./ero));
    Nmod=(NmodXh-NmodX)./h;
    %calculate exposure profile
    ero=0;
    NmodX = Nmod.*exp(-lam.*t).*X-(Pis./rho.*LAM.*exp(-rho.*X./LAM))./ ...
        (lam+mu.*ero).*(1-exp((-lam-mu.*ero).*t));
    NmodXh = Nmod.*exp(-lam.*t).*(X+h)-(Pis./rho.*LAM.*exp(-rho.*(X+h)./LAM))./ ...
        (lam+mu.*ero).*(1-exp((-lam-mu.*ero).*t));
    Nmod=(NmodXh-NmodX)./h;
    %calculate modified chi-square, and save the paramters if it's good
    chisquare=sqrt(sum(((Nmod-N)./Nerr).^2));
    if chisquare < minchisquare
        bestparams=[N0(1) tdep sed t chisquare];
        minchisquare=chisquare; Nmodbest=Nmod;
    end
end %i
ins = [bestparams'; bestparams(4)+X./-bestparams(3)];
A = [A ins];
end %j
for i=1:size(A,1)
    B(i,1)=mean(A(i,:));
    B(i,2)=std(A(i,:));
end
```

```
%%% Display results
ft=data(1,6); fla=stone2000(lat,Zf); Pis = ft.*fla.*P_SLHL;
rho=data(1,4); mu=rho./LAM;
for i=1:2
    N0=B(1,1); tdep=B(2,1); ero=B(3,1); t=B(4,1);
    if i==2
        X=linspace(0,X(end)+h(end),(X(end)+h(end)))'; h=X(2)-X(1);
    end
    %calculate depositional profile
    N0=N0.*ones(length(X),1);
    NmodX = N0./lam.*ero.*exp(lam.*X./ero)+Pis./(lam+mu.*ero).* ...
        (-1./mu.*exp(-mu.*X)-1./lam.*ero.*exp(lam.*X./ero));
    NmodXh = N0./lam.*ero.*exp(lam.*(X+h)./ero)+Pis./(lam+mu.*ero).* ...
        (-1./mu.*exp(-mu.*(X+h))-1./lam.*ero.*exp(lam.*(X+h)./ero));
    Nmod=(NmodXh-NmodX)./h;
    %calculate exposure profile
    ero=0;
    NmodX = Nmod.*exp(-lam.*t).*X-(Pis./rho.*LAM.*exp(-rho.*X./LAM))./ ...
        (lam+mu.*ero).*(1-exp((-lam-mu.*ero).*t));
    NmodXh = Nmod.*exp(-lam.*t).*(X+h)-(Pis./rho.*LAM.*exp(-rho.*(X+h)./LAM))./ ...
        (lam+mu.*ero).*(1-exp((-lam-mu.*ero).*t));
    Nmod=(NmodXh-NmodX)./h;
    if i==1
        plot(Nmod,X+h/2,'.r','MarkerSize',18); hold on;
    else
        plot(Nmod,X,'-r','LineWidth',2); hold on;
    end
end
% plot measured concentrations
X=data(:,3).*100; h=data(:,5); N=data(:,8); Nerr=data(:,9);
Nobs=[];
for i=1:length(X)
     Nobs=[Nobs; NaN NaN; N(i)-Nerr(i) X(i); N(i)-Nerr(i) X(i)+h(i); ...
         N(i)+Nerr(i) X(i)+h(i); N(i)+Nerr(i) X(i); N(i)-Nerr(i) X(i);];
end
plot(Nobs(:,1),Nobs(:,2),'-b' ,'LineWidth',2); hold on;
% pretty up the plot
title('Profile concentration plot');
xlabel('^1^0Be concentration [atoms g^-^1]');
ylabel('Profile depth [cm]');
axis([xaxisdef -5 X(end)+15]);
set(gca,'YDir','reverse');
toc
```

inheritance.m

```
% basin-wide erosion rates module
% written by Benny Guralnik (benny.guralnik@gmail.com)
%
% This program calculates sample inheritance based on deduction of OSL age
% equivalent concentration from a measured sample.
%   1. current latitude:                    lat        [decimal deg.]
%   2. current site elevation:              Z          [masl]
%   3. sample depth below ground:           X          [m]
%   4. sediment density:                    rho        [kg / m^3]
%   5. sample thickness:                    h          [cm]
%   6. topographic shielding factor:        ft         [1]
%   8,9. measured final concentration:      N ± Ns     [atoms /g]
%   10,11. measured OSL age:                t ± ts     [atoms /g]
%
clear; clc;
%%% Constants
thalf = 1.36e6; lam = log(2)./thalf;  % halflife and decay const
thalfs = 0.07e6; lams = sqrt((-log(2)/thalf(1)^2)^2*thalfs(1)^2);
LAM = 150;                % attenuation depth [g/cm^2]
M = 1250.^-1;             % mean attenuation distance in atmosphere [m^-1]
P_SLHL = 4.58;            % Sea Level High Latitude production rate
%%% Data goes below
data=[
% 1      2   3    4   5   6     7   8        9        10    11
% lat    Z   X    rho h   ft    l   N        Nerr     tOSL  terr name
30.34211 284 0.00 2.7 1.5 1.000 0.0 1.504E+6 3.647E+4 304e3 35e3 %P1-Q1-DPS
30.66093 78  0.00 2.7 1.5 0.999 0.0 1.081E+6 2.722E+4 212e3 38e3 %N1-Q2-DP
30.66060 78  0.00 2.7 1.0 0.997 0.0 1.27E+5  0.09E+5  0     0    %N2-Q2
30.34093 273 0.00 2.7 1.5 1.000 0.0 1.853E+6 4.340E+4 125e3 16e3 %P1-Q2-DP
30.66203 73  0.00 2.7 1.0 0.999 0.0 1.07E+5  0.04E+5  0     0    %N1-Q3
30.59118 380 0.00 2.7 5.0 0.966 0.0 1.61E+5  0.16E+5  0     0    %N4-NR-SD
];
```

```
%%% Main program starts here
for i=1:size(data,1)
    lat=data(i,1); Zf=data(i,2); X=data(i,3); rho=data(i,4); h=data(i,5);
    ft=data(i,6); fx=exp(-rho./LAM.*X); fh=LAM./(rho.*h).*(1-exp(-(rho.*h)./LAM));
    fla = stone2000(lat,Zf);
    % in-situ production rate
    P = ft.*fla.*fx.*fh.*P_SLHL; Ps = P.*0.1;
    % basin-wide averaged production rate ~ in-situ rate
    Pr = P; Prs = Pr.*0.1;
    % cosmogenic concentration and OSL age
    N = data(i,8); Ns = data(i,9);
    t = data(i,10); ts = data(i,11);
    % calculate inheritance and its uncertainty
    dN0dN = exp(lam*t);
    dN0dP = -1/lam*exp(lam*t)+1/lam;
    dN0dlam = P/lam^2*exp(lam*t)+(N-P/lam)*t*exp(lam*t)-P/lam^2;
    dN0dt = (N-P/lam)*lam*exp(lam*t);
    N0 = ((N-P/lam)*exp(lam*t)+P/lam);
    N0s = sqrt(dN0dN^2*Ns^2 + dN0dP^2*Ps^2 + dN0dlam^2*lams^2 + dN0dt^2*ts^2);
    % calculate apparent erosion rate and its uncertainty
    dedPr = LAM/rho/N0;
    dedN0 = -LAM/rho*P/N0^2;
    dedlam = -LAM/rho;
    e=LAM/rho*(Pr/N0-lam);
    es = sqrt(dedPr^2*Prs^2 + dedN0^2*N0s^2 + dedlam^2*lams^2);
    % append calculated estimates to data
    data(i,12) = N0; data(i,13) = N0s;
    data(i,14) = e.*1e4; data(i,15) = es.*1e4;
end %i
```

stone2000.m

```
function out = stone2000(lat,P, Fsp);
% Calculates the geographic scaling factor for cosmogenic-nuclide prodction as
% a function of site latitude and atmospheric pressure, according to:
%
% Stone, J., 2000, Air Pressure and Cosmogenic Isotope Production. JGR 105:B10,
% p. 23753.
%
% MODIFIED BY BENNY Syntax: scalingfactor = stone2000(latitude,altitude,fsp)
% Greg Balco -- UW Cosmogenic Isotope Lab
% First version, February 2001.
% Checked March, 2006 as part of the CRONUS-Earth Al-Be calculators.
P = stdatm(P);
if ~isempty(find(abs(lat) > 90));
    error('Latitudes below 90, please');
end;

if length(lat) ~= length(P);
    error('Vectors the same size, please');
end;
% default Fsp
if nargin == 2;
    Fsp = 0.978;
end;
% Spallogenic production at index latitudes;
% enter constants from Table 1
a = [31.8518 34.3699 40.3153 42.0983 56.7733 69.0720 71.8733];
b = [250.3193 258.4759 308.9894 512.6857 649.1343 832.4566 863.1927];
c = [-0.083393 -0.089807 -0.106248 -0.120551 -0.160859 -0.199252 -0.207069];
d = [7.4260e-5 7.9457e-5 9.4508e-5 1.1752e-4 1.5463e-4 1.9391e-4 2.0127e-4];
e = [-2.2397e-8 -2.3697e-8 -2.8234e-8 -3.8809e-8 -5.0330e-8 -6.3653e-8 -6.6043e-8];
ilats = [0 10 20 30 40 50 60];
% calculate index latitudes at given P's
lat0 = a(1) + (b(1) .* exp(P./(-150))) + (c(1).*P) + (d(1).*(P.^2)) + (e(1).*(P.^3));
lat10 = a(2) + (b(2) .* exp(P./(-150))) + (c(2).*P) + (d(2).*(P.^2)) + (e(2).*(P.^3));
lat20 = a(3) + (b(3) .* exp(P./(-150))) + (c(3).*P) + (d(3).*(P.^2)) + (e(3).*(P.^3));
lat30 = a(4) + (b(4) .* exp(P./(-150))) + (c(4).*P) + (d(4).*(P.^2)) + (e(4).*(P.^3));
lat40 = a(5) + (b(5) .* exp(P./(-150))) + (c(5).*P) + (d(5).*(P.^2)) + (e(5).*(P.^3));
lat50 = a(6) + (b(6) .* exp(P./(-150))) + (c(6).*P) + (d(6).*(P.^2)) + (e(6).*(P.^3));
lat60 = a(7) + (b(7) .* exp(P./(-150))) + (c(7).*P) + (d(7).*(P.^2)) + (e(7).*(P.^3));
% initialize output
correction = zeros(size(P));
% northernize southern-hemisphere inputs
lat = abs(lat);
% set high lats to 60;
lat(find(lat > 60)) = (zeros(size(find(lat > 60))) + 60);
% loop
b =1;
```

```
while b <= length(lat);
    %interpolate for actual elevation:
    S(b) = interp1(ilats,[lat0(b) lat10(b) lat20(b) lat30(b) lat40(b) lat50(b) lat60(b)],
lat(b));
    % continue loop
    b = b+1;
end;
% Production by muons
% constants
mk = [0.587 0.600 0.678 0.833 0.933 1.000 1.000];
% index latitudes at given P's
ml0 = mk(1) .* exp((1013.25 - P)./242);
ml10 = mk(2) .* exp((1013.25 - P)./242);
ml20 = mk(3) .* exp((1013.25 - P)./242);
ml30 = mk(4) .* exp((1013.25 - P)./242);
ml40 = mk(5) .* exp((1013.25 - P)./242);
ml50 = mk(6) .* exp((1013.25 - P)./242);
ml60 = mk(7) .* exp((1013.25 - P)./242);
% loop
b =1;
while b <= length(lat);
    %interpolate for actual elevation:
    M(b) = interp1(ilats,[ml0(b) ml10(b) ml20(b) ml30(b) ml40(b) ml50(b) ml60(b)], lat(b));
    % continue loop
    b = b+1;
end;
% Combine spallogenic and muogenic production; return
Fm = 1 - Fsp;
out_1 = ((S .* Fsp) + (M .* Fm));
% make vectors horizontal
if size(out_1,1) > size(out_1,2);
    out = out_1';
else;
    out = out_1;
end;
%========== subfunctions ================================================
function out = stdatm(z);
% stdatm.m
% Syntax: pressure = stdatm(elevation)
% Units: elevation in m; pressure in hPa; accepts vector arguments
% This function converts elevation to atmospheric pressure according
% to the "standard atmosphere" (cf. CRC Handbook of Chem and Phys).
%
% Greg Balco -- UW Cosmogenic Isotope Lab
% First version, Feb. 2001
% checked March, 2006 as part of the CRONUS-Earth Be-10/Al-26
% calculators.
% define constants
gmr = -0.03417;
Ts = 288.15;
dtdz = 0.0065;
Ps = 1013.25;
% calculation
out_1 = Ps .* exp( (gmr/dtdz) .* ( log(Ts) - log(Ts - (z.*dtdz)) ) );
% return a row vector
if size(out_1,1) > size(out_1,2);
    out = out_1';
else;
    out = out_1;
end;
```

הפלייסטוקן המוקדם. בתוך קבוצה זו כלולים גם 2 גילים צעירים (0.2 – 0.5 מ״ש) מקו פרשת המים של מזרח אגן המישר, המציינים את נסיגתו של קו פרשת מים זה למערב בעקבות התחתרות לאחור של נחל עשוש אל תוך תצורות רכות (ע׳רב ות׳קיה) הבונות קו פרשת מים זה.

קצב ההשתפלות של גב הערבה במהלך הפליו-פלייסטוקן הוערך בעזרת גיל הנטישה של משארי תצורת צחיחה בקו פרשת המים בין נחל שיטה לנחל חיון (1.63±0.27 מ״ש). באתר זה, נמצאים המשקעים של אפיק אדום כ-330 מ׳ מתחת לגובה הרבדתם המשוחזר. בהנחה כי תחילת ההשתפלות החלה בזמן לא מוגדר בפליוקן והסתיימה ב- 1.63±0.27 מ״ש, קצב ההשתפלות הצפוי נע בין 300 ל-100 מ׳/מ״ש, בהתאמה לקצבים המוכרים מאזור שולי דרום ים המלח ואף נמוך מהם. אולם, אינטרפרטציה זו מתעלמת מקיום טקטוניקה במהלך הפלייסטוקן בנגב ומקדימה בצורה לא סבירה את זמן הרבדת תצורת צחיחה אל הפליוקן. כיוון שקצב הייצור של איזוטופים קוסמוגנים גדל עם הגובה האבסולוטי, משטח שהשתפל *במהלך זמן חשיפתו* יראה גיל עתיק יותר מגילו האמיתי. באינטרפטציה המתוקנת הנחנו, שקו פרשת המים שיטה-חיון השתפל לאחר שכבר כוסה בריצוף מדברי, ולכן הריכוז הקוסמוגני שנמדד מכיל *סיגנל מעורב של זמן חשיפה מחד ושינויי גובה מאידך*. השוואת ריכוז קוסמוגני זה לריכוז שנמדד בקו פרשת המים חיון/ציחור ושלא עבר השתפלות משמעותית, מאפשרת לשחזר את עיקר ההשתפלות של הנגב אל הבקע ל- 1.0 – 1.6 מ״ש בעוצמה הולכת ודועכת עם הזמן. האטה טקטונית זו מסבירה את מיעוט הטרסות האלוביאליות בנגב המרכזי והדרומי מגילי פלייסטוקן מוקדם עד תיכון, כיוון שמשטר הנחלים השלט באותה תקופה היה של הסתגלות והתחתרות אינטנסיבית אל בסיס סחיפה הולך ויורד, ולא של הרבדה.

<u>תארוך טרסות מהפלייסטוקן המאוחר (פרק 4)</u> התמקד בסדרת טרסות המשתרעות על שטחים גדולים בנגב המרכזי והדרומי, ומעידות על ייצוב טקטוני ומעבר לשלטון אקלימי במשטרים הנחליים. שתי טרסות אלוביאליות סמוכות בקניון נקרות, שבהן נדגמו פרופילי עומק מפורטים בשיטות האיזוטופים הקוסמוגנים והלומיניסנציה, הראו גילים של 200~ אלף ו-10~ אלף שנה, ובהתאמה טובה בין שתי השיטות. ריכוזים קוסמוגניים התחלתיים בסדימנט חולי המשוחזרים מחתכים אלו דומים לריכוז הקוסמוגני בחול הזורם כיום בנחל נקרות ובמוצא מכתש רמון, ויכולים להתפרש כקצבי ארוזיה מדומים של אבן-חול במכתש רמון של 16-21 מ׳/מ״ש במשך 300 אלפי השנים האחרונות. בטרסה הבוגרת בנחל נקרות ובשתי טרסות נוספות בגרבן כרכם (גילי OSL של 100~ אלף ו-300 אלף שנה) הוערך גם קצב הארוזיה של צור בעזרת השוואת גילי הקבורה של הטרסות בשיטת ה-OSL לגילי חשיפה קוסמוגניים של ה״ריצוף המדברי״. קצבי הארוזיה המדומים של צור הראו שונות גדולה יותר מזו של קצב הארוזיה הממוצע של חול; מגמה של ירידה בקצב הארוזיה של צור מ-13 מ׳/מ״ש לפני 300 אלף שנה עד כדי 2 מ׳/מ״ש כיום יכולה לתמוך בקיום תהליך המדבור אשר גורם לייצוב המדרונות באזור המחקר.

<u>בנסיון לתארך את גיל הרבדת תצורת הערבה (פרק 6)</u> נדגם חומר אלוביאלי אשר כיום ממוסך לגמרי מקרניים קוסמיות, זאת בשלוש מערות עמוקות שבמחשופי תצורת הערבה בנחל ערוד שבגרבן כרכם. בעיות פרוצדורליות ואנליטיות בקביעת ריכוז ה-^{26}Al אינם מאפשרים שיפור של מסגרת הזמנים המוכרת, ומדגישים את הצורך במדידות מחודשות על מנת לקבל גילי הרבדה אמינים לתצורה זו.

האפקט המשולב של יצירה ודעיכה של איזוטופ קוסמוגני רדיואקטיבי מהווה למעשה גאוכרונומטר, המאפשר לתארך את זמן החשיפה של סלע לקרינה קוסמית טרם הגעת הריכוז לשיווי משקל סקולרי (ריכוז קבוע המושג כאשר קצבי הייצור והדעיכה משתווים, לרוב לאחר כ-3 עד 4 זמני מחציות חיים של האיזוטופ). מאידך, הנחת שיווי משקל איזוטופי סקולרי בסלעי bedrock העוברים דנודציה מתמדת, מאפשרת לפרש את הריכוזים הקוסמוגניים הנמדדים בהם כקצבי ארוזיה (כלומר מהירות הסילוק המכאני של איזוטופים קוסמוגנים מעמודת סלע לעומת קצב יצירתם בו). בעבודה הנוכחית נעשה שימוש באיזוטופים ^{10}Be ו-^{26}Al שהינם איזוטופים קוסמוגנים לא יציבים (זמני מחצית חיים של 1.36 מ״ש ו-0.7 מ״ש, בהתאמה) הנוצרים מפגיעת קרינה קוסמית משנית באטומי חמצן וצורן בקוורץ. עקב ההרכב הכימי הנקי של קוורץ, ונפיצותו הרבה בסלעי הקרום, מהווים איזוטופים אלו כלי עבודה ראשי לתארוך זמני חשיפה וקבורה של סדימנטים נחליים בכל רחבי העולם.

<u>מטרת העבודה הנוכחית היתה להבין ולכמת את היחסים שבין ההשתפלות הטקטונית של השוליים המערביים של בקע ים המלח בפליו-פלייסטוקן, לבין התגובה של אגני הניקוז בנגב המרכזי והדרומי בתקופה זו</u>. בפרט, תוארכו זמני הנטישה של 12 מפלסי זרימה של הפלאו-פארן ושל ״אפיק אדום״, השמורים בנגב המרכזי והדרומי בקוי פרשות המים ובתוך האגנים הנוכחיים (פרק 4). בנוסף, פרופילי עומק מפורטים של טרסות אלוביאליות מהפלייסטוקן האמצעי והמאוחר וההולוקן נדגמו בקניון נקרות ובגרבן כרכם לצורך השוואת גילים מתיארוך בשיטת האיזוטופים הקוסמוגנים ובשיטת הלומיניסנציה (OSL), ובמטרה לקבוע את קצבי הארוזיה האגניים בתקופת הרבדתן של הטרסות (פרק 5). לבסוף, נעשה נסיון לתארך את זמן ההרבדה של תצורת ערבה בגרבן כרכם (פרק 6).

<u>תארוך זמני הנטישה של מפלסי הזרימה של הפלאו-פארן (פרק 3)</u> נעשה על דוגמאות שהכילו מאות חלוקי ״ריצוף מדברי״ שנאספו מגג של כל מפלס נטוש. ה״ריצוף המדברי״ הינו השכבה העליונה ביותר של קרקע מדברית, ומורכב ברובו מחצצי צור בגודל אחיד של 2-4 ס״מ המכוסים פטינה שחורה, השרועים במוזאיקה צפופה מעל אופקי אבק המלוכדים בגבס. חצצי ה״ריצוף המדברי״ מייצגים את שכבת החלוקים העליונה ביותר שהייתה שרועה באפיק הנחל בזמן נטישתו. מכיוון ששכבת חלוקים עליונה זו אינה נקברת באקלים צחיח קיצון ובהיעדר זרימת מים (האבק המדברי חודר בין הרווחים שבין החלוקים ונוסף לקרקע שמתחתיהם), רווחת ההנחה כי חלוקי ״הריצוף המדברי״ נמצאים בפני השטח של טרסה הנחלית מיום היווצרותה, ונתונים לשטף הקבוע של הקרינה הקוסמית בפני השטח. בהנחה שהריכוז הקוסמוגני ההתחלתי של החלוקים שהתגלגלו בנחל הינו זניח לעומת הריכוז אותו רכשו מאז שהטרסה ננטשה, ושהגובה המוחלט של הטרסה בעבר היה זהה לגובהו כיום, אפשר לחשב ״גיל חשיפה פשוט״ שמשמעו – הזמן שחלוקי ה״ריצוף המדברי״ חשופים לקרינה הקוסמית בפני השטח של האתר הנדגם. את 12 גילי החשיפה שהתקבלו, יחד עם 2 גילים נוספים מעבודה קודמת, ניתן לסווג ל-2 קבוצות עיקריות:

א. 5 גילי חשיפה עתיקים, בעלי ממוצע של 1.8±0.2 מ״ש, נמדדו בלי יוצא דופן בקוי פרשות המים המרכזיות בנגב (פארן/נקרות, שיטה/חיון, חיון/ציחור, חיון/פארן), ומציינים את גיל ההתפרקות של אגן הפלאו-פארן למערכת הזרימה של היום. חוסר קיום תלות מובהקת בין גיל המשאר לבין מרחקו מהבקע, מצביע על קריסה פלוביאלית בו-זמנית במרחבי הנגב, ומודיפיקציה של מערכת הנחלים אל מתכונתה הנוכחית לאורך תקופה של 300 עד 400 אלף שנה.

ב. 9 גילי חשיפה צעירים יותר, הנעים בטווח בין 0.2 – 1.4 מ״ש, נמדדו בטרסות הנמצאות בתוך האגנים הנוכחיים, ומהווים עדות רציפה להתחתרות הנחלים במתווה הנוכחי מאז

תקציר

נחל פארן-נקרות היה אפיק זרימה עיקרי תת-מקביל לבקע, שהתפתח בפליוקן בעקבות פתיחת בקע ים המלח. קונגלומרטים ויחידות אגמיות המשויכות למערכת הניקוז פארן-נקרות ידועים בשם "תצורת ערבה". הנחל, שניקז שטחים גדולים שכללו את האגנים הנוכחיים של פארן, נקרות וחיון, חצה את הנגב הדרומי מאזור בקעת הירח בסיני דרך אגני כרכום ומישר בנגב המרכזי ומשם זרם דרך קניון נקרות אל הערבה הצפונית באזור עין יהב. אל אפיק מרכזי זה התחברו נחלים משניים ממזרח. הבולט מביניהם ("אפיק אדום") היה נחל שניקז את שולי הרי אדום דרך אזור "גב הערבה" והתחבר אל האפיק המרכזי של הפלאו-פארן באזור הר חלמיש. המשך שקיעתו של הבקע גרם להטייה טקטונית הדרגתית של הנגב בשיעור של כמעלה עד שתיים למזרח. ההטיה למזרח, אשר לוותה בפעילות טקטונית לאורך מערכת העתקים מקבילה לבקע, הביאה לשינויים בולטים במערכות הניקוז כבר בתחילת הפלייסטוקן. שיפועי הנחלים שזרמו כלפי מערב התמתנו ופחתו ; בזמן שהגרדיינט האזורי בנגב המרכזי והדרומי התקרב לאפס, הורבדה יחידה אגמית וקונגלומרטים אוטוכטונים (תצורת צחיחה) שטשטשו את גבולות אגן הפלאו-פארן ; שביית נחלים אל הבקע ההולך ומעמיק גרמה להתפרקות אגן הפלאו-פארן וליצירת לאגנים מקומיים קטנים יותר, ונוצר מתווה הזרימה הנוכחי. על גבולות האגנים הנוכחיים ובסמוך לקוי פרשות מים עיקריות, ניתן למצוא משטחים אלוביאליים נטושים משלב ההתפרקות של הפלאו-פארן, שבהיעדר זרימת מים התפתחה בהם קרקע רג מדברית בוגרת. גובהם של משארי "אפיק אדום" נמצאים כיום בגרדיינט הפוך לשיפועו של הנחל המקורי (דהיינו, הולכים ויורדים למזרח), ומהווים סמן בולט למידת ההשתפלות האזורית אל הבקע מאז הרבדתם. שלבי ההתפתחות של מערכות הניקוז הנוכחיות מיוצגים על ידי טרסות אלוביאליות הממוקמות בשולי האפיקים הפעילים. על אף שהיחידות האלוביאליות הפליו-פלייסטוקניות בנגב כבר מופו ותוארו בפירוט רב בעבודות קודמות, עד היום לא היתה אינפורמציה ישירה לגבי גילי הרבדתם ונטישתם בכלל, וגיל התפרקות אגן הפלאו-פארן בפרט. בעקבות כך, לא היו הערכות טובות לקצבי ההשתפלות הרביעוניים בערבה, כל זאת עקב היעדר שיטת תיארוך של משקעים יבשתיים בחלון הזמן המבוקש (פליו-פלייסטוקן).

ההתקדמות האנליטית המשמעותית שהושגה בעשרים השנים האחרונות ביכולת המדידה של ריכוזים נמוכים (10^5~ אטומים) בספקטרומטר-מסות אטומי, הפכה את התארוך בעזרת איזוטופים קוסמוגניים לשיטה נגישה ומוכרת בגאומורפולוגיה, המאפשרת לתארך את זמן החשיפה של סדימנט בפני השטח או את זמן קבורתו לעומק בחלון הזמן של עד עשרות מליוני שנים. השיטה מתבססת על קיומה של "קרינה קוסמית" שהינה שטף של חלקיקים אלמנטריים (נויטרונים, פרוטונים, מיואונים) בעלי אנרגיות גבוהות המתפשטים בחלל ופוגעים באטומים ובמולקולות הנמצאים ברום האטמוספירה של כדור-הארץ. כל התנגשות של חלקיק אלמנטרי עם אטום מלווה בפירוק האטום (spall), העפת "נתז" המורכב מחלקיקים אלמנטריים חדשים (קרינה קוסמית משנית), ויצירת איזוטופ חדש בעל מסה אטומית נמוכה מזו של האטום שנפגע. (האיזוטופ ה"קוסמוגני" המוכר ביותר הינו ^{14}C, הנוצר מפגיעת נויטרון קוסמי באטום של חנקן.) הקרינה הקוסמית המשנית (בעיקר נויטרונים) חודרת דרך האטמוספירה ומגיעה לפני השטח של כדור הארץ. קצב הייצור של איזוטופים קוסמוגנים בסלע נגזר ישירות מהעוצמה של שטף הקרינה המשנית. עוצמת הקרינה בפני השטח מושפעת מגובה האתר מעל פני הים ומקו הרוחב הגיאומגנטי, והקרינה דועכת באופן אקספוננציאלי עם העומק עד להיעלמותה ב-2-4 מ' בלבד (ככל שלסלע צפיפות גדולה יותר, עומק בלימת הקרינה הקוסמוגנית רדוד יותר). במקביל לקצבי הייצור השונים והקבועים (בקירוב טוב) של האיזוטופים הקוסמוגנים השונים בסלעים הקרובים לפני השטח, האיזוטופים הלא-יציבים שביניהם עוברים גם דעיכה רדיואקטיבית בקצב הנשלט על ידי ריכוזם וזמן מחצית חייהם.

משרד התשתיות הלאומיות
המכון הגיאולוגי

התפתחות הנוף והטקטוניקה בנגב המרכזי בתגובה להשתפלות בקע ים המלח

בני גורלניק

עבודת זו הוגשה כחיבור לקבלת תואר "מוסמך במדעי הטבע" במחלקה לגיאולוגיה,
המכון למדעי כדור הארץ, הפקולטה למדעי הטבע, האוניברסיטה העברית, ירושלים.

העבודה נעשתה בהדרכתם של:
ד"ר ארי מטמון, המחלקה לגיאולוגיה, המכון למדעי כדור הארץ, האוניברסיטה העברית, ירושלים
ד"ר יואב אבני, המכון הגיאולוגי הישראלי, ירושלים
ד"ר עזרא זילברמן, המכון הגיאולוגי הישראלי, ירושלים

דוח מס' GSI/11/2009 ירושלים, חשון תש"ע, אוקטובר 2009